

# Connectomic analysis of apical dendrite innervation in pyramidal neurons of mouse cerebral cortex

Dissertation

zur Erlangung des Doktorgrades

der Naturwissenschaften

vorgelegt beim Fachbereich Biowissenschaften

der Johann Wolfgang Goethe - Universität

in Frankfurt am Main

von

Ali Karimi

aus

Mashhad, Iran

Frankfurt am Main, 2020

(D 30)

Vom Fachbereich Biowissenschaften der

Johann Wolfgang Goethe - Universität als Dissertation angenommen.

Dekan: Prof. Dr. med. Sven Klimpel

Erstgutachter : Prof. Dr. Amparo Acker-Palmer

Zweitgutachter : Prof. Dr. Moritz Helmstaedter

Datum der Disputation :

*To Maryam and Mohammad-Hosseini.*

*Thank you for all the memories.*

# 1. Acknowledgements

This scientific endeavor would not have been possible without the help of my colleagues at the Connectomics Department. I think this has been the most intense learning period in my life. To be around such wonderful group of smart, humble individuals was extremely gratifying. The conversations we had shaped every aspect of my professional and personal life.

First, I would like to thank Moritz Helmstaedter for giving me this opportunity and his continuous support and guidance during the past 4 years. I wish to thank Florian Drawitsch, Jakob Straehle, Anjali Gour, Meike Schurr, Yunfeng Hua and Philip Laserstein for discussions regarding multiple aspects of the experimental procedure from sample preparation to dataset acquisition. Manuel Berning, Benedikt Staffler, Alessandro Motta, Martin Schmidt, Sahil Loomba and Emmanuel Klinger for their support regarding various aspects of our data analysis pipeline and help with implementation of the various analysis procedures and aberration adjustment software package.

In addition to the ACC dataset, Jan Odenthal provided a large fraction of the skeleton annotations and the initial version of the analysis routines. Our discussions were always a way for me to figure out new directions for the apical dendrite analysis project. Additionally, the LPtA and S1 datasets were provided by Florian Drawitsch and Kevin Boergens, respectively. The FluoEM code repository provided by Florian Drawitsch significantly eased the challenging process of identifying long-range projections in correlative light and electron microscopic datasets.

In addition, I would like to thank Dr. Kevin Briggman and Prof. Dr. Amparo Acker-Palmer who provided guidance and constructive feedback throughout my doctoral research as members of the thesis advisory board.

Jakob Straehle, Sahil Loomba, Kun Song, Vijayan Gangadharan and Marcel Beining provided information and overview images of their datasets acquired using the automated aberration adjustment software. Jakob Straehle helped implement the initial version of the software on the Verios microscope. Our conversations helped the design of multiple experimental and analysis procedures during my PhD.

We thank M. S. E. A. Aly, L. Bezenberger, A. B. Brandt, B. Heftrich, A. C. Rix, B. L. Stiehl, C. Arras, C. M. Schumm, D. E. Celik, D. J. Goffitzer, J. Buß, K. M. Trares, K. Weber, L. Buxmann, L. Decker, L. C. R. Kreppner, M. S. Kronawitter, N. M. Böffinger, N. Plath, S. M. Bohne, S. Reichel, T. Engelmann, T. Ernst, T. Winkelmeier, V. C. Kalbert, K. Kramer, L. Präve, M. Präve, N. Berghaus, O. J. Brandt, S. S. Wehrheim for neurite reconstructions, Heiko Wissler, Susanne Babl, Lisa Bezenberger, Alexander Brandt, Raphael Jakoby, Raphael Kneißl and Marc Kronawitter for annotator training and task management and Heiko Wissler for support with visualizations.

Comments on the initial version of the thesis at hand were provided by Martin Schmidt, Sahil Loomba, Kun Song, Jan Odenthal and Renee Hartig. Martin Schmidt translated the summary of the thesis to German.

Finally, I would also like to thank my family and friends for helping me during this intense phase and apologize for my lack of presence. I would like to specifically thank my wife, Renee, for her patience, grace and positivity when mine was gone.

## 2. Table of Contents

<b>1. Acknowledgements</b>	<b>IV</b>
<b>2. Table of Contents</b>	<b>VI</b>
<b>3. Index of Figures and Tables</b>	<b>X</b>
<b>4. Summary (English)</b>	<b>XII</b>
<b>5. Zusammenfassung / Summary (German)</b>	<b>XIV</b>
<b>6. Introduction</b>	<b>1</b>
6.1. Cerebral cortex in mammalian brains	1
6.2. Wiring in cerebral cortex: canonical cortical circuit model	2
6.3. Functional properties of pyramidal neurons and their apical dendrites	3
6.4. Role of dendritic spines in pyramidal neurons	6
6.5. Inhibitory innervation of apical dendrites	6
6.6. Balance between excitation and inhibition in pyramidal neurons	7
6.7. Methods to generate connectivity data in the cerebral cortex	8
6.8. Automated aberration adjustment for SBEM	14
6.9. Sample preparation for 3D electron microscopy	16
6.10. Analysis of 3D-EM volumes for connectivity	18
6.11. Impact of long-range input on pyramidal neurons (case study in S1)	19
6.12. FluoEM: an ideal method to map long-range input in 3D-EM	21
6.13. Long-range input to posterior parietal cortex (PPC)	23
6.14. Outlook and contributions	24
<b>7. Materials and Methods</b>	<b>25</b>
7.1. Volumetric electron microscopy imaging of cortex	25
7.1.1. Animal experiments	25
7.1.2. S1, LPtA sample preparation	25
7.1.3. Transcardial perfusion	25
7.1.4. Cortical region targeting and tissue extraction	26

7.1.5. Electron microscopy dataset names .....	26
7.1.6. En-bloc sample preparation for 3D electron microscopy .....	26
7.1.7. Serial block-face electron microscopy (SBEM).....	27
7.1.8. Image alignment .....	28
7.1.9. Estimating EM beam aberration parameters using image autocorrelation .....	30
7.1.10. The detection of large objects in EM micrographs.....	30
7.2. Cell-type specific innervation of apical dendrites .....	31
7.2.1. Skeleton reconstruction and synapse annotation .....	31
7.2.2. Apical dendrite (AD) definition and classification .....	31
7.2.3. Identification of layer 2 marginal (L2MN) and slender-tufted layer 5 (L5st) neurons .....	33
7.2.4. Complete synaptic input mapping of apical dendrites.....	34
7.2.5. Inhibitory input fraction mapping in upper cortex .....	35
7.2.6. Distance to soma and synapse composition at the main bifurcation.....	36
7.2.7. Inhibitory fraction along L2 apical dendrites .....	36
7.2.8. Identity estimation for shaft and spine synapses .....	36
7.2.9. Synapse size estimation .....	37
7.2.10. Spine apparatus at the main AD bifurcation .....	37
7.2.11. Apical dendrite diameter and synapse density per unit surface area .....	37
7.2.12. Conditional innervation probability of inhibitory axons .....	37
7.2.13. Dirichlet-multinomial model for postsynaptic targeting probability.....	38
7.2.14. Multiple innervation of an AD by inhibitory axons .....	38
7.2.15. Distribution of pre- and post-synaptic neurites along cortical depth.....	39
7.2.16. Visualization of neurites and their synapses.....	39
7.2.17. Statistics .....	40
7.2.18. Data and software availability.....	41
7.3. Correlative volumetric light and electron microscopy .....	42
7.3.1. Viral injection into M2 and V1 cortices.....	42
7.3.2. Sample preparation and confocal laser scanning light microscopy (LM) .....	43
7.3.3. Alignment of long-range axons between 3D-LM and EM.....	43
7.3.4. Extracting distribution of postsynaptic targets .....	43
<b>8. Results .....</b>	<b>45</b>
8.1. Synaptic composition in apical dendrites of pyramidal neurons .....	45
8.1.1. Synaptic composition at the main bifurcation of layer 2 (L2) and deep layer (L3/5) pyramidal neurons .....	45
8.1.2. More detailed definition of cell types in datasets containing layers 1-5.....	48

8.1.3. Layer 2 marginal neurons (L2MN) and slender-tufted layer 5 (L5st) neurons .....	52
8.1.4. Synaptic composition at the main bifurcation of L2-5 pyramidal neurons .....	54
8.1.5. Distal apical dendrites' synaptic composition in layer 1 for L2-5 pyramidal neurons .....	56
8.1.6. Distance to the soma as a determining factor for inhibitory fraction at the main bifurcation.....	58
8.1.7. Depth dependence of synapse composition for pyramidal neurons.....	60
8.1.8. Synapse size and spine properties around the main bifurcation.....	62
8.1.9. Postsynaptic dendritic targets of excitatory and inhibitory synapses and the effect on the estimation of synapse densities .....	64
8.1.10. Synapse density normalized to surface area of dendrite .....	65
8.2. Innervation profile of AD-targeting inhibitory axons in layer 2 of neocortex.....	68
8.2.1. Cell-type innervation specificity of AD-targeting axons in layer 2.....	68
8.2.2. Distribution of pre- and postsynaptic targets across cortex .....	70
8.2.3. Multiple innervation of apical dendrites by inhibitory axons .....	71
8.2.4. Comparing inhibitory axon innervation preference across mouse cortex.....	73
8.3. Correlative 3D-EM in the posterior parietal cortex .....	74
8.3.1. Automatic aberration adjustment of long-term SBEM experiments.....	74
8.3.2. Application of FluoEM to input from secondary motor (M2) and primary visual (V1) areas to posterior parietal cortex (PPC) .....	76
<b>9. Discussion.....</b>	<b>82</b>
9.1. Cell-type specific synaptic innervation in apical dendrites of pyramidal neurons.....	82
9.1.1. Cell-type specific synaptic composition on apical dendrites .....	82
9.1.2. Non-specific volume transmission and inhibition of L5 apical dendrites.....	84
9.1.3. Distance to soma as a determining factor of inhibitory strength at the main bifurcation of pyramidal neurons .....	85
9.1.4. Definition of L5 pyramidal neuron subtypes.....	86
9.1.5. Composition of synapses onto shaft and spine of apical dendrites.....	86
9.1.6. Synapse density normalized to the surface area of apical dendrites .....	87
9.1.7. Specific innervation of L2 and L3/5 ADs.....	88
9.1.8. Multi-innervation of apical dendrites by inhibitory axons.....	88
9.1.9. Quantitative consistency of axonal innervation across cortical regions.....	89
9.2. EM connectomic analysis of long-range input to posterior parietal cortex (PPC) ....	90
9.2.1. Importance of image quality control routines in long-term high throughput volumetric 3D-EM .....	90
9.2.2. Cell-type specific innervation of neurons in PPC by long-range input from M2 and V1 .....	91



<b>10. Tables.....</b>	<b>93</b>
<b>11. References.....</b>	<b>100</b>
<b>12. Curriculum vitae (CV).....</b>	<b>117</b>

### 3. Index of Figures and Tables

Figure 1. Coupling of input to the distal apical dendrite and basal input regions for layer 5 pyramidal neurons.....	5
Figure 2. Methods for 3D reconstruction of neuronal circuits using electron microscopes ....	11
Figure 3. Conceptual summary of FluoEM as a method for mapping long-range innervation using combined 3D light and electron microscopy .....	22
Figure 4. 3D electron microscopy datasets of size $\sim 10^6 \mu\text{m}^3$ used for analysis .....	46
Figure 5. Complete synaptic input mapping of the main bifurcation of apical dendrites in pyramidal neurons.....	47
Figure 6. Datasets used for detailed cell-type specific analysis .....	49
Figure 7. Reconstruction of apical dendrites of pyramidal neurons used in cell-type specific analysis .....	51
Figure 8. Classification of L5 neurons into slender-tufted and thick-tufted subtypes. ....	53
Figure 9. Cell-type specific inhibitory size at the main bifurcation of apical dendrites.....	55
Figure 10. Inhibitory fraction at the distal apical dendrite tuft of L2-5 pyramidal neurons .....	57
Figure 11. Distance of the dendritic segment to soma controls inhibitory fraction .....	59
Figure 12. Complete synaptic input map of segments of layer 2-5 pyramidal neurons.....	60
Figure 13. Synaptic densities across upper cortex for pyramidal neurons.....	61
Figure 14. Properties of synapses and spines around the main bifurcation .....	63
Figure 15. The dendritic target of excitatory and inhibitory synapses and its effect on the fraction of inhibitory synapses .....	65
Figure 16. Apical dendrite diameter and synapse density normalized to the surface area of dendrites .....	67
Figure 17. Cell-type specific innervation of apical dendrites by inhibitory axons in layer 2 of neocortex .....	69
Figure 18. Spatial distribution of main bifurcation of ADs and axons across the upper cortical layers .....	70
Figure 19. Multiple innervations of apical dendrites by inhibitory axons .....	72

Figure 20. Consistent innervation profile of inhibitory axons across the neocortex .....	73
Figure 21. Design of software for automatic adjustment of objective lens and stigmators in 3D electron microscopy .....	75
Figure 22. Example datasets acquired by colleagues using automatic aberration adjustment software.....	76
Figure 23. Application of FluoEM, correlated light and electron microscopy, to motor (M2) and visual (V1) input to posterior parietal cortex (PPC) .....	77
Figure 24. The depth profile of cell bodies in PPC innervated by axons from secondary motor (M2) and visual (V1) cortices .....	79
Figure 25. Cortical depth of soma for postsynaptic targets of individual axons from V1 and M2 cortical regions .....	81
Table 1. Experimental details .....	94
Table 2. Temperature and times of dehydration and embedding steps for 3D-EM samples .....	95
Table 3. Data analysis .....	96
Table 4. Fraction of spine-preferring (excitatory) input on spine and shaft of apical dendrites .....	97
Table 5. The somatic depth of pyramidal neurons relative to pial surface .....	98
Table 6. Datasets acquired using automated aberration adjustment.....	99

## 4. Summary (English)

The central goal of this study was to generate synapse-resolution maps of local and long-range innervation on apical dendrites (AD) in mouse cerebral cortex. We used three-dimensional electron microscopy (3D-EM) to first measure the cell-type specific balance in the excitatory and inhibitory input on ADs. Further, we found two inhibitory axon populations with preference for apical dendrites originating from layer 2 and 3/5. Additionally, we used a combination of large-scale volumetric light and electron microscopy to investigate the innervation preference of long-range cortical projections onto ADs. To generate such large-scale 3D-EM datasets, we also developed a software package to automate aberration adjustment.

The balance of excitation and inhibition defines the computational properties of neurons. We, therefore, generated 6 datasets and annotated 26,548 excitatory and inhibitory synapses to map the relative inhibitory strength on the AD of pyramidal neurons in layers 1 and 2 (L1 and 2) of the cortex. We found consistent and cell-type specific patterns of inhibitory strength along the apical dendrite of L2-5 pyramidal neurons in primary somatosensory (S1), secondary visual (V2), posterior parietal (PPC) and anterior cingulate (ACC) cortices. L2 and L5 pyramidal neurons had inhibitory hot-zones at their main bifurcation and distal apical dendrite tuft, respectively. In contrast, L3 neurons had a baseline (~10%) level of inhibition along their apical dendrite. As controls, we quantified the effect of synapse strength (size), dendrite diameter, AD classification and synapse identification methods on the cell-type specific synapse densities. To classify L5 pyramidal subtypes, we performed hierarchical clustering using morphological properties that were described to differentiate slender- and thick-tufted L5 neurons.

We also investigated the distance to soma as a predictor of fractional inhibition around the main bifurcation of apical dendrites. Interestingly, we found a strong exponential relationship that was absent in density of either synapse type. This suggests a distance dependent control mechanism designed specifically for the balance (in synapse numbers) of excitation and inhibition.

Next, we focused on the inhibitory innervation preference for apical dendrite of pyramidal neuron. We, therefore, annotated 5,448 output synapses of AD-targeting inhibitory axons and found two populations specific for either L2 or L3/5 apical dendrites. Together with previous findings on preferential innervation of sub-cellular structures by inhibitory axons, this suggests two distinct inhibitory circuits for control of AD activity in L2 vs. deep-layer pyramidal neurons. This innervation preference was surprisingly consistent across S1, V2, PPC and ACC cortices.

3D-EM data acquisition is a laborious process that is made easier and more popular everyday by technical progress in the laboratory and industrial settings. To make data acquisition robust using our custom-built 3D-EM microscopes, an automatic aberration software was implemented to adjust the objective lens and the stigmators of the electron microscope. This method was used in multiple month-long experiments across 2 microscopes and 10 datasets. The aberration adjustment used the reduction in image details (high-frequency elements) to estimate the level of deviation from optimal focus and stigmator parameters. However, large objects in EM micrographs such as blood vessel and nuclei cross-sections generated anomalous results. We, therefore, added image processing routines based on edge detection combined with morphological operations to exclude such large objects.

Finally, we performed a correlative three-dimensional (3D) light (LM) and electron (EM) microscopy experiment to map the long-range primary visual (V1) and secondary motor (M2) cortical input to ADs in layer 1 of PPC using the “FluoEM” approach. This method allows for identification of the long-range source of projection axons in EM volumes without the need for EM-dense label conversion or heat-induced markings. The long-range source of an axon in EM is identified based on the fluorescent protein that is expressed in its LM counterpart. In comparison to M2 input, Long-range axons from V1 had a higher tendency to target L3 pyramidal neurons in PPC according to our preliminary analysis. In combination with the difference observed in the synapse composition of L2 and L3 apical dendrites, this suggests the need for separate functional and structural analysis of L2 and 3 pyramidal neurons.

## 5. Zusammenfassung / Summary (German) <sup>1</sup>

Das zentrale Ziel dieser Studie war die Erstellung synapsenaufgelöster Verschaltungskarten der lokalen und langreichweitigen Innervation apikaler Dendriten (AD) von Pyramidenzellen in der Großhirnrinde von Mäusen. Zu diesem Zweck nutzten wir die dreidimensionale Elektronenmikroskopie (3D-EM) zur Aufnahme 6 kortikaler Volumina und ermittelten das zelltypspezifische Gleichgewicht in den exzitatorischen und inhibitorischen Inputs. Darüber hinaus untersuchten wir die lokale inhibitorische Präferenz der Innervation von ADs in Pyramidenzellen der Schichten 2-5 (L2-5). Zudem nutzten wir eine Kombination von großskaliger volumetrischer Licht- und Elektronenmikroskopie zur Untersuchung der Innervationspräferenz von langreichweitigen, kortikalen Projektionen auf kortikale Neuronen. Um diese großen 3D-EM-Datensätze zu generieren, haben wir ein Softwarepaket zur Automatisierung der Aberrationsanpassung entwickelt.

Das Gleichgewicht von Exzitation und Inhibition definiert die rechnerischen Eigenschaften von Neuronen. Wir haben daher sechs 3D-EM Datensätze aus 5 verschiedenen kortikalen Regionen aufgenommen und 26,548 exzitatorische und inhibitorische Synapsen annotiert, um die relative inhibitorische Innervation der apikalen Dendriten in den Schichten 1 und 2 (L1 und 2) des Kortex abzubilden. In Primären Somatosensorischen (S1), Sekundären Visuellen (V2), Posterioren Parietalen (PPC) und Anterioren Zingulären (ACC) Kortizes fanden wir konsistente und zelltypspezifische Muster der relativen inhibitorischen Stärke entlang des apikalen Dendriten von L2-5-Pyramidenzellen.

L2 Pyramidenzellen wiesen an ihrer AD Hauptbifurkation eine Inhibitionszone auf. Der Anteil an Inhibition war im Vergleich zum Grundniveau der Inhibition (10%) in L3/5 Pyramidenzellen um das Dreifache erhöht. Erhöhte inhibitorische und verringerte exzitatorische Synapsendichten tragen beide zu einer Inhibitionszone an der L2 AD Hauptbifurkation bei. Im Gegensatz dazu zeigten L5 *thick-tufted* (L5tt) Pyramidenzellen eine erhöhte relative Inhibition an ihrem distalen AD *tuft*. Die

---

<sup>1</sup> Translated to German by Martin Schmidt

geringe exzitatorische Synapsendichte im Vergleich zur Hauptbifurkation stellte sich als der wesentliche Faktor dieser distalen Inhibitionszone von L5tt-Neuronen heraus. Die distale Inhibitionszone könnte möglicherweise den Erregungsgrad um die Hauptbifurkation gezielt steuern. Interessanterweise zeigten L3 Neuronen eine Grundinhibition (~10%) über ihren gesamten apikalen Dendriten in L1-3. Diese Ergebnisse weisen auf das Gleichgewicht von Exzitation und Inhibition (der Synapsenanzahl) als zelltypspezifisches Merkmal von Pyramidenzellen in L1-3 des Kortex hin, was ihnen einzigartige rechnerische und integrierende Eigenschaften verleiht.

Als Kontrollen verglichen wir die Synapsengrößen und Häufigkeiten von Zweifachinnervationen der Dornfortsätze durch inhibitorische Axone zwischen L2 und L3/5 AD Hauptbifurkationen. In früheren Veröffentlichungen wurde die Korrelation zwischen Synapsengröße und Synapsenstärke bereits gezeigt. Die inhibitorischen Synapsen waren an der Hauptbifurkation der L2 ADs größer (und entsprechend wahrscheinlich stärker). Zusätzlich wurde ein größerer Anteil von L2 AD Dornfortsätzen im Vergleich zu den Dornfortsätzen von L3/5-ADs mit einer inhibitorischen Synapse co-innerviert. Insgesamt deuten die Synapsenanzahl, -größe und -doppelinervation der Dornfortsätze auf ein erhöhtes Maß an Inhibition an der Hauptbifurkation von L2 ADs hin.

Die Eingangsimpedanz eines Dendriten ist proportional zur Amplitude der elektrischen Spannung der postsynaptischen Zelle. Der AD-Durchmesser (und die Oberfläche) steuern die Eingangsimpedanz. Wir haben deshalb den Durchmesser und die Oberfläche von ADs gemessen und fanden einen circa zweifach reduzierten Durchmesser der distalen Dendriten im Vergleich zu Dendritendurchmessern an der Hauptbifurkation. Darüber hinaus hatten *slender-tufted* L5-Neuronen (L5st) die dünnsten ADs im Vergleich zu anderen Pyramidenzellen. Die zelltypspezifischen Unterschiede in der Synapsendichte, normalisiert mit der Apikaldendritlänge, wurden ebenfalls beobachtet wenn mit der Oberfläche statt der Länge normalisiert wurde.

Wir klassifizierten zunächst Synapsen auf dem dendritischen Schaft und die dendritischen Dornfortsätze von ADs als inhibitorisch bzw. exzitatorisch. Um den Fehler dieser Klassifizierung zu quantifizieren, rekonstruierten wir in L1-2 eine

Teilmenge von Axonen die Schaft oder Dornenfortsatz von ADs innervieren. Unser Ziel war es festzustellen, ob das präsynaptische Axon inhibitorisch (schaftpräferierend) oder exzitatorisch (dornenfortsatzpräferierend) war. Wir haben daher die Präferenz für Dornenfortsätze für jedes rekonstruierte Axon innerhalb des EM-Volumens quantifiziert. Interessanterweise war die Innervationspräferenz fast binär, d.h. Axone bevorzugten entweder Schaft oder Dornfortsätzen von ADs. Entsprechend lag die durchschnittliche Klassifizierungsfehlerrate für alle Neuronentypen mit Ausnahme von L5st-Neuronen unter 25%.

Pyramidenzellen werden traditionell anhand der kortikalen Schicht klassifiziert, in der sich ihr Soma befindet. Wir haben diesen Ansatz verwendet, um L2-, L3- und L5- Neuronen zu unterscheiden. Es wurde anderswo jedoch auch über morphologische und funktionelle Subtypen von Neuronen berichtet, die sich in derselben Schicht befinden. Deshalb suchten wir speziell nach L2 marginalen Neuronen (L2MN) mit einem schrägen Apikaldendriten (*oblique AD*) relativ zur *pia mater*. Wir führten zudem eine Analyse der Synapsendichte um die AD Hauptbifurkation durch. Unsere vorläufige Analyse (n = 2) ergab keinen signifikanten Unterschied zwischen den L2 und L2MN Pyramidenzellen.

Als nächstes untersuchten wir die Unterschied in der Synapsendichte zwischen L5tt und L5st Pyramidenzellen. Zunächst verwendeten wir die zuvor veröffentlichte Anzahl von schrägen Apikaldendriten, die kortikale Tiefe der Hauptbifurkation, Soma- und AD Schaftdurchmesser, um L5 Subtypen zu klassifizieren. L5st-Neuronen hatten einen kleineren Soma- und AD-Schaftdurchmesser. Darüber hinaus war der Ort der AD Hauptbifurkation in L1-3 und es gab eine geringere Anzahl von schrägen (*oblique*) Dendriten im Vergleich zu L5tt-Neuronen. Die morphologischen Merkmale von L5 Pyramidenzellen lassen jedoch auf ein Spektrum kontinuierlicher Subtypen mit unterschiedlichem Grad an „*thick-tuftedness*“ schließen. Interessanterweise hatte die Dichte der exzitatorischen Synapsen eine positive lineare Beziehung zur „*thick-tuftedness*“ von L5 Neuronen. Dies führt zu einem verringerten inhibitorischen Anteil an L5tt Neuronen im Vergleich zu L5st Neuronen.



Wir untersuchten auch den Abstand zum Soma als Prädiktor für die anteilige Inhibition der Hauptbifurkation apikaler Dendriten. Interessanterweise fanden wir eine starke exponentielle Beziehung, die in keiner Einzelsynapsendichte (exzitatorisch bzw. inhibitorisch) vorhanden war. Dies legt einen abstandsabhängigen Kontrollmechanismus nahe, der für das Gleichgewicht (der Synapsenanzahl) von Exzitation und Inhibition spezifisch ist.

Als nächstes konzentrierten wir uns auf die Präferenz der inhibitorischen axonalen Innervation für den apikalen Dendrit von Pyramidenzellen. Wir annotierten 5448 Ausgabesynapsen von AD-innervierenden inhibitorischen Axonen und quantifizierten ihre Präferenz nach AD-Typen. Wir fanden zwei Populationen, die entweder für L2 oder für L3/5 Apikaldendriten spezifisch sind. Zusammen mit früheren Befunden zu präferentieller Innervation subzellulärer Strukturen durch inhibitorische Axone, legt dies zwei unterschiedliche inhibitorische Schaltkreise für die Kontrolle der AD-Aktivität in L2 vs. L3/5-Pyramidenzellen nahe. Die Innervationspräferenz war überraschend konsistent über S1-, V2-, PPC- und ACC-Kortizes.

Um zu untersuchen, ob eine geometrische Trennung zu einer solchen Innervationsspezifität führen kann, untersuchten wir die zelltypspezifische kortikale Tiefenverteilung der AD Hauptbifurkationen und der AD innervierenden inhibitorischen Axone. Wir fanden, dass ihre Tiefenverteilung ähnlich ist, was darauf hindeutet, dass die geometrische Trennung die spezifische Innervation von L2- und L3/5- ADs nicht erklären kann.

Es wurde berichtet, dass inhibitorische Axone Apikaldendriten geclustert und multisynaptisch innervieren. Daher haben wir solche Mehrfachinnervationen von Apikaldendriten durch einzelne inhibitorische Axone innerhalb unserer EM-Volumina von S1, V2, PPC und ACC annotiert. Wir stellten fest, dass ~80% der AD-Innervation durch inhibitorische Axone innerhalb der EM-Volumina ( $\sim 10^6 \mu\text{m}^3$ ) monosynaptisch sind. Daher wurde die Innervationsspezifität von AD-Typen nur geringfügig beeinflusst, wenn die mehrfache Innervation desselben postsynaptischen Ziels ignoriert wurde.

Die 3D-EM-Datenerfassung ist ein arbeitsaufwändiger Prozess, der durch den technischen Fortschritt im Labor und in der Industrie einfacher und populärer wird. Um

die Datenerfassung unserer spezialangefertigten 3D-EM Mikroskope robuster zu machen, wurde eine Software zur automatischen Detektion und Korrektur von Abbildungsfehlern implementiert, die die Parameter der Objektivlinse und der Stigmatoren des Elektronenmikroskops anpasst. Die Software erwies sich in mehrmonatigen Experimenten mit 2 Mikroskopen und 10 Datensätzen von 5 Experimentatoren als robust.

Die Aberrationsanpassung verwendete die Verringerung der Bilddetails (Hochfrequenzelemente), um den Grad der Abweichung von den optimalen Fokus- und Stigmatorparametern abzuschätzen. Große Objekte in EM-Aufnahmen wie Blutgefäß- und Zellkernquerschnitte führten jedoch zu anomalen Ergebnissen. Wir haben deshalb Bildverarbeitungsroutinen hinzugefügt, die auf Kantenerkennung in Kombination mit morphologischen Operationen basieren, um somit große Objekte auszuschließen.

In Veröffentlichungen wurde gezeigt, dass die auf die Schicht 1 des Kortex einwirkende langreichweitigen Innervationen die Aktivität von Pyramidenzellen *in vitro* und *in vivo* steuert. Daher wurden korrelative dreidimensionales (3D) Licht- (LM) und Elektron- (EM) Mikroskopien durchgeführt, um die langreichweitigen Verbindungen des Primären Visuellen (V1) und des Sekundären Motorkortex (M2) zu Schicht 1 des posterior parietalen Kortex (PPC) zu vermessen. Der „FluoEM“ Ansatz ermöglicht die Identifizierung der Quelle von langreichweitigen Verbindungen von Projektionsaxonen in EM, ohne dass eine EM-dichte Markierungsumwandlung oder wärmeinduzierte Markierungen erforderlich wären. Die Identifizierung der Quelle eines Axons basiert auf dem fluoreszierenden Protein, das in seinem LM-Gegenstück exprimiert wird. Das fluoreszierende Protein wird durch Virusinjektion in die Quellregionen abgegeben.

PPC ist ein Assoziationskortex mit reziproken Verbindungen zu sensorischen und multimodalen kortikalen Regionen. Es wird angenommen, dass er an verschiedenen Aspekten der sensomotorischen Transformationen im Kortex beteiligt ist. Daher wollten wir die Muster der langreichweitigen Innervation von Neuronen im PPC durch den Sekundären Motorcortex (M2) und den Primären Visuellen Cortex (V1) verstehen. Unsere vorläufige Analyse der postsynaptischen Ziele von 24

langreichweitigen Axonen legt nahe, dass der V1 Input eine höhere Tendenz aufweist, L3 Pyramidenzellen im PPC zu innervieren als M2 Projektionsaxone. In Kombination mit den beobachteten Abweichungen in der lokalen inhibitorischen Innervation von L2 und L3 Apikaldendriten resultiert die Notwendigkeit der getrennten Betrachtung von L2 und L3 Pyramidenzellen, die traditionell als ein einziger Zelltyp klassifiziert wurden.

Abschließend ergibt unsere Analyse der synaptischen Innervation in apikalen Dendriten von Pyramidenzellen der kortikalen Schichten 1-3 ein zelltypspezifisches Gleichgewicht in Exzitation und Inhibition. Inhibitorische Axone zeigen auch bevorzugte Innervation von L2 und L3/5 Apikaldendriten. Zusätzlich ergab auch die Analyse langreichweitiger Innervation der kortikalen Neuronen zelltypspezifische Präferenzen. Zusammengenommen legen diese Ergebnisse nicht-zufällige, spezifische Verschaltung von apikalen *tuft* Dendriten nahe. Dies erlaubt rechnerisch einzigartige Eigenschaften von L2, L3 und L5 Pyramidenzellen.

## **6. Introduction**

### **6.1. Cerebral cortex in mammalian brains**

Santiago Ramón y Cajal first described neurons as the discrete cellular components of the brain by using the Golgi staining method to visualize their structure (Cajal 1899). Neurons receive and convey electrical signals through dendritic and axonal protrusions which are connected through electrical and chemical synapses (Colonnier 1968). The human brain consists of a network of ~86 billion such interconnected neurons. About ~16 billion of these neurons are located in the cerebral cortex which covers the surface of the brain (Herculano-Houzel 2009). Neocortex with its six layers of cell bodies has been implicated in a wide variety of functions from sensory processing (Hubel and Wiesel 1959) to motor control (Cheney 1985, Brecht, Schneider et al. 2004) and cognition (Glickfeld, Histed et al. 2013, Guo, Li et al. 2014, Kato, Gillet et al. 2015).

There has been considerable progress in understanding several aspects of single cortical neuron properties since the anatomical investigation of Ramón y Cajal (Cajal 1899, Cajal, DeFelipe et al. 1988). The functional properties of single neurons and their ion channels have been described using patch-clamp recording techniques (Neher and Sakmann 1976, Hamill, Marty et al. 1981) and two-photon laser scanning microscopy (Denk, Strickler et al. 1990). To image activity of neurons, calcium sensors have been used (Svoboda, Denk et al. 1997). In addition, intervention in neuronal activity using light-sensitive ion channels (Boyden, Zhang et al. 2005) and neurotransmitter precursors (Denk 2006) were used to investigate the causal relationship between neuronal activity and various phenotypes. Molecular and cellular tools have also allowed us to investigate the basic properties of neurons, such as, synaptic transmission (Südhof 2013) and protein expression (Holt and Schuman 2013).

An average neuron receives about 10,000 synaptic inputs, and outputs a similar number of synapses to its neighbors (Megías, Emri et al. 2001). It is therefore postulated that a missing link in achieving a mechanistic understanding of the brain is the lack of knowledge about the structure of these networks (Denk, Briggman et al.

2012). However, methods to investigate the activity of biological neuronal networks, such as electroencephalography (EEG, (Berger 1929)) and functional magnetic resonance-imaging (f-MRI, (Ogawa, Lee et al. 1990)), suffer from poor resolution. A cubic millimeter (approximate size of an f-MRI voxel) contains about a hundred thousand neurons and a billion synapses. Therefore, brain connectivity at the single-cell resolution remained poorly understood until recently (Logothetis 2008, Helmstaedter 2013). The goal of electron microscopy (EM)-based connectomics is to fill this gap.

## **6.2. Wiring in cerebral cortex: canonical cortical circuit model**

The general flow of information in the cortex gives rise to the simplified “canonical” wiring model of cortical layers within each “cortical column” (Douglas and Martin 2004). The two most studied cortical regions for this model are the primary visual (Hubel and Wiesel 1959) and somatosensory cortices (Mountcastle 1957, Woolsey and Van der Loos 1970). The canonical wiring model describes information flow in a simple feedforward manner, where sensory information is delivered to the mid-section of cortex (centered on layer 4 (L4)) from the sensory thalamic input areas (Wimmer, Bruno et al. 2010). This input is then relayed to the cortical output neurons in layers 5 and 6 via L2/3 pyramidal neurons. The barrel-shaped thalamic input and cell body arrangement in L4 of mouse somatosensory cortex is the most well-defined demonstration of the cortical column concept. Additional support for this model was generated by the reconstruction of L2/3 axons that converge on L5/6 neurons (Narayanan, Egger et al. 2015).

Significant divergences from the canonical circuit model were observed *in vivo*. For example, it was shown that sensory thalamic input directly activates cortical output neurons in L5/6 (Constantinople and Bruno 2013). This is because pyramidal neurons extend their dendritic trees beyond the cortical layer that their soma resides (Larkum, Petro et al. 2018).

### **6.3. Functional properties of pyramidal neurons and their apical dendrites**

Pyramidal neurons make up the majority of neurons (70-85%) in the mammalian cerebral cortex and are also found in subcortical structures, such as, hippocampus and amygdala (Cajal 1899, Spruston 2008). They are known to be glutamatergic excitatory neurons (Conti, Rustioni et al. 1987) with spiny dendrites (Cajal 1899, Larkman 1991) that receive most of the excitatory input. Their subtypes have been historically defined by the layer where their cell body resides. However, it is important to note that the extent of input and output regions of these cells is much larger and is not restricted to their cell body layer (Narayanan, Egger et al. 2015, Larkum, Petro et al. 2018). In addition, recent single-cell transcriptomic and functional studies have found distinct subtypes within the same cortical layer (Economo, Viswanathan et al. 2018, Tasic, Yao et al. 2018).

Active changes in the membrane conductance of neurons were first described in giant squid axons (Hodgkin and Huxley 1952). Pyramidal neurons contain ligand- and voltage-gated ion-channels both in their dendrites and somata (Stuart and Sakmann 1994, Migliore and Shepherd 2002). These ion channels are involved in the active regeneration of membrane voltage transients. Investigation of ion channels was only made possible by the patch-clamp technique (Neher and Sakmann 1976).

One of the most significant morphological features of pyramidal cells is their apical dendrite (AD). This dendrite emanates from the apex of the pyramidal soma and is directed towards the surface of the cortex. It bifurcates at the level of layer 2 generating the apical tuft dendrite within layer 1 of the upper cortex for most pyramidal neurons (Larkman and Mason 1990, Ito, Kato et al. 1998). The role of the apical tuft dendrite has been a mystery since the long apical dendrite trunk (up to 1 mm in rats) acts as a low-pass filter attenuating the distal synaptic input. It was therefore postulated that this signal needs to be amplified at the main bifurcation of apical dendrites (W. A. Spencer 1959). Layer 5 pyramidal neurons are exceptional as their basal input region receives the primary sensory input in layer 4 (Wimmer, Bruno et al. 2010) and the AD tuft region gets the higher order (associative) cortical and thalamic feedback in layer 1 (Coogan and Burkhalter 1990, Cauller, Clancy et al. 1998). Hence, L5 neurons are

hypothesized to be the cellular substrate for combining the cortical input streams and a possible solution to the problem of “binding” distributed feature representation of a percept (object) in the brain (Larkum 2013). Additionally, feature-binding could allow the cortical neuronal networks to discern percepts from each other (Crick and Koch , Treisman 1996).

The existence of such active amplification of distal electrical input to apical dendrites was confirmed using optical fluorescent calcium imaging (Yuste, Gutnick et al. 1994) and whole-cell dendritic patch-clamp recordings (Stuart, Dodt et al. 1993, Stuart and Sakmann 1994). These studies identified a region around the main bifurcation of ADs with increased calcium response to electrical input in layer 5 pyramidal neurons (Helmchen, Svoboda et al. 1999, Larkum and Zhu 2002). Therefore, these neurons contain a secondary spike initiation zone that amplifies the input to the AD tuft.

Apical dendrites of L2/3 (Svoboda, Denk et al. 1997, Svoboda, Helmchen et al. 1999, Waters, Larkum et al. 2003) and L6 (Ledergerber and Larkum 2010) pyramidal neurons also display non-linear calcium spike events in response to concurrent input to their basal and AD tuft input domains. L5 neurons, however, are unique in the strength of their response to simultaneous synaptic input to their basal and AD tuft dendrites (Ledergerber and Larkum 2012).

Two seminal *in vitro* studies demonstrated that L5 pyramidal neurons act as biological coincidence detectors (Figure 1, (Larkum, Zhu et al. 1999, Larkum, Zhu et al. 2001)). Interestingly, Active back-propagation of somatic action potentials (APs) reduced the threshold for generation of calcium spikes around the main AD bifurcation. Furthermore, coupling a somatic action potential with sub-threshold input to the main AD bifurcation generates a burst of action potentials at the soma. The coupling strength between somatic and dendritic spike initiation zones was shown to depend on dendritic morphology (Schaefer 2003).

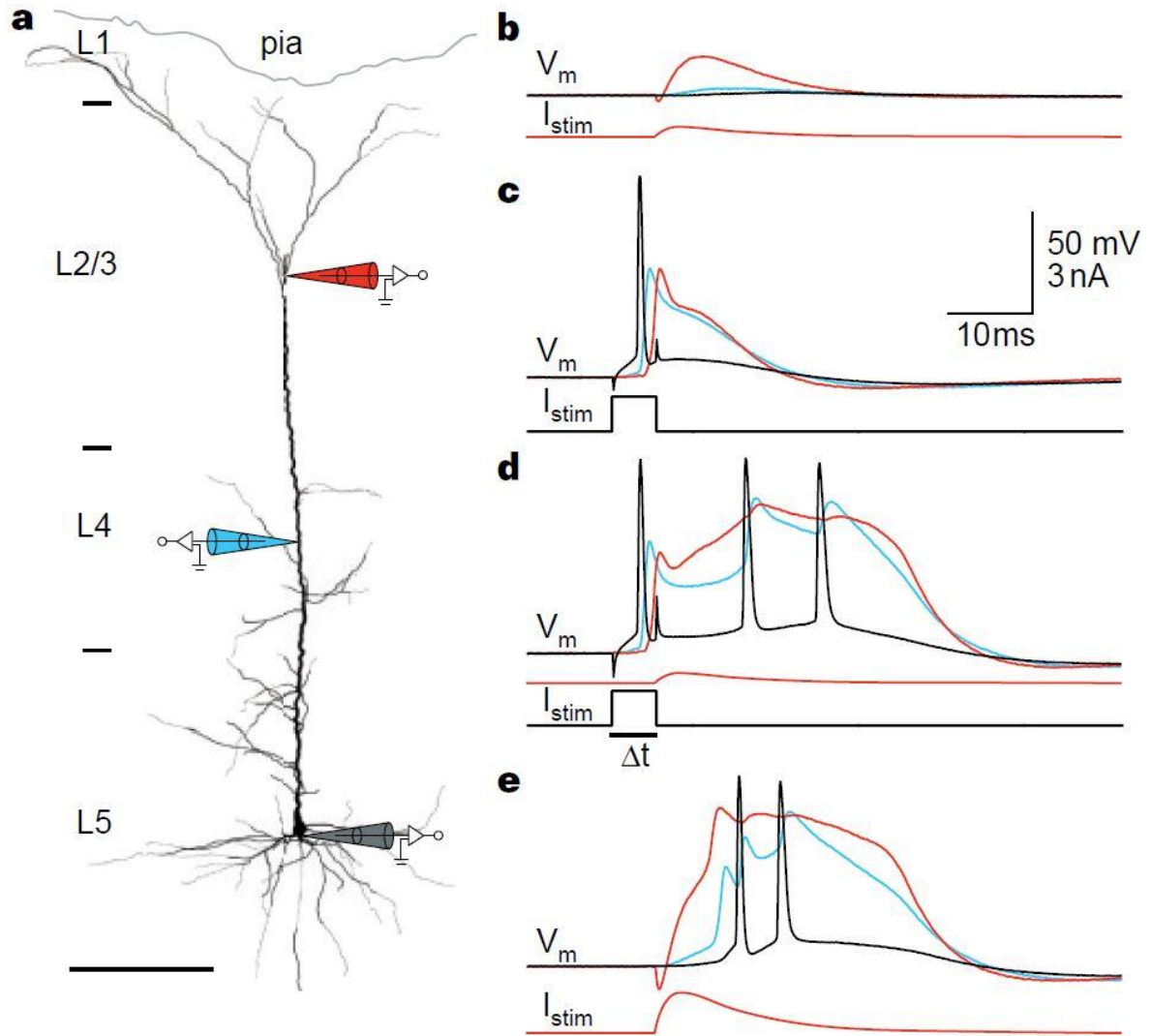


**Figure 1. Coupling of input to the distal apical dendrite and basal input regions for layer 5 pyramidal neurons**

**(a)** A biocytin-filled L5 pyramidal neuron, with the recording pipette positions shown. Cortical layers indicated on the left. Scale bar, 200  $\mu\text{m}$ . **(b)** Current injection with peak amplitude of 0.3 nA at the distal pipette (red trace, bottom) produced only a small signal at the soma. It did not reach threshold for either a  $\text{Ca}^{2+}$ -AP or a  $\text{Na}^{+}$ -AP.  $I_{stim}$  refers to traces representing injected current and  $V_m$  the recorded potential. Note that positive current creates intracellular depolarization. The color matches the corresponding electrode in the diagram. **(c)** Current injection above the  $\text{Na}^{+}$  spike at the soma (black trace) evoked a single AP. **(d)** The combination of the injections used in (b) and (c) separated by an interval of 5 ms evoked a burst of APs following the onset of the  $\text{Ca}^{2+}$ -AP



in the distal dendrite. Scale bars in (c) also apply to (b, d). **(e)** A similar dendritic  $\text{Ca}^{2+}$ -AP to (d) could be evoked by a far larger current injection alone at the distal dendritic electrode (1.2 nA). Reprinted with permission from Springer nature: Nature (Larkum, Zhu et al. 1999), copyright 1999.

#### **6.4. Role of dendritic spines in pyramidal neurons**

Most excitatory synapses are formed onto small dendritic spine protrusions in pyramidal neurons (Gray 1957, Chen, Villa et al. 2012). They form separate electrical compartments from the rest of the dendritic shaft and create localized calcium responses (Yuste and Denk 1995). The spine and shaft of a dendrite are coupled by a time constant of 20-100 ms (exponential diffusion) and a resistance of 4-50 MOhms, as measured by photo-conversion of fluorescent markers (Svoboda, Tank et al. 1996). In addition, back-propagating somatic action potentials invade spines, allowing them to detect the coincidence of post- and pre-synaptic activity during plasticity events (Markram, Lübke et al. 1997). The spine apparatus is a specialized form of endoplasmic reticulum found in spines; it was suggested to have a role in the release of calcium within the spine and the local synthesis of proteins (Špaček 1985, Segal, Vlachos et al. 2010).

#### **6.5. Inhibitory innervation of apical dendrites**

Inhibitory neurons are involved in a wide variety of cortical circuits and control various aspects of neuronal activity, even though they account for only ~12% of neurons ((Braitenberg and Schüz 1998), for a review see (Feldmeyer, Qi et al. 2018)). They also demonstrate a wide variety of morphological and electrophysiological properties (Markram, Toledo-Rodriguez et al. 2004). Their output is mostly localized around their cell body of origin (interneurons), even though evidence for long-range (projection) inhibitory neurons were recently reported (Yamawaki, Li et al. 2019).

Inhibitory neurons are known to target specific subcellular regions of pyramidal neurons. The chandelier cells, for example, almost exclusively target the initial axon segment of L2/3 pyramidal neurons (Somogyi 1977). Basket and Martinotti interneurons are known to target peri-somatic and apical tuft sub-regions, respectively (Kubota, Karube et al. 2016). However, their innervation specificity is not as extreme

as compared to chandelier cells. A recent dense connectomic reconstruction of  $5 \times 10^5 \mu\text{m}^3$  of layer 4 in mouse somatosensory cortex demonstrated quantitatively that at least 58% of all inhibitory axons were specific in their innervation of subcellular targets (Motta, Berning et al. 2019).

Interneurons release gamma-Aminobutyric acid (GABA) as their main neurotransmitter to inhibit the activity of their postsynaptic targets. GABA activates the ionotropic GABA<sub>A</sub> receptors in synapses with fast kinetics and specificity (synaptic transmission). In addition, GABA released to the extracellular space can activate the more sensitive metabotropic GABA<sub>B</sub> receptors with slower kinetics in a non-specific manner (volume transmission). Interneuron subtypes engage in either or both inhibitory transmission types (Tamás, Lőrincz et al. 2003). Neurogliaform neurons that are specialized in volumetric release of GABA inhibit ~85% of neurons within their dense axonal arbor (Oláh, Füle et al. 2009). EM connectomics allows the reconstruction of complete synaptic inhibitory wiring diagrams. However, no straightforward method to predict volume transmission has been described using only EM image volumes.

Since input to apical dendrites effects the output of neurons, it is not surprising that inhibitory input modulates non-linear calcium spikes observed both *in vitro* (Larkum, Zhu et al. 1999) and *in vivo* (Takahashi, Oertner et al. 2016, Abs, Poorthuis et al. 2018). Specific inhibitory circuits within cortex were described to modulate AD activity through synaptic inhibition in L1-3 (Jiang, Wang et al. 2013) and L5 (Silberberg and Markram 2007). In addition, the direct interaction between the GABA<sub>B</sub> receptors and voltage-gated calcium channels has been implied in long-lasting blockage (~400 ms) of dendritic calcium spikes through volume transmission (Pérez-Garci, Gassmann et al. 2006, Pérez-Garci, Larkum et al. 2013). To understand the innervation patterns of AD-targeting inhibitory neurons, we reconstructed their axons in four cortical regions.

## **6.6. Balance between excitation and inhibition in pyramidal neurons**

The spatial distribution of excitatory and inhibitory synapses has been shown to affect the activity and computational properties of neurons (Rall 1959, Rall and Rinzel 1973). Interaction of inhibitory and excitatory input can implement logical operations,

such as AND, NOT, as demonstrated in simulated neurons (Koch, Poggio et al. 1983, Bush and Sejnowski 1994). A biological implementation of this logical operation was found in the direction selectivity circuit of ganglion neurons in the mammalian retina. The inhibitory input from the starburst amacrine to ganglion neurons was effective in a directional manner, which results in their direction-selectivity (Fried, Münch et al. 2002). In addition, 3D-EM reconstruction of the same circuit demonstrated the existence of such direction-selective inhibitory innervation patterns (Briggman, Helmstaedter et al. 2011).

In cultured rat hippocampal cells, neurons controlled their inhibitory input ratio locally within each dendrite by using a feedback regulatory mechanism (Liu 2004). The implementation of circuit remodelling during experience-related plasticity was also investigated in both inhibitory and excitatory synapses (Harvey and Svoboda 2007, Chen, Villa et al. 2012). Interestingly, individual synapse strength is modulated by the activity of neighbouring synapses in a clustered manner.

The distribution of synapses has been used to suggest and provide evidence for a two-stage model of synaptic integration in pyramidal neurons. This model suggests that synaptic input is first summed linearly within each branch to generate a local dendritic spike (most likely NMDA type (Larkum, Nevian et al. 2009)). Next, the somatic  $\text{Na}^+$  spike initiation zone responds to the sum of the input from all dendritic branches (Polsky, Mel et al. 2004, Katz, Menon et al. 2009).

We, therefore, aimed to measure the distribution of excitatory and inhibitory synapses across the upper cortical layers for layer 2-5 pyramidal neurons' apical dendrite. The goal was to reveal the cell-type specific innervation patterns (see below). Next, we will describe the challenges to acquire and analyze 3D-EM datasets used for cellular resolution connectomics (Kleinfeld, Bharioke et al. 2011).

## **6.7. Methods to generate connectivity data in the cerebral cortex**

The goal of electron microscopy-based connectomics is to obtain a detailed cellular-resolution description of all neuronal wiring. The first step is to image a volume large enough to contain the whole dendritic and axonal arbors involved in a functional circuit at a sufficient resolution (About  $1 \text{ mm}^3$  in mouse cortex, (Briggman and Bock

2012, Kornfeld and Denk 2018)). However, the largest cubes densely reconstructed so far have an edge length of about 100  $\mu\text{m}$ . Furthermore, the resolution should allow for reconstruction of the thinnest processes in axons and dendrites (spine necks,  $\sim 50$  nm thick). To cover such thin processes with at least 2 voxels, one needs a resolution smaller than  $\sim 25$  nm along all three dimensions (Helmstaedter 2013).

In microscopes, the resolution ( $d$ ) is related to the wavelength ( $\lambda$ ) of the imaging agent used (photon or electron) and the numerical aperture of the objective lens system (NA) using the following relationship (Abbe 1883):

$$d = \frac{\lambda}{2 \times NA}$$

Light microscopy (LM) uses photons and is thus limited by the visible light's wavelength (300-700 nm). Therefore, the resolution limit for a traditional light microscope is about 200 nm in-plane and 500 nm axially (Gaussian beam under Abbe's criterion). Point objects closer than the limit cannot be resolved by a light microscope since their diffraction pattern overlaps. LM is therefore not currently used for dense reconstruction of cortical neuronal circuits. In combination with sparse labelling of neurons, LM could be used to study the structure of single neurons (Larkman and Mason 1990). For example, neuronal expression of fluorescent proteins is commonly used to map its regional brain-wide connectivity, also known as the "mesoscopic connectome" (Bohland, Wu et al. 2009, Oh, Harris et al. 2014). Furthermore, imaging by multiphoton excitation (Denk, Strickler et al. 1990) has made great strides in recording activity of large neuronal populations (Helmchen and Denk 2005, Weisenburger, Tejera et al. 2019). These methods in combination with the development of genetically encoded calcium sensors (Nakai, Ohkura et al. 2001, Chen, Wardill et al. 2013) allow investigators to monitor the activity of neurons in a wide variety of behavioral states (Dombeck, Khabbaz et al. 2007, Helmchen, Denk et al. 2013).

Recently, there has been a focus on overcoming the diffraction limit by combining optical and computational methods (Huang, Bates et al. 2009). These LM techniques rely on either a combination of spatially patterned excitation and stimulated emission (STED, (Hell and Wichmann 1994, Klar and Hell 1999)) or localization of

single molecules (PALM, STORM, (Betzig, Patterson et al. 2006, Hess, Girirajan et al. 2006, Rust, Bates et al. 2006)). In addition, expansion microscopy allows for resolution improvement by physically expanding fluorescent tissue labels using polymer substrates (Chen, Tillberg et al. 2015). However, technical challenges must be overcome before one or a combination of these methods satisfies the resolution limit (~25 nm) for dense circuit reconstruction (Huang, Bates et al. 2009, Helmstaedter 2013). Physical ultra-thin sectioning of the sample is used in array tomography to improve the axial resolution of light microscopy. This method is also used to combine light and electron microscopy imaging of the same set of brain sections (Micheva and Smith 2007, Bloss, Cembrowski et al. 2016).

Electron beams have a de Broglie wavelength that is proportional to the inverse square root of the voltage used to accelerate them (de Broglie 1925). The wavelength of electrons with energies of 1 and 100 keV is about 39 and 3.7 pm, the common energies used in scanning and transmission electron microscopy, respectively (Denk, Briggman et al. 2012). Therefore, electron microscopes (EMs) allow the imaging of neuronal circuits for dense reconstruction.

EMs are generally divided into transmission (Knoll and Ruska 1932) and scanning subtypes (von Ardenne 1938). Both types utilize the interaction of electrons with heavy metals deposited in the sample during the staining process as the contrast agent. In transmission electron microscopy (TEM), electrons passing through a thin sheath of the sample are diffracted differentially based upon the density of heavy nuclei. The final image is formed by the impact of electrons on the detector's surface. A charged-coupled device (CCD) detector is used in modern TEMs (example: (Bock, Lee et al. 2011)). Scanning electron microscopes (SEM) operate on the principle of raster-scanning a sufficiently small electron beam across the region of interest. Detection through transmission is used in special use cases (Pennycook and Nellist 2011). Backscattered or secondary electrons generated through beam interaction with a sample's atomic content is detected by a solid-state detector (backscattered electron detection) or a photomultiplier (secondary and back-scattered electrons, e.g. Everhart-Thornley detector (ETD), (Goldstein, Newbury et al. 2017)).

Electrons were reported to scatter significantly by biological tissue stained with heavy metals using Monte Carlo simulations (Hennig and Denk 2007). For example, Most electrons with an acceleration voltage of 6 kV have lost their ballistic path within the first 1  $\mu\text{m}$  of the sample surface (Kubota, Sohn et al. 2018). Even though high-voltage acceleration of electrons (400 keV) was used to reconstruct structures in “thick” (1-2  $\mu\text{m}$ ) sections by single-axis tomography, this method never gained popularity due to difficulties associated with back-projection reconstruction (Soto, Young et al. 1994). Therefore, current volumetric electron microscopy (3D-EM) methods combine serial imaging with ultra-thin (<50 nm) sectioning of the region of interest (Briggman and Denk 2006, Briggman and Bock 2012). One classification scheme for 3D-EM methods is based on whether the sectioning happens before (“serial section” methods, Figure 2a,b) or after (“block-face” methods, Figure 2c,d) imaging.

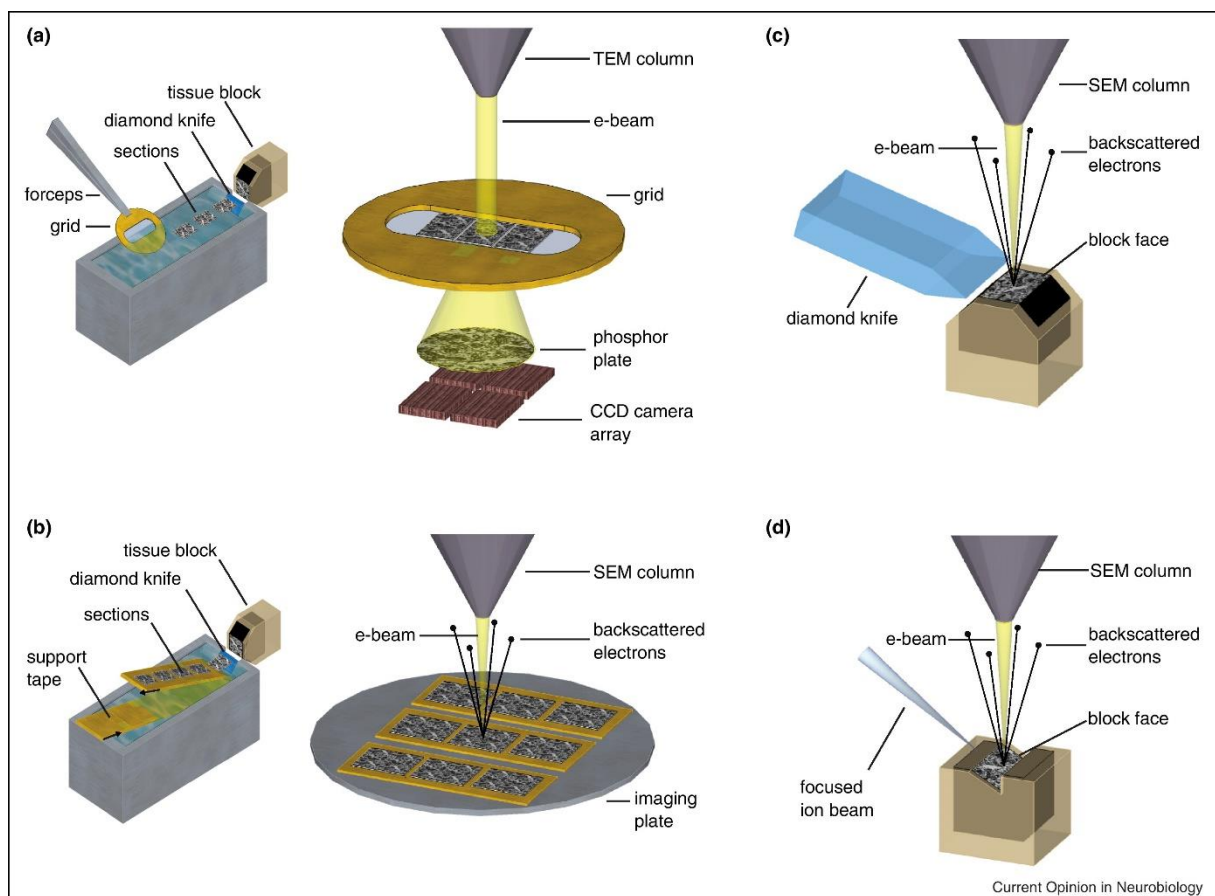


**Figure 2. Methods for 3D reconstruction of neuronal circuits using electron microscopes**

**(a)** TEMCA: Classical serial sectioning combined with high speed CCD camera arrays in TEM. **(b)** ATUM-SEM: tape support is used to automate section collection. The imaging is done by an SEM. **(c)** SBEM: Imaging steps are interlaced with removal of an ultra-thin section from the top of tissue block. Sectioning is performed by a diamond-knife microtome placed inside the SEM chamber. This is the method of choice in the thesis at hand. **(d)** FIB-SEM: similar to (c), but uses a focused ion beam to remove the ultra-thin section. Reprinted with permission from Elsevier: Current Opinion in Neurobiology (Briggman and Bock 2012), copyright 2012.

The classic serial section TEM (ssTEM) method relies on manually mounting ultra-thin sections (~40-50 nm) of a sample on TEM imaging grids (Figure 2a). First used in the 1950s to reconstruct the 3D ultrastructure of cellular components (Birch-Andersen 1955, Bang and Bang 1957), ssTEM was then utilized to reconstruct the complete connectome of the nematode *C.elegans* in a seminal study by White *et al.* (White, Southgate *et al.* 1986). In addition, ssTEM was the method of choice for investigation of the fine structural features of neurons, such as, synapses and dendritic spines (White and Hersch 1982, Harris and Stevens 1988).

ssTEM gained a significant boost in imaging speed with the addition of charge-coupled device (CCD) camera arrays (Bock, Lee *et al.* 2011) and methods to automate the laborious manual section collection using tape-based (similar to ATUM, see below) or accurate robotic systems (J. Lee, Kumar *et al.* 2018, Graham, Hildebrand *et al.* 2019). Sample loading into the microscope also benefited from reel-to-reel systems, which allow controlled random access to sections of interest (Mikula 2017).

EM-based connectomics was revolutionized by the addition of 3D-EM methods using scanning electron microscopes. SEMs, with their detection of back-reflected electrons from the sample surface, allow for imaging the block-face of a tissue before sectioning (Figure 2c, d). The initial block-face method used a miniaturized diamond knife ultra-microtome inside the chamber of a scanning electron microscope (SBEM, (Leighton 1981, Denk and Horstmann 2004)). The process of 3D volume acquisition then starts with imaging the block-face of a sample, followed by removal of the top ultra-thin section of the tissue block (typically ~20-35 nm). To reduce the axial

resolution below 25 nm, focused ion beams (FIB) were used to abrade thinner films of tissue (FIB-SEM, down to 4 nm in thickness, (Heymann, Hayles et al. 2006, Knott, Marchman et al. 2008)).

One significant break-through in serial sectioning was automation of section collection by using a tape-reel system added to a traditional ultra-microtome (ATUM, (Hayworth, Kasthuri et al. 2006)). ATUM allows for more reliable section collection and processing. Since the electrons cannot transmit through the tape, ATUM is used in combination with an SEM. ATUM is especially compatible with the current multi-beam SEMs that allow for large-scale imaging projects (volumes of about 1 mm<sup>3</sup>). Multi-beam SEMs increase the imaging speed 61-91X by increasing the number of parallel electron beams impinging on the sample surface (Eberle, Mikula et al. 2015).

The features of each 3D-EM method should be understood before choosing one for an experiment. Several reviews can guide your decision making process (Briggman and Bock 2012, Titze and Genoud 2016, Kornfeld and Denk 2018). In short, block-face imaging techniques benefit from reduced image deformations since the images are taken from the same block of tissue before any deformations are introduced by sectioning. You can approach the best isotropic resolution with FIB-SEM. However, this method is limited to tens of micrometers in-plane due to inconsistencies in the milling process for larger fields-of-view (FOVs). This limit could be overcome by reliable partitioning of the tissue into appropriate blocks with an ultra-sonicated, lubricated and heated (60 °C) diamond knife (Hayworth, Xu et al. 2015).

Recently, gas ion clusters were used to abrade large areas consistently with an axial resolution of ~10 nm (Hayworth, Peale et al. 2019). The prototype has shown promising results for isotropic (<10 nm) imaging of small volumes (tens of microns on each side). This method can, in principle, be applied to imaging of a 1 mm<sup>3</sup>.

On the other hand, the serial section methods (both ssTEM and ATUM-SEM) allow for repeated imaging of the same section unlike block-face approaches. This allows investigators to image the same tissue multiple times in case of microscope failure or to improve image quality (Kasthuri, Hayworth et al. 2015).



One method to improve signal and resolution in SEMs is to decelerate the electron beam by a negative bias on the sample. This bias reduces the solid angle of electron-backscattering that increases the probability of their collection by the solid-state detector's surface. The backscattered electrons are also accelerated towards the detector's surface, which increases the signal produced by their impact. In addition, low-energy secondary electrons (<50 keV) could be detected with an in-lens detector since the negative bias collimates them along the optical axis. Furthermore, this method reduces the chromatic and spherical aberrations, thus, increasing the achievable resolution for low-voltage imaging (Paden and Nixon 1968, Frank and Müllerová 1999, Phifer, Tuma et al. 2009, Titze and Denk 2013).

The diamond-knife block-face SEM method (SBEM) currently gives a balanced trade-off between resolution, volume and image quality. The main advantage is the full automation of the 3D image acquisition, nearly isotropic voxel size and limited deformation/artifacts in the image. The effective imaging speed for a single-beam SBEM has been pushed to about  $6 \times 10^6$  voxels/s using a combination of fast detection and piezo actuated continuous sample movement (Schmidt, Gour et al. 2017). The main disadvantage of SBEM is the accumulation of the sections cut from the sample block-face within the microscope chamber. This results in debris-beam interaction and requires careful failure detection software and microscope maintenance that are discussed in the following section.

## **6.8. Automated aberration adjustment for SBEM**

A SBEM set-up requires error-free operation over a few weeks to multiple months, depending on the volume and effective imaging speed. SBEM is a destructive method where previous sections cannot be imaged again. Therefore, errors where multiple sections are lost or imaged at low-quality would be catastrophic for the reconstructability of neurites. The thickness of lost tissue determines the thinnest process that can be reconstructed. Hence, the most common issues that are detrimental to SBEM experiments are: EM failures, such as, electron beam shutoff, stage motor failures, section cutting failures and image aberrations. Our goal was to correct for image aberrations automatically in SBEM during dataset acquisition.

The area of the beam cross-section at the surface of the sample should match the desired pixel size to get an optimal image in SEM. A larger beam area deteriorates the image resolution by averaging the signal over a larger sample volume. To achieve the best results in SEM, the beam area is minimized at the sample surface by changing the focal length of the objective lens and the strength of two stigmators. The stigmators allow for correction of the beam's rotational symmetry (second-order Zernike aberrations) by changing the magnitude of a quadrupole electromagnetic field perpendicular to the beam (Binding, Mikula et al. 2013). These aberrations affect the modulation transfer function (MTF) of the images by dampening the high-frequency spatial details of the image in a symmetric (defocus) or non-symmetric (destigmatation) manner.

The manual process to monitor image quality in a SBEM set-up is to review the output images frequently, interrupt the acquisition process when the aberration levels have dropped under a subjective threshold and adjust the focus and stigmatation parameters accordingly. This is a huge burden on the experimenter during month-long SBEM experiments and can only be used in systems where the failure rate is low.

The task of monitoring aberration levels in an EM depends on the robustness of the microscope to parameter changes. A major factor is the depth-of-focus where image resolution is acceptable. This is proportional to the beam's convergence angle ( $\alpha$ ). The gun brightness ( $\beta$ ) relates the depth-of-focus to the current ( $i$ ) and cross-section ( $d$ ) of the beam at the sample surface:

$$\beta = \frac{4 i}{\pi^2 d^2 \alpha^2}$$

EM systems designed to increase imaging speed by supplying high beam current (e.g., Magellan and Verios SEMs, FEI, USA) would have a smaller depth-of-focus ( $\sim 3 \mu\text{m}$  vs.  $\sim 10 \mu\text{m}$  for high-current vs low-current SEMs) assuming the same beam cross-section area. Therefore, high-current systems are less robust against changes in focus parameters. Additionally, immersion fields were introduced in high-current SEMs to decrease the solid angle and increase the energy of back-scattered electrons, which increases the signal generated in the solid-state detectors. However, immersion fields could possibly be distorted with electric fields emanating from charged

debris produced by the in-chamber sectioning process of SBEM. Moreover, large in-plane imaging requires multiple focus values for different parts since the sample surface is not fully orthogonal to the beam direction. Henceforth, automated adjustment of focus and stigmatism parameters is necessary in high-current SEMs.

Binding and colleagues introduced two methods for estimating aberrations in EM images (Binding, Mikula et al. 2013). The Bayesian approach (“MAPFoSt”) is beyond the scope of this thesis. We focus on a “heuristic algorithm” that uses the shape of the image autocorrelation to estimate three image aberration parameters (1 focus, 2 stigmators). This method has been additionally implemented in volume imaging software packages used for SBEM and FIB-SEM (Xu, Hayworth et al. 2017, Titze, Genoud et al. 2018). In addition to the microscope aberration parameters, the shape of the autocorrelation depends on the frequency spectrum of the imaged tissue. Therefore, the heuristic algorithm is sensitive to low-frequency features, such as, blood vessels and nuclei in 3D-EM images of neuronal tissue. To avoid these structures, we combined an edge detector with morphological operations to detect neuropil.

We describe a MATLAB (MathWorks, USA) implementation of the heuristic algorithm for the automatic adjustment of beam aberrations in SBEM (see Methods for details). Our method is the first, to our knowledge, to combine this algorithm with the masking of low-frequency blood vessels and cell nuclei.

## **6.9. Sample preparation for 3D electron microscopy**

The process of sample preparation begins with the vascular perfusion of aldehyde fixatives to preserve the ultrastructure of the brain tissue (usually a combination of paraformaldehyde and glutaraldehyde, (Hayat 1981)). Next, the tissue of interest is extracted and stained using the contrast agent (heavy metals) for electron microscopy.

The fraction of diffracted electrons increases monotonically with the atomic number of the elemental composition of sample. This factor is utilized to generate contrast in both 3D-SEM and TEM methods (Goldstein, Newbury et al. 2017). Therefore, the staining procedure aims to deposit heavy metals on cellular structures of interest, essentially lipids and proteins comprising the phospholipid membrane and

synapses. These structures allow for the reconstruction of neurites and their synapses. The heavy metals routinely used for EM staining of biological tissue are osmium (Os, (Palade 1952)), uranium (U, (Watson 1958)) and lead (Pb, (Venable and Coggeshall 1965)).

Application of the staining material can be performed on ultra-thin sections for ATUM and ssTEM, as the sectioning precedes imaging (Sato 1968). However, the staining material could cause sporadic damage to the sections and generate electron dense precipitates that hinder high-quality imaging (Kasthuri, Hayworth et al. 2015, Zheng, Lauritzen et al. 2018). Additionally, these methods are not compatible with block-face imaging. Therefore, a significant effort was put forth to improve *en-bloc* staining methods, which allow for staining the full volume of interest (Tapia, Kasthuri et al. 2012).

The method of choice for *en-bloc* staining of neuronal tissue was a sequential application of osmium tetroxide (initially reduced) interleaved with thiocarbohydrazide (TCH) as a linker agent until recently (ROTO, (Seligman, Wasserkrug et al. 1966, Willingham and Rutherford 1984)). This method was improved with the addition of uranium and lead staining steps and used in a seminal connectomic study of the retina (Walton 1979, Briggman, Helmstaedter et al. 2011). In ROTO, the penetration depth of the staining material is restricted to ~200  $\mu\text{m}$ , even though it generates a high level of membrane contrast within this penetration depth. The likely cause of the penetration limit is the generation of an electron dense barrier in the sample (Mikula, Binding et al. 2012, Hua, Laserstein et al. 2015). ROTO should be improved to allow for investigation of millimeter-sized neuronal circuits of the mammalian cortex.

A combination of reagent substitution and elongation of incubation steps was used to stain the whole mouse brain (Mikula and Denk 2015). However, this protocol requires ~2-3 months of staining for a single brain and a simple reduction of the incubation times does not result in proper staining of a cubic millimeter-sized sample (Genoud, Titze et al. 2018). Therefore, an initiative focused on modifying the osmium and uranium staining steps to increase penetration depth to 500  $\mu\text{m}$ , which allows for high-quality staining of samples with a diameter of 1 mm (Hua, Laserstein et al. 2015). The stained tissue is then dehydrated in a graded ethanol solution and infiltrated with

monomers of a plastic resin that polymerize in higher temperatures (e.g. Spurr's resin (Spurr 1969)).

## **6.10. Analysis of 3D-EM volumes for connectivity**

After acquisition of the 3D-EM volume, raw image files need to be aligned into a coherent 3D volume to reconstruct the 3D morphology of neuronal structures. Initial 3D-EM studies relied on manual contouring of the neuronal structures on printed EM images (White, Southgate et al. 1986). These methods were improved by computer software which allowed for manual alignment of images (Fiala 2005). A major breakthrough in automated alignment was the combination of shift vector measurement between neighboring image tiles with a global least-square relaxation process to find the optimal location for each tile (Preibisch, Saalfeld et al. 2009, Scheffer, Karsh et al. 2013). The shift vectors are usually estimated using error-prone cross-correlation or local feature detection. To improve shift vector estimation, learned algorithms were recently introduced (Mitchell, Keselj et al. 2019, Buniatyan, Popovych et al. 2020).

Next, the structures of interest need to be morphologically reconstructed and their synaptic connections of interest detected. Since, the detection of electrical synapses requires resolutions beyond current 3D-EM approaches (Rash, Yasumura et al. 1998) or the preservation of extracellular space (Pallotto, Watkins et al. 2015), we focus on the chemical synapses. The minimum volume required to extract cellular connectivity is dictated by the volume of dendritic and axonal arbors of connected neurons. The volume is about 1 mm<sup>3</sup> in the mouse neocortex (Helmstaedter 2013). This is also the goal of the Intelligence Advanced Research Projects Activity (IARPA) initiative to reverse-engineer cortical circuits to improve machine intelligence ([MICRONS](#), (Helmstaedter 2015)). 1 mm<sup>3</sup> is expected to contain about 92,000 neurons, 7 km of wiring (4 km of axons, 1 km dendrites and 2 km dendritic spines) and 1 billion synapses (Braitenberg and Schuz 1991, Staffler, Berning et al. 2017). Manual contouring requires about 200-400 human-hours per mm neurite length (Helmstaedter, Briggman et al. 2011) and the total time required to densely reconstruct a cubic mm would be about 240,000 human-years. Manual synapse annotation speed by volume

search is about  $0.1\text{h}/\mu\text{m}^3$ , which adds an additional 11,500 human-years. Therefore, methods to automate reconstruction are crucial for dense volume annotation.

A ~50-fold increase in neurite reconstruction speed was introduced by using the graph-like skeleton representation of neurons instead of the contouring approach (KNOSSOS, (Helmstaedter, Briggman et al. 2011)). A browser-based variant of KNOSSOS was developed, which allows for an egocentric flight through the EM volume without the need to switch between different orthogonal slices of the data (webKnossos, (Boergens, Berning et al. 2017)). Almost all the data generated in the current study is by skeleton reconstructions and synapse annotations in webKnossos since fully automatic reconstruction of neuronal structures is still under development.

To reach the goal of fully automated reconstruction of neural circuits, machine learning systems are developed. Machine learning is the study of learning algorithms for digital computers to perform a specific task without explicit instructions (Samuel 1959). One graphical model inspired by brain structure, and frequently used in machine learning, is artificial neural networks (Rosenblatt 1958). These networks consist of multiple layers of artificial neurons which act as non-linear operators on the weighted sum of their input (see (Lecun, Bengio et al. 2015) for a comprehensive review). A variant of this technique called convolutional neural networks (CNN, (LeCun, Boser et al. 1989)) has gained significant attention due to its superior performance in computer vision tasks (Krizhevsky, Sutskever et al. , Krizhevsky, Sutskever et al. 2012). This approach uses shared weights between neighboring elements in the hidden layers of the neuronal network to reduce the number of features that need to be learned (LeCun, Boser et al. 1989). The CNNs also surpassed other approaches in 3D segmentation of biological neuronal structures (Jain, Murray et al. 2007, Andres, Köthe et al. 2008, Berning, Boergens et al. 2015). The dense reconstruction of EM volumes, however, still requires correction by human annotators (Motta, Berning et al. 2019).

### **6.11. Impact of long-range input on pyramidal neurons (case study in S1)**

Projection neurons send long-range axons to cortical and subcortical regions and can be classified by their projection patterns in the brain (Winnubst, Bas et al. 2019). Interestingly, the majority (70-90%) of synapses within a cortical column have

a non-local source which highlights the importance of understanding long-range innervation patterns in cortex (Stepanyants, Martinez et al. 2009). One of the best studied models of long-range projections is the somatosensory whisker system in rodents (S1, (Aronoff, Matyas et al. 2010)).

In S1, sensory input from the thalamus mainly targets cortical layer 4 and the top-down feedback from other cortical/thalamic areas contact the apical dendrites of pyramidal neurons in layer 1 (Petreanu, Mao et al. 2009, Wimmer, Bruno et al. 2010). Additionally, L2/3 and L5 neurons in S1 were shown to control the activity of pyramidal neurons in the contralateral hemisphere through callosal projections. To inhibit their contralateral counterparts, L5 neurons recruit inhibitory interneurons in L1 to provide GABA<sub>B</sub>-mediated inhibition to apical dendrites (Petreanu, Huber et al. 2007, Palmer, Schulz et al. 2012).

A combination of anatomical and functional experiments revealed secondary somatosensory (S2) and primary motor (M1) cortices as two regions with prominent reciprocal connections to S1 (Mao, Kusefoglou et al. 2011, Ni and Chen 2017). The interaction between M1 and S1 extracts motor-related information, such as whisker position, movement initiation and adjustment of motor plans (Mao, Kusefoglou et al. 2011, Petreanu, Gutnisky et al. 2012, Ebbesen, Doron et al. 2017). In contrast, the interaction between S1 and S2 generates choice-related context from sensory information (Chen, Voigt et al. 2016, Ni and Chen 2017). Therefore, coordination of these three cortical regions is important for successful task completion.

Nevertheless, the functional description of long-range connectivity patterns across cortex lacks the cell-type specific wiring information that can be acquired using 3D-EM. This is because full mammalian brains are too large to be imaged using current 3D-EM techniques. Therefore, methods that supplement local synaptic wiring information in 3D-EM with the long-range source of axons are crucial for understanding cortical circuitry. The next sections describe “FluoEM”, a method to combine light and electron microscopy to achieve this goal and its application to posterior parietal cortex.

## 6.12. FluoEM: an ideal method to map long-range input in 3D-EM

Mammalian brain volumes that are large enough to contain complete long-range innervations cannot be imaged routinely with our current 3D-EM approaches (Briggman and Bock 2012). However, light microscopy is usually used to extract such information by expression of fluorescent proteins (Oh, Harris et al. 2014). A method to combine these two approaches without the need for label conversion (Gray and Hamlyn 1962, Zhang, Lee et al. 2019) or fiducial markings on the tissue (Bishop, Nikić et al. 2011) were not developed until recently.

The FluoEM method applies 3D fluorescent light (LM) and electron microscopy (EM) to a cortical region of interest (Drawitsch, Karimi et al. 2018). Axons within this block are labeled by anterograde fluorescent tracers injected into two or more input regions. Therefore, the long-range source of an axon is identified by the excitation wavelength of the fluorophore expressed in LM. Furthermore, all synaptic innervation information can be extracted from EM (Figure 3b). In FluoEM, the LM and EM datasets are initially aligned using markers, such as, blood vessels and/or neuronal cell bodies (Figure 3c). Axons annotated in the LM dataset are transformed into the EM coordinate system using the coarse registration ( $LM^T$ ). Next, the corresponding axon in EM is found by annotation of all axons contained within a bounding box surrounding the  $LM^T$  using only structural constraints (Figure 3d, e). FluoEM, therefore, allows for identification of the long-range source of axons in a limited EM volume by utilization of color-space in LM.



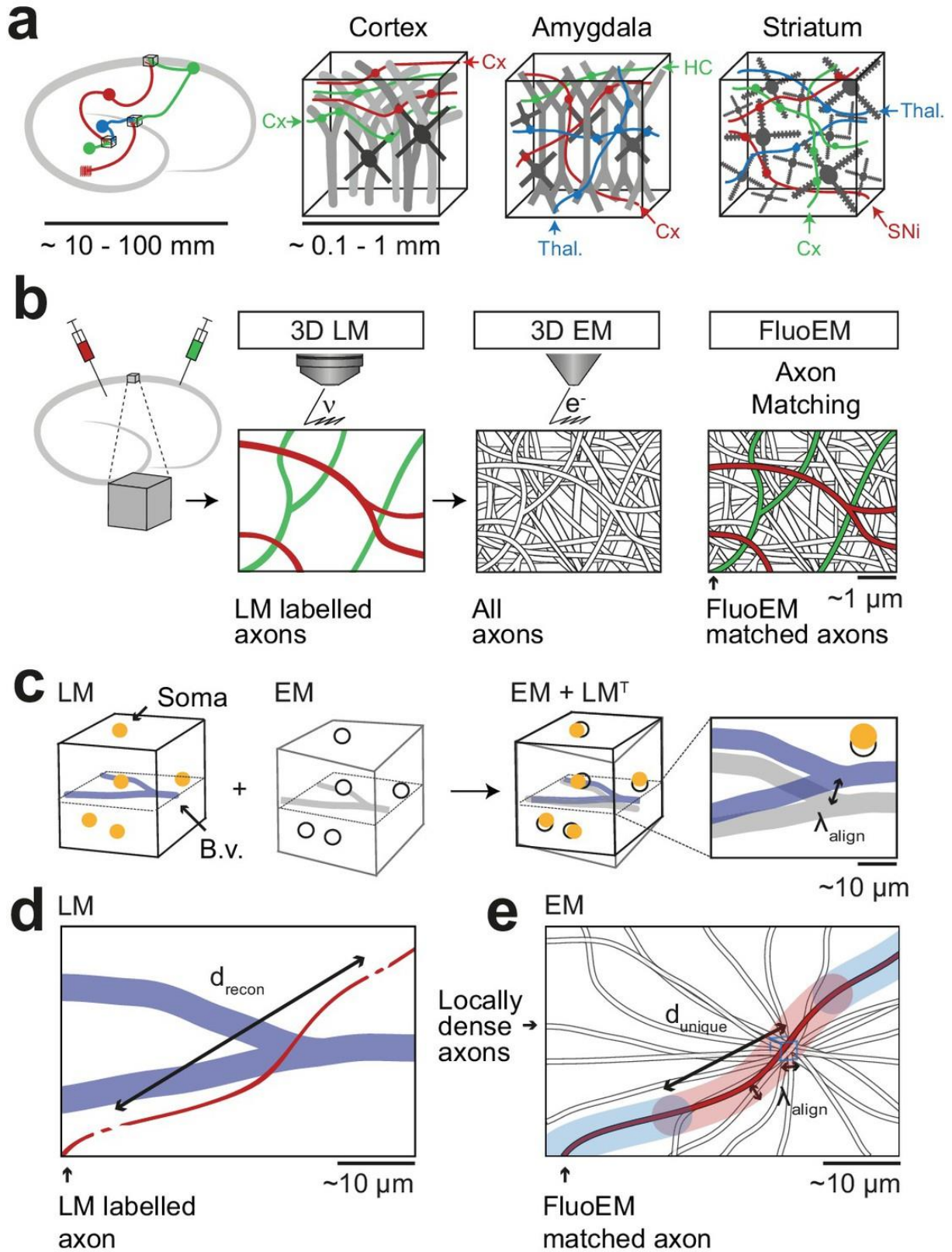


**Figure 3. Conceptual summary of FluoEM as a method for mapping long-range innervation using combined 3D light and electron microscopy**

**(a)** Brain regions can be mapped densely using modern 3D-EM methods with the source of most long-range input from other brain regions unknown, such as, Cortex (Cx), Thalamus (Thal.), Hippocampus (HC) and Substantia Nigra (SNi). **(b)** A block of tissue containing fluorescently labeled axons first imaged by confocal laser scanning light microscopy (LM), followed by 3D-EM. The fluorescently labeled axons are matched solely based on structural constraints without the need for electron-dense label conversion or fiducial markers. **(c)** The FluoEM approach starts with a coarse registration between EM and LM datasets using blood vessel and nuclei locations. **(d,e)** Axons are reconstructed in LM and transformed into the EM coordinate system using the transformation from (c). All axons within a bounding box surrounding the transformed axon are reconstructed in the EM dataset to find the unique axon with a matching trajectory. This figure is reproduced from (Drawitsch, Karimi et al. 2018) and is licensed under the CC BY 4.0.

### **6.13. Long-range input to posterior parietal cortex (PPC)**

The parietal cortex is defined as a set of cortical regions covered by the parietal bone. It is divided into the anterior somatosensory and posterior parietal cortex (PPC, (Whitlock, Sutherland et al. 2008)). PPC is located posterior to somatosensory and anterior to secondary visual areas, and it has reciprocal connections to both. It is defined in different animal models by cyto- and myelo-architecture (Krieg 1946), expression patterns of various neurotransmitters (Palomero-Gallagher and Zilles 2015), and most importantly, by its connectivity pattern to thalamus and other cortical areas (Kolb and Walkey 1987, Reep, Chandler et al. 1994).

PPC receives input from the associative thalamic nuclei (lateral posterior nucleus) and lacks unimodal somatosensory and visual thalamic input. In addition, PPC has reciprocal connectivity to almost all primary sensory cortices (e.g. somatosensory, auditory, and visual) and some associative cortices, such as retrosplenial cortex. PPC cortex is also connected to its contralateral counterpart through the callosum (Reep, Chandler et al. 1994, Harvey, Coen et al. 2012).

PPC is involved in various aspects of spatial perception. Human patients with lesions in PPC show a lack of spatial understanding (Lynch 1980). In non-human

primates, electrophysiological recordings of PPC neurons demonstrated their role in decision making (Gold and Shadlen 2007), spatial attention (Bisley and Goldberg 2010) and action planning. Similarly in rodents, PPC was shown to be involved in various aspects of navigation and decision making (Nitz 2006, Harvey, Coen et al. 2012, Whitlock, Pfuhl et al. 2012). A recent study recorded activity of neurons in PPC, primary visual (V1) and premotor (M2) cortices during a memory-guided visual discrimination task (Goard, Pho et al. 2016). Neurons in V1 and M2 encode stimulus and choice information, respectively, with PPC neurons encoding the mixture. We, therefore, decided to map long-range innervation to PPC from these two input cortical regions (see results below).

## 6.14. Outlook and contributions

The superficial cortical layers are an interesting region for connectivity analysis as the apical tuft dendrites of pyramidal neurons coincide within the same spatial region innervated by different excitatory and inhibitory axons (Figure 5a). We, therefore, acquired six 3D-EM datasets from 5 cortical regions<sup>2</sup> and annotated 31,996 synapses formed by the apical dendrites or the inhibitory axons innervating them<sup>3</sup>. Our goal was to understand whether inhibitory axons innervate different apical dendrite types in a specific manner by measuring their conditional innervation probability. We also quantified the distribution of excitatory and inhibitory synapses onto apical dendrites across the upper cortex to reveal cell-type specific innervation patterns. Finally, we analyzed the cell-type preference of long-range projections to posterior parietal cortex using a combination of large-scale volumetric light and electron microscopy.

---

<sup>2</sup> The LPtA, ACC and S1 datasets were acquired by Florian Drawitsch, Jan Odenthal and Kevin Boergens, respectively. All other datasets were acquired by the author.

<sup>3</sup> All skeleton reconstructions and synapse annotations were performed in collaboration (equal contributions) with Jan Odenthal. All analysis and figure preparations were done by the author with input from colleagues (see acknowledgements).

## **7. Materials and Methods**

### **7.1. Volumetric electron microscopy imaging of cortex**

#### **7.1.1. Animal experiments**

Performance of all experimental procedures was in accordance with the law of animal experimentation issued by the German Federal Government under the supervision of local ethics committees and according to the guidelines of the Max Planck Society. The experimental procedures were approved by the Regierungspräsidium in Darmstadt, under protocol ID V54 - 19c20/15 F126/1015 (LPtA, PPC-2) or V54 – 19 c 20/15 – F126/1002 (V2, PPC, ACC). Preparation of the S1 sample followed experimental procedures approved by the Regierung von Oberbayern, 55.2-1-54-2532.3-103-12.

#### **7.1.2. S1, LPtA sample preparation**

The experimental and computational procedures for preparation of the S1 (Figure 4, acquired by Kevin Boergens) and LPtA (Figure 6, acquired by Florian Drawitsch) datasets were described previously in (Berning, Boergens et al. 2015) and (Drawitsch, Karimi et al. 2018), respectively. The V2, PPC, ACC (Figure 4, acquired by Jan Odenthal) and PPC-2 samples were processed as follows.

#### **7.1.3. Transcardial perfusion**

Wild-type adult mice (species: C57BL/6J, age (postnatal days): 56 – 57) were injected with general analgesia (0.1 mg/kg buprenorphine (Buprenovet, Recipharm, France and 100 mg/kg Metamizol (Metamizol WDT, WDT, Germany)). Animals were then anesthetized by inhalation of isoflurane (3 – 3.5% in carbogen) and perfused with 15 ml of cacodylate buffer (150 mM, Serva, Heidelberg, Germany, pH = 7.4) followed by 30 ml of fixative solution through the left ventricle (flow rate of 10 ml/min). The fixative solution was 2.5% PFA (Sigma-Aldrich, Germany), 1.25% glutaraldehyde (Serva) and 0.5% CaCl<sub>2</sub> (Sigma-Aldrich) in 80 mM cacodylate buffer (pH = 7.4). The animal was decapitated and the skull was removed to expose the brain. The exposed brain was then submerged in fixative solution overnight at 4 °C.

#### **7.1.4. Cortical region targeting and tissue extraction**

A coronal slice containing the region (600  $\mu\text{m}$  thick) of interest was acquired using a vibrating microtome (Microm HM 650V, Thermo Fisher Scientific, USA), guided by a reference atlas (Franklin and Paxinos 2008). We then used a biopsy punch (1 mm in diameter, KAI medicals, USA) to extract a cylindrical block of cortex containing layers 1-3. This block was then incubated for 3 - 4 hours (V2, PPC and ACC) or overnight (PPC-2) in cacodylate buffer. The remainder of the coronal slice was sectioned at a thickness of 100-150  $\mu\text{m}$  and imaged by a wide-field light microscope (Leica MZ10 F, Leica, Germany) for post-hoc qualitative comparison to the reference atlas (Figure 4c, Figure 6b). The approximate coordinate of each dataset relative to bregma is given in Table 1. The PPC-2 sample was also subjected to confocal laser scanning light microscopy as described below.

#### **7.1.5. Electron microscopy dataset names**

Dataset names match the cortical region from which they were sampled from. The exception was the larger of the two datasets taken from posterior parietal cortex (PPC and PPC-2, Figure 4 and 6, respectively).

#### **7.1.6. En-bloc sample preparation for 3D electron microscopy**

Samples were stained and embedded in plastic for serial block-face electron microscopy, following an *en-bloc* technique slightly modified from (Hua, Laserstein et al. 2015). Note that all procedures were performed at room temperature in 2 ml reaction tubes (Eppendorf, Germany) unless stated otherwise. In addition, the initial incubation steps (until dehydration) were performed with the aid of an automatic microwave tissue processor (Leica EM AMW, Leica, Germany, V2, PPC, and ACC samples) or manually (PPC-2).

In short, cortical tissue was rinsed in cacodylate buffer for 30 min before any staining material was applied. Next, it was transferred to 2%  $\text{OsO}_4$  (Serva, Germany) in cacodylate buffer for 90 min. The sample was then treated with 2.5% ferrocyanide (Potassium hexacyanoferrate trihydrate, Sigma-Aldrich, Germany) in cacodylate buffer for 90 min and 2% buffered  $\text{OsO}_4$  for 45 min. We then rinsed the tissue in cacodylate and ultrapure water for 30 min each. Osmium content of the sample was amplified by

treatment with saturated aqueous thiocarbohydrazide (TCH, Sigma-Aldrich, Germany) and 2% aqueous OsO<sub>4</sub> for 60 and 90 min, respectively. Subsequently, the sample was moved to 2% uranyl acetate solution for overnight incubation at 4 °C. The following day, the tissue, still in uranyl acetate, was heated to 50 °C for 120 min in an oven (Mettler, Germany). This was followed by incubation in lead aspartate at 50 °C for 120 min. The lead aspartate solution was prepared by dissolving 0.066 g lead nitrate (Sigma-Aldrich, Germany) in a 10 ml 0.03 M aspartic acid (Serva, Germany) solution and adjusting the pH to 5.0 (pH error < 0.1). Treatment steps (from TCH application) were interleaved with two 30 min washing steps in ultrapure water (Biochrom, Germany).

Next, the cortical tissue was dehydrated by incubation in 50%, 75% and 100% ethanol solutions (Serva, Germany). This was followed by at least three 20-45 min incubation steps in acetone (Serva, Germany). The sample was then transferred to a 1:1 mixture of acetone and Spurr's resin (4.1 g ERL 4221, 0.95 g DER 736 and 5.9 g NSA, 113 µl DMAE, Sigma-Aldrich, Germany) for 3-4 hours. Tubes were opened to allow for acetone evaporation overnight (V2, PPC and ACC samples). At this stage, the PPC-2 sample was transferred to a 3:1 mixture of Spurr's resin and acetone. The following day, the sample was further incubated for two 3-hour (PPC-2) or one 6-hour (V2, PPC, ACC) period in undiluted Spurr's resin mixture. The tissue was then transferred to a flat-embedding mold and cured at 70 °C for at least 48 hours. Specific time and temperature of dehydration and embedding steps are detailed in Table 2.

#### **7.1.7. Serial block-face electron microscopy (SBEM)**

The samples were removed from the resin block using a rotating saw blade in the trimming machine (Leica EM TRIM2, Leica, Germany) and mounted onto a cylindrical aluminum pin (designed to fit the sample holder on the SBEM microtome) using epoxy glue (Uhu plus schnellfest, Uhu, Germany). The block-face of the sample was trimmed down to an area of ~ 750 µm x 750 µm using a diamond-head trimming machine (Leica EM TRIM2). In addition, tissue was sputter coated with a 100 - 200 nm layer of gold (Leica ACE600 Sputter Coater, Leica, Germany) to increase surface conductivity and reduce the artifacts from local charge accumulation.

The SBEM microtome (courtesy of W. Denk) was fit inside the door of a scanning electron microscope (Table 1, FEI, Thermo Fisher Scientific, USA). The microtome and microscope were controlled using custom-written software during the volume imaging process; focus and stigmatism were corrected either manually (V2, PPC, ACC and LPtA) or by using custom-written auto-correction routines (see below, S1, PPC-2). The region of interest was imaged using overlapping image tiles and cutting direction was along the tangential (S1, V2, PPC, ACC, PPC-2) or radial (LPtA) cortical axes. The region-of-interest was targeted close to the layer 1/2 border (S1, V2, PPC and ACC, Figure 4a). The final imaged volume and the nominal voxel size is detailed in Table 1. Note that the LPtA and PPC-2 datasets were adjacent to low-resolution datasets extending to the middle of layer 5 (voxel dimensions of 22.48 x 22.48 x 30 and 44.96 x 44.96 x 120 nm<sup>3</sup> for PPC-2 and LPtA, respectively).

The dataset from PPC intended for the correlative light and electron microscopy (“FluoEM”) study (PPC-2) was composed of two high-resolution (voxel size: 11.24 x 11.24 x 30 nm<sup>3</sup>, volumes: 200 x 185 x 200 and 200 x 370 x 100 μm<sup>3</sup>) and one low-resolution (voxel size: 22.48 x 22.48 x 30 nm<sup>3</sup>, volume: 250 x 581 x 200 μm<sup>3</sup>) adjacent cubes (Figure 6a, right panel). The PPC-2 dataset was continuous along the cutting direction with one exception: scanning electron microscopy repair procedures resulted in a discontinuity at ~177 μm depth (between image planes 5886 and 5887), such that only dendrites thicker than ~1 μm (e.g. apical dendrites) were traceable.

#### **7.1.8. Image alignment**

The alignment of the PPC, V2 and ACC datasets was done using custom-written MATLAB (Mathworks, USA) routines (Briggman, Helmstaedter et al. 2011), which roughly followed (Preibisch, Saalfeld et al. 2009). In short, we used cross-correlation or speeded up robust feature (SURF) detection in the overlap region to measure the relative shift between image patches. These patches were full image tiles (V2, ACC) or tile sub-regions (PPC, 256 x 256 pixels). The position of each patch was then globally optimized using least-square regression.

Regions with high residual error were inspected for erroneous feature matches. Miscalculated shift vectors were down-weighted and the global least square was repeated until the highest residual was below a specific threshold (~10-20 pixels). The

image volume was then partitioned into 1024x1024x1024 voxel blocks and transformed into webKnossos-wrapper format files ([WKW](#)) for efficient 3D access. It was then transferred to the data store accessible by webKnossos for in-browser skeleton reconstruction and annotation (Boergens, Berning et al. 2017).

The PPC-2 dataset was aligned using a modified version of an affine alignment method. In short, this algorithm uses a gradient ascent on the cross-correlation result of the overlapping region between two image tiles while one is deformed. The ensuing matched features are point-pairs. These point-pairs are then used as constraints in a parallel implementation of a least squares algorithm to find the optimal affine transformation for each image tile (Scheffer, Karsh et al. 2013).

The C++ routines were modified to give unique affine transformations to each sub-region of size 1868x2148 pixels<sup>2</sup> (2x2 sub region per tile, 200 pixels of overlap, original tile size: 4096x3536 pixels<sup>2</sup>). This allows for non-affine transformations on the scale of a full tile, yet corrected with locally affine transformations. We also added MATLAB routines to generate WKW files from the final dataset for efficient 3D access.

In addition, we extracted a mask for blood vessels and cell nuclei by using the Canny edge detector (Canny 1986) and morphological operations from the [OpenCV](#) library (version 3.4.1). Nuclei and blood vessels are larger structures, detectable as blobs with a lower density of edges compared to the surrounding neuropil (Figure 21d, EM micrographs of nuclei and neuropil). These regions are excluded since they generate erroneous feature matches between neighboring image tiles. Furthermore, we added the option to output intermediate results at each step of the mask creation to allow for optimizing the algorithm parameters ( $n = 7$ ) for new datasets. However, convolutional neural networks trained to detect blood vessels and nuclei with higher accuracy and robustness against differences between datasets would be the reasonable next step (e.g. see (Januszewski, Kornfeld et al. 2018)).

We used this pipeline to also align a dataset from the hippocampal dentate gyrus (Table 6, acquired and aligned by Dr. Marcel Beining, voxel size: 11.24 x 11.24 x 28 nm<sup>3</sup>, dataset dimensions: 322 x 207 x 200  $\mu$ m<sup>3</sup>). Furthermore, a modified version of this pipeline was successfully used to align a dataset of size ~0.5 mm<sup>3</sup> (acquired and aligned by Meike Schurr).



### **7.1.9. Estimating EM beam aberration parameters using image autocorrelation**

Our approach closely follows the “heuristic algorithm” reported in (Binding, Mikula et al. 2013) that makes use of the way aberration changes the Fourier spectrum of images. Focus and astigmatism result in rotationally symmetric and asymmetric loss of higher frequencies in the image, respectively (Figure 21a-b). To get an unbiased estimator of the three actual aberrations (1 defocus and 2 astigmatism), two images were acquired with test (T) aberrations (T+ and T- images with a defocus of +0.6 and -0.6  $\mu\text{m}$ ). In SBEM experiments, sequential slices were used since 0.6  $\mu\text{m}$  of defocus has a negligible effect on image quality.

The images were then cropped to a region of 1024 x 1024 pixels<sup>2</sup> to calculate the autocorrelation avoiding blood vessels and nuclei (see section below for neuropil detection). Next, the dot-product of a central 64 x 64 pixel region of the autocorrelation image was calculated against six weight masks (2 per aberration, Figure 21c). The masks were designed to capture the shape of the autocorrelation image and dot-product pairs were used to estimate single-image defocus and astigmatism.

The difference of the single-image aberrations between two test images (T+ and T-) were uncalibrated estimators of the actual aberrations. We, therefore, needed to experimentally measure the calibration parameter for each estimator. However, the estimated linear relationship to actual aberrations was dependent on the sample’s frequency spectrum and microscope settings. In our experience, the method was robust against minor changes in image texture between brain regions (Figure 21, Table 6). Furthermore, the two astigmatism parameters were rotated to match the coordinate system of the microscope’s stigmator elements, which differ between individual microscopes.

The objective lens has a variable distance to the sample surface that is tilted relative to the path of electron beam. Therefore, it was necessary to allow for individual focus parameters in  $\sim 100 \times 100 \mu\text{m}^2$  sub-regions of the imaging field-of-view.

### **7.1.10. The detection of large objects in EM micrographs**

The frequency dependence of the aberration adjustment software allowed for spurious result when the imaged sub-region was a large object, such as, blood vessels

and nuclei. It was, therefore, necessary to detect and avoid these objects. First, we smoothed the image using a Gaussian kernel ( $100 \times 100 \text{ nm}^2$ , standard deviation = 90 nm) and applied the Canny edge detector (Canny 1986). Next, we used morphological operations based on heuristics to create a binary mask for the nuclei and blood vessels. The binary mask was distance-transformed and the pixel region used for automatic aberration adjustment was centered on the maximum distance from binary mask in the image tile (Figure 21d). All software for automated aberration and detection of large objects were written in MATLAB 2014-2016a (Mathworks, USA).

## **7.2. Cell-type specific innervation of apical dendrites**

### **7.2.1. Skeleton reconstruction and synapse annotation**

Skeleton reconstructions are tree-like graph representations (collection of nodes and edges) of the path neurites take in 3D space (e.g. Figure 7). In webKnossos, each reconstruction node accepts a comment string used to note the location of cellular structures, such as, synapses. The skeleton reconstruction and synapse annotations were downloaded as NML files (XML-based file format). NML files were subsequently parsed into a MATLAB class (MathWorks, USA, release 2014b-2019a) containing node and edge properties of each neurite. These properties were used to visualize (e.g. Figure 9a) and extract various features of the annotations (e.g. Figure 5c-f, number of synapses and path length).

### **7.2.2. Apical dendrite (AD) definition and classification**

In PPC-2 and LPtA datasets, pyramidal neurons were identified by the pyramid shape of their cell body, their axon initial segment's (AIS) direction towards white matter (WM), spiny dendrites (apart from peri-somatic region) and their apical dendrite trunk directionality (towards pial surface) and diameter ( $\sim 1\text{-}3 \text{ }\mu\text{m}$ , Figure 16b, d, e, (Larkman and Mason 1990)). Next, the AD shaft was reconstructed around the main bifurcation (Figure 9) or distal apical dendrite tuft (Figure 10) for local dense synaptic input mapping. The range of depth used for classifying pyramidal neurons into layers 2-5 subtypes was reported in Table 5. Note that, LPtA and PPC cortical regions do not possess a prominent layer 4 (Kolb and Walkey 1987).

The difference between nominal and actual cutting thickness in the LPtA dataset resulted in compression of spherical somata into ellipsoids along the cutting axis. Therefore, the section thickness was corrected (by a factor of 1.49) to obtain an accurate estimate of somatic depth relative to pial surface, assuming spherical somatic shape.

To get a direct estimate of the pial surface in the PPC-2 dataset, we used the difference in auto-fluorescence of the fixed brain tissue and its surrounding buffer. Using this brightness difference, we placed nodes on the approximate location of the pial surface. We next transformed the nodes into EM space and regressed their coordinates to estimate pia as a 2D linear plane. The Euclidean distance to the pial 2D plane was used as the somatic depth (Table 5). Additionally, we estimated the L1/2 border surface using the PPC-2 dataset following a similar procedure.

Within the S1, V2, PPC and ACC datasets, ADs were classified depending on the existence of soma in the image volume (Figure 4a). ADs with soma in the image volume were classified as layer 2 (L2) and other apical dendrites were classified as deep layer (L3/5, DL) ADs. The deep class of ADs was only identified based on their radial direction and diameter (Figure 4a, 5b). To augment the diversity of ADs analyzed within this study, we specifically searched for layer 2 and 5 pyramidal subtypes where ADs were either obliquely directed or thin. We identified two subtypes for L2 and L5 pyramidal neurons (Figure 9, also see below).

The main bifurcation of apical dendrites was defined as the branching point with two daughter branches of similar thickness and branching angle (resulting in a “Y” shape, Figure 5b).

The ACC dataset was used to reconstruct all ADs within one EM volume (Figure 5a, blue-green). They were detected by examining the dataset border facing WM for deeper layer ADs ( $n = 152$ ), and by identifying all L2 pyramidal neurons for the L2 ADs ( $n = 61$ ). The AD locations were used as seed points for manual annotation by student annotators ignoring spines.

### **7.2.3. Identification of layer 2 marginal (L2MN) and slender-tufted layer 5 (L5st) neurons**

Our goal was to find known subtypes of apical dendrites that were not investigated due to our AD identification process described above. AD morphology, contained in the low- and high-resolution EM volume, was reconstructed for all investigated neurons in LPtA and PPC-2 datasets (Figure 7). We then specifically searched for layer 2 marginal (L2MN) and slender-tufted layer 5 pyramidal neurons (L5st).

To identify L2MN neurons, we searched the L1/2 border region for pyramidal neurons that have an AD obliquely directed relative to pial surface (Figure 7a, 9a, black reconstructions (Larkman and Mason 1990, Luo, Hasegawa et al. 2017)).

We also reconstructed additional L5 neurons with a slender apical dendrite tuft morphology (Figure 7, blue reconstructions). We used soma diameter, AD trunk diameter, number of oblique dendrites and the depth of main bifurcation as parameters that were previously reported to distinguish L5 subtypes (Larkman and Mason 1990, Groh, Meyer et al. 2009). Our goals was to classify L5 neurons by agglomerative hierarchical clustering. We, therefore, used the correlation coefficient between height of the link between clusters (cophenetic distance) and their actual distance in the 4-dimensional feature space to find the optimal linking function. We found the average of “cosine” distance (One minus the cosine of the angle between points) to create the most consistent tree with the distance of clusters in the original feature space.

We then created two clusters containing L5st ( $n = 11$ ) and L5tt ( $n = 7$ ) neurons. The feature distribution of the two clusters corresponded to previous definition of L5 neuronal subtypes (Hübener and Bolz 1988, Hübener, Schwarz et al. 1990, Manns, Sakmann et al. 2004). The L5tt neurons had a larger soma and AD diameter with higher number of oblique dendrites and a deeper bifurcation relative to pial surface as compared to L5st neurons (Figure 8a). To approximate the soma volume using an ellipsoid, we measured the diameter along the three Cartesian dimensions of the dataset. We then calculated the diameter of the sphere that has an equivalent volume. To measure AD diameter, we determined the diameter of the circle that has an

equivalent area to the ellipse approximation of the AD trunk cross-section. The diameter was measured about 50  $\mu\text{m}$  from the cell body.

We also performed principal component analysis (PCA) on the morphological features of L5 neurons. The first principal component (PC 1) was correlated with thick-tuftedness of pyramidal neurons (Figure 8b, d). Therefore, PC 1 was used to investigate the correlation of synaptic densities and the morphology of L5 neurons. We fitted linear models to each synaptic density. Additionally, we used a fraction of two linear models to explain the relationship between fraction of inhibitory synapses and L5 morphology (Figure 8e, solid black line). To understand the variance explained by individual synapse densities, we used the linear model fit to either or both synapse densities to create predictions on the inhibitory fraction (Figure 8e, dashed lines). In these models, the average of the other synapse density was used to calculate the inhibitory fraction. Finally, we compared the spine density and somatic depth of L5 pyramidal neurons (Figure 8c, f).

#### **7.2.4. Complete synaptic input mapping of apical dendrites**

Apical dendrites and their dendritic spines were skeleton-reconstructed and the synapses on their shaft and spines were annotated within a bounding box of size  $20 \times 20 \times 20 \mu\text{m}^3$  around the main bifurcation (Figure 5, 9,  $n = 20$  for S1, V2, PPC,  $n = 40$  for PPC-2,  $n = 22$  for ACC) or distal apical dendrite tuft (Figure 10a,  $n = 6$  L5st group in PPC-2). Further, we also performed dense synapse annotation throughout the high-resolution EM datasets for a few ADs by an expert annotator (Figure 10a (except for the L5st group),  $n = 11$  for LPtA,  $n = 6$  for ACC,  $n = 4$  for S1, V2 and PPC). See Figure 12 for all annotated synapses.

Chemical synapses were identified within the data set based upon the presence of vesicle cloud and postsynaptic density, as described previously (Gray 1957, Schmidt, Gour et al. 2017). We also noted cases where spine neck or head received an additional synapse (Figure 14c). The co-innervation of spines with excitatory and inhibitory synapses was reported for thalamic input to cortex (Kubota, Hatada et al. 2007). Shaft synapses, synapses on spine necks and secondary spine head innervations were counted as inhibitory synapses, and primary spine innervations were counted as excitatory synapses for majority of neuron types. Justification for the

identification criteria of synapses were provided using structural constraints below (Total error rate was below 4% with the exception of L5st neurons, Figure 5, 9, 10).

Synapse and skeleton annotations were done in collaboration with Jan Odenthal. In our analysis, we only included possible synapses that met our criteria according to both expert annotators (AK and JO).

The fraction of inhibitory synapses was defined as the number of inhibitory synapses divided by the total number of synapses for individual ADs (Figure 5e, f, 9b, 10b, 13b). The inhibitory and excitatory synapse density was calculated by dividing the number of synapses by the path length of the apical dendrite shaft (Figure 5c, d, 9c, 10c, 13a). Shaft path length was measured by removing the spine necks from the skeleton reconstructions and summing the lengths of the remaining edges. Note that inhibitory input was measured separately for each distal tuft branch in the LPtA and PPC-2 datasets, resulting in 9, 7, 9, 6 dendritic segments for L2, 3, 5tt and 5st cells, respectively (Figure 10).

#### **7.2.5. Inhibitory input fraction mapping in upper cortex**

We first estimated the location of each dataset relative to pia by measuring the distance to pial surface in the coronal overview EM images. Distances were 125, 215, 170, 110, 10, 20  $\mu\text{m}$  for S1, V2, PPC, ACC, PPC-2 and LPtA, respectively (Figure 4, 6). We then transformed all the dense synaptic input maps into a common coordinate system with the second dimension (Y-axis) representing the distance to pia (Figure 12). Next, we partitioned the reconstructions ( $n = 141$ , total AD shaft path length = 14.1 mm) into virtual 100  $\mu\text{m}$  thick cortical tangential sections. This process resulted in dendritic segments at each depth bin. We then combined synapse counts and path lengths from all segments within each virtual cortical section to calculate the pooled mean for inhibitory fraction and synapse densities at that depth (lines in Figure 13a-b). We also used the 95% bootstrap confidence interval to estimate the dependence of the pooled average on the sample composition (shades in Figure 13a-b,  $n = 10,000$  bootstrap samples).

### **7.2.6. Distance to soma and synapse composition at the main bifurcation**

We annotated the path between soma and main bifurcation within the high- and low-res EM data volumes for the L2 ( $n = 51$ , datasets: S1, V2, PPC, ACC, PPC-2), L2MN ( $n = 2$ , PPC-2), L3 ( $n = 10$ , PPC-2), L5tt ( $n = 7$ , PPC-2), and L5st ( $n = 11$ , PPC-2) pyramidal cells. The path distance between soma and main bifurcation was plotted against the synaptic densities at the main bifurcation (Figure 11a-c).

### **7.2.7. Inhibitory fraction along L2 apical dendrites**

The excitatory and inhibitory synapses were binned based on their path distance to soma in the reconstructed L2 pyramidal ADs ( $n = 61$ ,  $n = 12,532$  synapses, bin size = 10  $\mu\text{m}$ ), allowing us to measure the fraction of inhibitory synapses as a function of dendritic path distance to the soma (Figure 11d-e, 10-330  $\mu\text{m}$  distance range). Soma distance bins with less than 4 synapses were merged to their immediate neighbors that contained at least 4 synapses. This was done to avoid extreme values introduced by computing the inhibitory ratio in bins with low synapse count.

### **7.2.8. Identity estimation for shaft and spine synapses**

A random subset of axons targeting shaft or dendritic spines of ADs was reconstructed in layers 1 and 2 ( $n = 142$ , 288, respectively, Figure 15a). The postsynaptic targets were identified for 2 to 405 additional targets of each axon (median of 7 synapses). Next, we classified the postsynaptic target as single-innervated spine head or shaft/non-spine that included spine neck, double-innervated spine and soma innervation. Next, we plotted the histogram (bin size = 0.1) and the probability density estimate (bandwidth = 0.0573) of the fraction of single-innervated spines (Figure 15b).

We used a threshold ( $=0.5$ ) on the single-innervated spine innervation fraction to classify axons into excitatory (spine-preferring) and inhibitory (shaft/non-spine preferring) types (Figure 15b, dashed lines). Next, we measured the prediction accuracy of the presynaptic axon (spine- vs. shaft-preferring) based on the location of the synapse on the dendrite (spine vs. shaft, Figure 15c, Table 4). Since the L5st neurons had a significant spine-preferring (likely excitatory) input to their shafts, we

corrected their synaptic densities using our prediction accuracies (Figure 9, 10, grey and blue crosses are values pre- and post-correction).

#### **7.2.9. Synapse size estimation**

A random subset of synapses onto shaft and dendritic spines ( $n = 41$  per AD type) were used to compare the synaptic interface area between L2 and deep layer AD main bifurcations (Figure 14b, S1, V2, PPC and ACC datasets). For this, an expert annotator placed two edges along the longest dimension of the synapse and its approximate orthogonal direction. These two edges were used as the minor and major axes of an ellipse to estimate the contact area (Figure 14a,  $area = \pi * semi - major axis * semi - minor axis$ ).

#### **7.2.10. Spine apparatus at the main AD bifurcation**

We inspected a randomly selected subset of spines from the main bifurcation of L2, L3 and L5tt neurons for presence of spine apparatus ( $n = 20$  per cell type, PPC-2 dataset). We reported the fraction and density (per  $\mu m$  shaft path length of AD) of spines with an apparatus (Figure 14d).

#### **7.2.11. Apical dendrite diameter and synapse density per unit surface area**

The apical dendrite diameter was measured every  $\sim 2-3 \mu m$  along the path used for dense synaptic input mapping (Figure 16a). The average diameter (Figure 16b, d, e), in combination with the path length of the dendrite, was used to calculate the surface area of the dendrite (AD surface =  $\pi \times path\ length \times average\ diameter$ ). Next, the synapse number was normalized to the surface area of the dendrite to generate synapse density per unit surface (Figure 16c, d, e).

#### **7.2.12. Conditional innervation probability of inhibitory axons**

We selected a random subset of shaft synapses (the “seed” synapses) from layer 2 ( $n = 21, 20, 21, 30$  for S1, V2, PPC and ACC) and deep layer ADs ( $n = 19, 20, 20, 32$  for S1, V2, PPC and ACC). An expert annotator reconstructed the path and annotated all synapses and postsynaptic partners of the pre-synaptic axon. The reconstructions were then revised by another annotator for morphological irregularities,



such as, sharp branching angles and untraced endings. All axon reconstructions were done in collaboration with Jan Odenthal.

The postsynaptic targets were categorized into one of the following: layer 2 or deep layer apical dendrite (shaft and dendritic spine of AD trunk and primary branches), shaft, single- or double-innervated spine (including neck targeting) of other dendrites, layer 2 cell body, axon initial segment (AIS) or glia. Next, we measured the fractional innervation of an axon by dividing the vector of synapse numbers for each group by the total (minus the seed synapse). The seed synapse biases our estimation of the seed AD fractional innervation, especially with axonal segments with low synapse numbers. The innervation fractions were averaged over axons seeded from each AD type (Figure 17c, e). Each dataset average (S1, V2, PPC and ACC cortices) was also computed separately (Figure 20).

#### **7.2.13. Dirichlet-multinomial model for postsynaptic targeting probability**

Dirichlet-multinomial models allow for defining distributions over the multinomial probability parameter vector. Therefore, we modeled the generative process for the axonal postsynaptic target counts using this distribution. With Dirichlet-multinomial models, a multinomial probability vector is drawn from a Dirichlet distribution for each sample (AD-targeting axon). Next, the synapse targeting count is generated as a multinomial sample of this probability vector. Next, we used a Newton-iteration implementation (Minka 2000) to find the maximum-likelihood estimate (MLE) of the Dirichlet-multinomial distribution for axonal targeting count. The mean of the MLE Dirichlet distribution was reported as the axonal innervation probability for layer 2 and deep ADs. In addition, we reported the fraction (in percent) of AD targeting probability (Figure 17b).

#### **7.2.14. Multiple innervation of an AD by inhibitory axons**

We next annotated cases where an AD was innervated multiple times by an AD-targeting inhibitory axon (Figure 19a), and then measured the average number of synapses onto L2 and deep layer targets by each axon (Figure 19b). Axons with no synapses (excluding the seed synapses) on L2 ( $n = 18$ , 46 for L2 and deep AD-seeded axons, respectively) or deep ADs ( $n = 48$ , 24 for L2 and deep AD-seeded axons,

respectively) were excluded since averages are not defined on empty sets. In addition, we plotted the histogram for the number of synapses on AD targets, as separated by the AD seed-type of axons (Figure 19d), and the number of times the seed structure is targeted (Figure 19e). To quantify the effect of multiple targeting on fractional AD innervation, we reported the average fraction of synapses (Figure 19c, upper panel,  $n=183$  axons) and individual AD targets ignoring multiple innervation of the same target (Figure 19c, lower panel,  $n=159$  axons).

#### **7.2.15. Distribution of pre- and post-synaptic neurites along cortical depth**

The depth of the main bifurcation relative to pia was determined by transforming the S1, V2, PPC and ACC datasets into a common coordinate system ( $n = 82$ , as seen in Figure 12). Next, we created a histogram (bin size of  $20\ \mu\text{m}$ ) and probability density estimate (bandwidth:  $25\ \mu\text{m}$ ) for main bifurcation densities along the cortical depth (Figure 18b). Note that this is only a subset of main bifurcations within each image volume.

We used the same datasets to estimate the density of AD-targeting inhibitory axons. The axonal annotations contained additional nodes used for marking synapses, which were removed before measuring the path length. We then computed the average fraction of the axonal path within  $20\ \mu\text{m}$  tangential cortical slices for each datasets (Figure 18c, error bars indicate mean  $\pm$  SEM over datasets,  $n = 4$ ).

#### **7.2.16. Visualization of neurites and their synapses**

The surface of the main bifurcation of PPC and S1 apical dendrite shafts and axons was extracted by segmenting the image volumes using SegEM (Berning, Boergens et al. 2015) and collecting all the segments of the neurites. The segment was then imported to MATLAB, binarized and smoothed using a  $9 \times 9 \times 9$  voxel<sup>3</sup> Gaussian convolution kernel with a standard deviation of 8 voxels. The surface mesh was then constructed at a threshold of 0.2 (Figure 5b, 17d).

For the V2 and ACC datasets, the volume of the main bifurcation of AD shafts was generated by tracing the dendrite outlines using the volume-tracing mode in webKnossos; the 3D data were processed in a similar fashion (Figure 5b).

Skeleton reconstructions of axonal (Figure 15a) and dendritic paths (Figure 5a-b, 7, 8d, 9a, 10a, 12) were represented by cylindrical tubes. Additional spheres were added to represent input (Figure 5b, 10a, 12) and output (Figure 15a, 17d) synapses.

The EM ultra-structure of an AD, synapses and cell bodies was demonstrated by electron micrographs of their cross-sections in the PPC dataset (Figure 5b, 14a,c-d, 15a, 16a). Overview EM images and low-res EM data were used to demonstrate the location and size of datasets (Figure 4a-b, 6a). The visualizations were generated using MATLAB (MathWorks, USA) and Amira (Thermo Fisher Scientific, USA).

### **7.2.17. Statistics**

The significance of difference between L2 and deep layer AD excitatory and inhibitory synapse densities (Figure 5c-d), inhibitory fractions (Figure 5e-f), synapse size (Figure 14b), double innervation of spines (Figure 14c), AD innervation fraction (Figure 17c), and L5 subtype comparisons (Figure 8c) were tested using the non-parametric Wilcoxon rank-sum test. In addition, the rank-sum test was used to test for the fraction of inhibitory and excitatory/inhibitory synapse densities between the main bifurcation and the distal tuft area for each pyramidal cell type (Figure 10d).

Difference in the inhibitory fraction between L2 (with L2MN), 3, 5tt and 5st apical dendrites at the main bifurcation and on the distal tufts was tested using the non-parametric Kruskal-Wallis test to account for the small sample size ( $n = 12, 10, 7, 11$  main bifurcations and  $n = 9, 7, 9, 6$  distal tuft branches for L2, 3, 5tt, 5st, respectively, Figure 9b, 10b). It was followed by Tukey's post-hoc range test to find significantly different pairs.

To identify differences in the axonal innervation fractions, a bootstrap test was designed. The identity of axonal groups was randomly shuffled and 10,000 bootstrap resamples (with replacement) were drawn matching the number of axons in the sample. The mean difference in each bootstrap resample between L2 and deep layer groups was compared to the sample's mean difference. The  $p$  value was calculated as the fraction of bootstrap resamples that had a value more extreme. The significance threshold was set to 0.05 with Bonferroni correction for 8 comparisons (Figure 17e).

To compare innervation fractions of AD-targeting axons across cortical regions, a multivariate analysis of variance (MANOVA) test was applied to 6 postsynaptic innervation fractions (AD, soma, spine and shaft of other dendrites). Axon initial segment (AIS) and glia groups were excluded since they had very few synapses that resulted in singular matrices when the MANOVA test was applied (0.8%, 0.04% of total synapses, respectively). The null hypothesis states that the cortical region does not affect the mean fractional innervations. We followed the MANOVA test when the null hypothesis was rejected (Figure 20c, L2 AD seeded axons) with multiple comparisons using Bonferroni-corrected one-way ANOVA tests to determine the target innervation(s) which vary across the cortex.

To investigate the possible exponential relationship between synaptic composition at the main bifurcation and its distance to the soma, single-term exponential models (with offset) of the form  $inh.fraction = c + a * e^{b*distance}$  were fit to the data from layers 2-5. The coefficient of determination ( $R^2$ ) was used as the goodness-of-fit measure. We also used  $R^2$  to compare models explaining the relationship between morphology and synapse density of L5 pyramidal neurons (Figure 8). To understand the relationship between morphology and synapse density of L5 neurons, we fitted a linear model to individual synapse densities and a non-linear model (form:  $\frac{ax+b}{cx+a}$ ) to their inhibitory fraction.

#### 7.2.18. Data and software availability

All analysis software for the cell-type specific apical tuft dendrite innervation analysis is available under the MIT license using the following link:

<https://gitlab.mpcdf.mpg.de/connectomics/apicaltuftpaper>

All 6 datasets are available for browsing at [demo.webknossos.org](http://demo.webknossos.org) using the following links:

S1: [Hyperlink](#)

V2: [Hyperlink](#)

PPC: [Hyperlink](#)

ACC: [Hyperlink](#)

LPtA: [Hyperlink](#)

PPC-2: [Hyperlink](#)

### **7.3. Correlative volumetric light and electron microscopy**

#### **7.3.1. Viral injection into M2 and V1 cortices**

Our injection approach closely followed FluoEM (Figure 23a, (Drawitsch, Karimi et al. 2018)). We anesthetized a wild-type C57BL/6J mouse (age: 35 postnatal days, weight: 17.8 g) by inhalation of 2-4% isoflurane in Carbogen (CO<sub>2</sub> in medical oxygen). The body temperature was maintained at 37 °C using a heating pad (feedback-controlled, DC Temperature Control System, FHC, USA) and fixed in a stereotaxic frame (Kopf Instruments, USA). Systemic analgesia, a combination of 2 and 100 mg/kg Meloxicam (Metacam, Boeringer-Ingelheim, Germany) and Metamizol (Metamizol WDT, WDT, Germany), was injected subcutaneously 1 hour prior to operation in addition to local anesthesia during surgery (16.7 mg/kg Ropivacaine (Naropin, AstraZeneca, Switzerland) injected under the scalp). To label projection axons anterogradely in M2 (1 mm lateral, 1.4 mm anterior relative to bregma, right hemisphere) and V1 (2.5 mm lateral, 4.2 mm posterior to bregma, right hemisphere), we injected adeno-associated viruses (AAV) expressing eGFP (AAV1. CAG. Flex. eGFP. WPRE. bGH (Allen Institute 854),  $1.71 \times 10^{13}$  genome count (GC)/ml, Penn Vector Core, USA) and tdTomato (AAV1. CAG. Flex. tdTomato. WPRE. bGH (Allen Institute 864),  $1.07 \times 10^{13}$  GC/ml, Penn Vector Core, USA). The fluorescent AAV was mixed in a 2:1 ratio with AAV.Cre solution (AAV1.CamKII0.4.Cre.SV40,  $2.3 \times 10^{13}$  GC/ml, Penn Vector Core, USA). The injection (~50 nl) was performed 500 µm below cortical surface using a pressure injection system (PDES, NPI, Germany).

We performed the transcardial perfusion 3 weeks after the injections to allow for expression of fluorescent proteins in projection neurons of V1 and M2 (postnatal day 57). The perfusion was performed as described above with the addition of DiD (1,1'-Diocetadecyl-3,3,3',3'-Tetramethylindodicarbocyanine) to the initial buffer for labelling blood vessels (5 µM, Thermo Fisher, USA)

### **7.3.2. Sample preparation and confocal laser scanning light microscopy (LM)**

In FluoEM, it was crucial that sample preparation would allow for imaging of the same volume in both LM and EM. We sliced the brain along the coronal plane to generate a 600  $\mu\text{m}$  thick slice containing PPC (2 mm posterior and 1.7 lateral to bregma). Next, we separated the PPC cuboid from the rest of the section using a surgical razor. One of the edges of the cuboid was intentionally oblique to allow for determining the side of block being imaged (LSM 880, Zeiss, Germany).

The PPC sample was transferred to a buffer-filled imaging chamber (Grace Bio-Labs, USA) used for inverted confocal laser-scanning microscopy (LSM 880, Zeiss, Germany). We imaged three channels (eGFP and tdTomato labelled axons and DiD labelled blood vessels) of  $1130 \times 909 \times 94 \mu\text{m}^3$  (voxel size:  $115 \times 115 \times 444 \text{ nm}^3$ , Figure 23), using a 40X water objective (C-Apochromat 40x/1.2 W Korr FCS M27, Zeiss, Germany). The sample preparation for electron microscopy and 3D-EM imaging was detailed in the section above (PPC-2 sample, Figure 23b).

### **7.3.3. Alignment of long-range axons between 3D-LM and EM**

We followed the previously reported matching process for fluorescently labelled axons in 3D-LM to their counterparts in the 3D-EM dataset (Drawitsch, Karimi et al. 2018). In short, blood vessel bifurcations were used to constrain an initial, coarse affine alignment between LM and EM datasets ( $2.7 \pm 0.9 \mu\text{m}$  residual Euclidian distance error, mean  $\pm$  SD,  $n = 23$  control points). Next, we iteratively matched LM axons to their EM counterparts and used their boutons as control points to refine the transformation (Figure 23c-d,  $1.5 \pm 0.8 \mu\text{m}$  vs.  $86 \pm 100 \text{ nm}$  for final affine and freeform transformations, respectively, mean  $\pm$  SD,  $n = 348$  control points)

### **7.3.4. Extracting distribution of postsynaptic targets**

The source of 24 long-range axons from M2 ( $n = 12$ ) and V1 ( $n = 12$ ) was determined by the matching to their LM counterparts. We first measured the density of synapses normalized to the path length of the axons (Figure 23e). Next, we annotated all the postsynaptic targets of the long-range axons ( $n = 1619$  synapses) and asked student annotators to reconstruct the dendrite. Students were instructed to note the soma location within the dataset boundaries (annotation redundancy = 3). About half

of the postsynaptic targets' soma (804/1619) was identified within the volume (Figure 24d-e, 25).

We noted the locations of pia and layer 1 by fitting a surface through a set of coordinates extracted from the surface annotations in LM and EM data, respectively. In addition, we used the cyto-architecture of L2-5 to find an approximate depth map for cortical layer borders (145, 245, 410, 460  $\mu\text{m}$  from pial surface for L1/2, L2/3, L3/4 and L4/5 borders, respectively).

## 8. Results

### 8.1. Synaptic composition in apical dendrites of pyramidal neurons

In the following section, we describe the composition of excitatory and inhibitory synapses on the apical dendrite surface of pyramidal neurons at the superficial cortical layers.

#### 8.1.1. Synaptic composition at the main bifurcation of layer 2 (L2) and deep layer (L3/5) pyramidal neurons

We used serial block-face scanning electron microscopy (SBEM, (Denk and Horstmann 2004)) to acquire electron microscopy image volumes from the layer 1/2 border region (L1/2) of primary somatosensory (S1), secondary visual (V2), posterior parietal (PPC) and anterior cingulate (ACC) cortices in mouse (Figure 4). The regions represent a mixture of primary sensory and higher-order cortices (Figure 4c-d) (Woolsey and Van der Loos 1970, Kolb and Walkey 1987). The datasets were acquired at a nominal resolution of  $11.24\text{-}12 \times 11.24\text{-}12 \times 28\text{-}30 \text{ nm}^3$  and were approximately the size of a cube with an edge length of  $100 \text{ }\mu\text{m}$  (Figure 4b,  $9.4\text{-}1.2 \times 10^6 \text{ }\mu\text{m}^3$ ).

Apical dendrites (ADs) from most layer 2-5 (L2-5) pyramidal neurons bifurcate in the L1/2 border region and branch further in L1 to generate the apical tuft dendrite (Figure 4a, 5a, (Larkman and Mason 1990)). Our goal was to measure and compare the inhibitory input size at the main bifurcation of ADs (Larkum, Zhu et al. 1999, Ledergerber and Larkum 2012). While ADs originating from cell bodies within the EM volume were classified as layer 2 (L2), deep layer (L3/5) ADs were from cell bodies residing deeper within the cortex (i.e. layers 3 and 5) (Figure 4a, 5, grey and orange reconstructions represent L2 and L3/5, respectively). Note that layer 4 is either not prominent (association cortical areas, (Kolb and Walkey 1987)) or most L4 neurons do not possess an apical dendrite (spiny stellate neurons in S1, (Feldmeyer, Egger et al. 1999)).



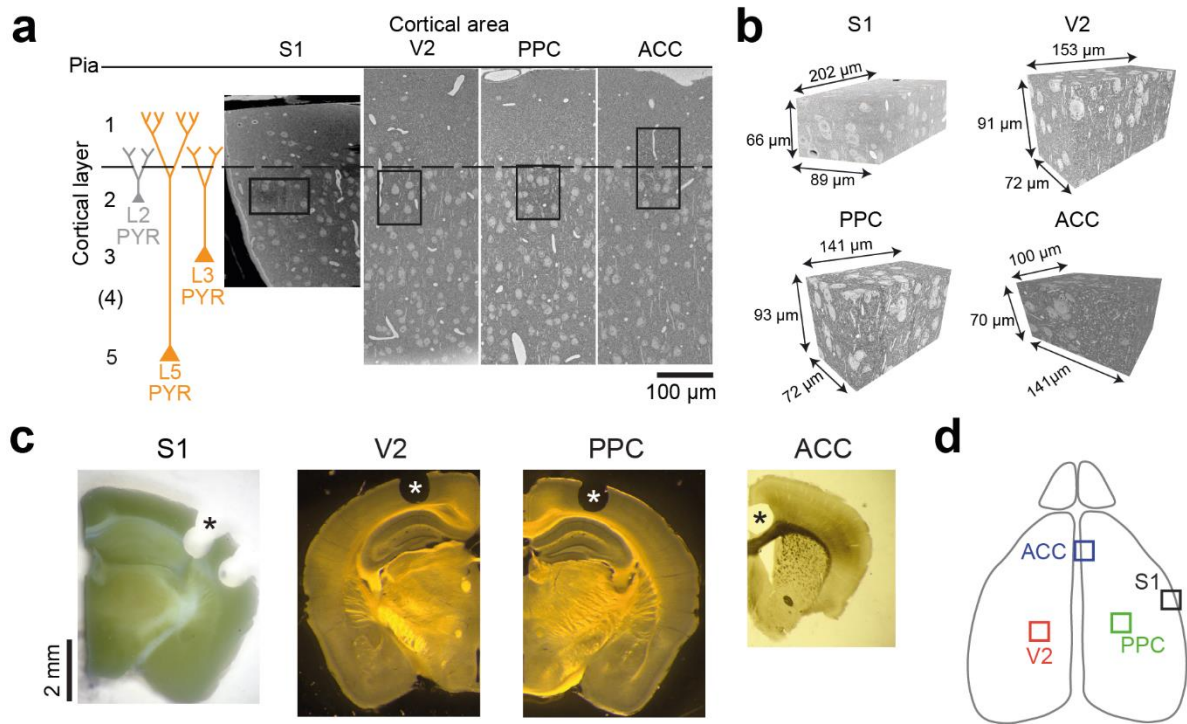


**Figure 4. 3D electron microscopy datasets of size  $\sim 10^6 \mu\text{m}^3$  used for analysis**

**(a)** EM overview of datasets from primary somatosensory (S1), secondary visual (V2), posterior parietal (PPC) and anterior cingulate (ACC) cortices. **(b)** Volume representation of the datasets with their respective dimensions. Note that datasets were about  $10^6 \mu\text{m}^3$ . **(c)** Coronal sections of the mouse brain section (100-1000 μm in thickness) from which S1, V2, PPC and ACC datasets were extracted. Stars indicate the sample location. **(d)** The horizontal illustration of the mouse cortex with the approximate location of each dataset. ACC and S1 datasets were acquired by Jan Odenthal and Kevin Boergens, respectively. This figure is reproduced with modifications from (Karimi, Odenthal et al. 2019) and is licensed under the CC-BY-NC-ND 4.0.

Next, we annotated all chemical input synapses about 10 μm around the main bifurcation of L2 ( $n = 41$ ) and L3/5 ( $n = 41$ ) ADs (Figure 5b,  $n = 5148$ , 1092 for excitatory and inhibitory synapses, respectively. Total dendritic length analyzed: 3.33 mm). The inhibitory synapse density normalized to dendritic shaft path length was larger for L2 as compared to L3/5 pyramidal neurons (Figure 5c,  $0.42 \pm 0.02$  vs.  $0.22 \pm 0.02$  synapses per μm for L2 and L3/5, respectively, mean  $\pm$  SEM,  $n = 82$ , Wilcoxon rank-sum test,  $p$

$< 10^{-7}$ ). Combined with the higher excitatory input density in L3/5 pyramidal neurons (Figure 5c,  $1.09 \pm 0.1$  vs.  $2.12 \pm 0.15$  synapses per  $\mu\text{m}$  for L2 and L3/5, respectively, mean  $\pm$  SEM,  $n = 82$ , Wilcoxon rank-sum test,  $p < 10^{-6}$ ), the inhibitory fraction was about 3 fold higher for the main bifurcation of L2 neurons (Figure 5e,  $33.6 \pm 17.9\%$  vs  $9.9 \pm 5.1\%$  of synapses for L2 and L3/5, respectively, mean  $\pm$  SD, Wilcoxon rank-sum test,  $p < 10^{-11}$ ). The increase in inhibitory input density and fraction for L2 neurons was consistently present across the cortical regions investigated (S1, V2, PPC and ACC, (Figure 5d, f)).

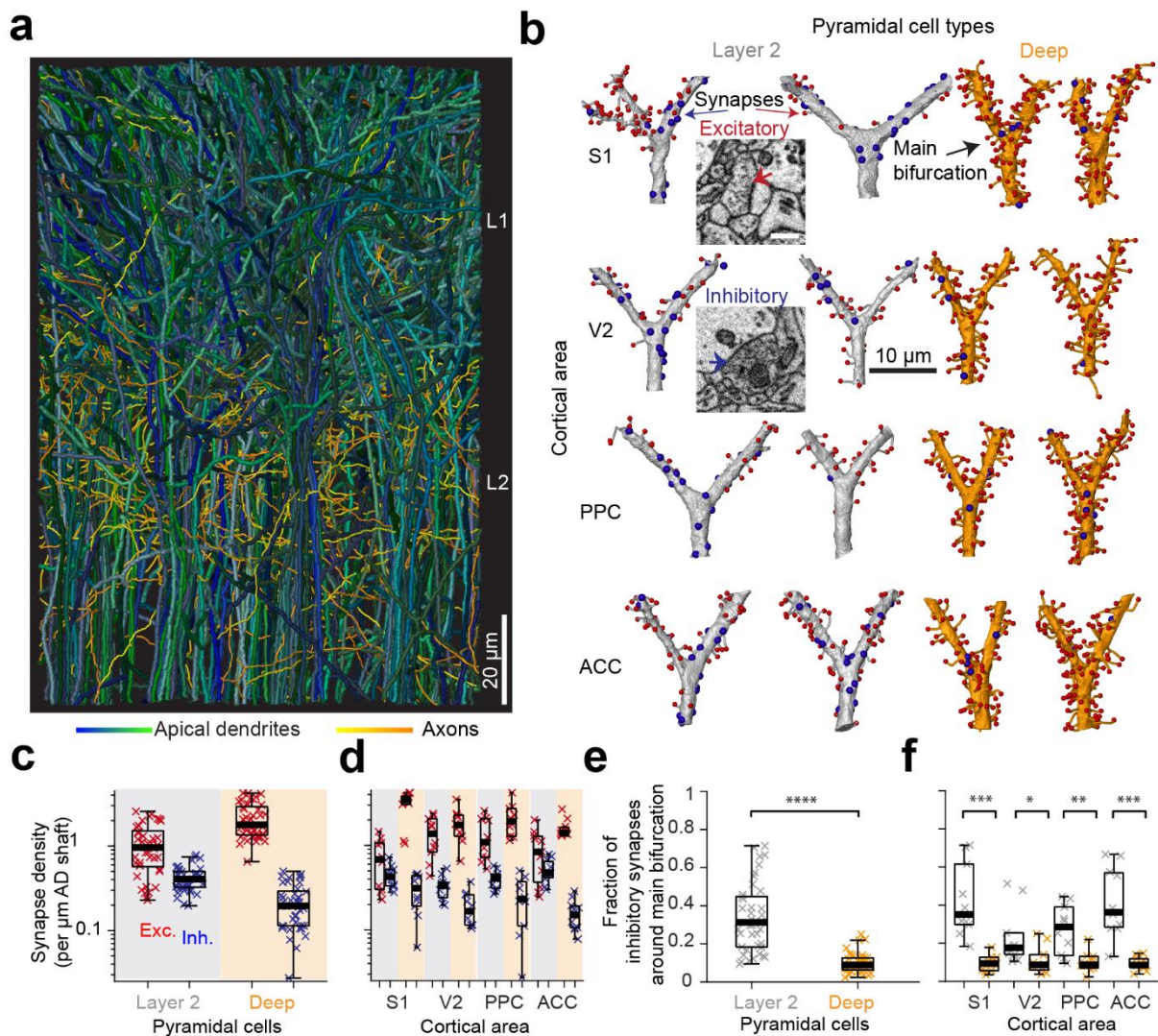
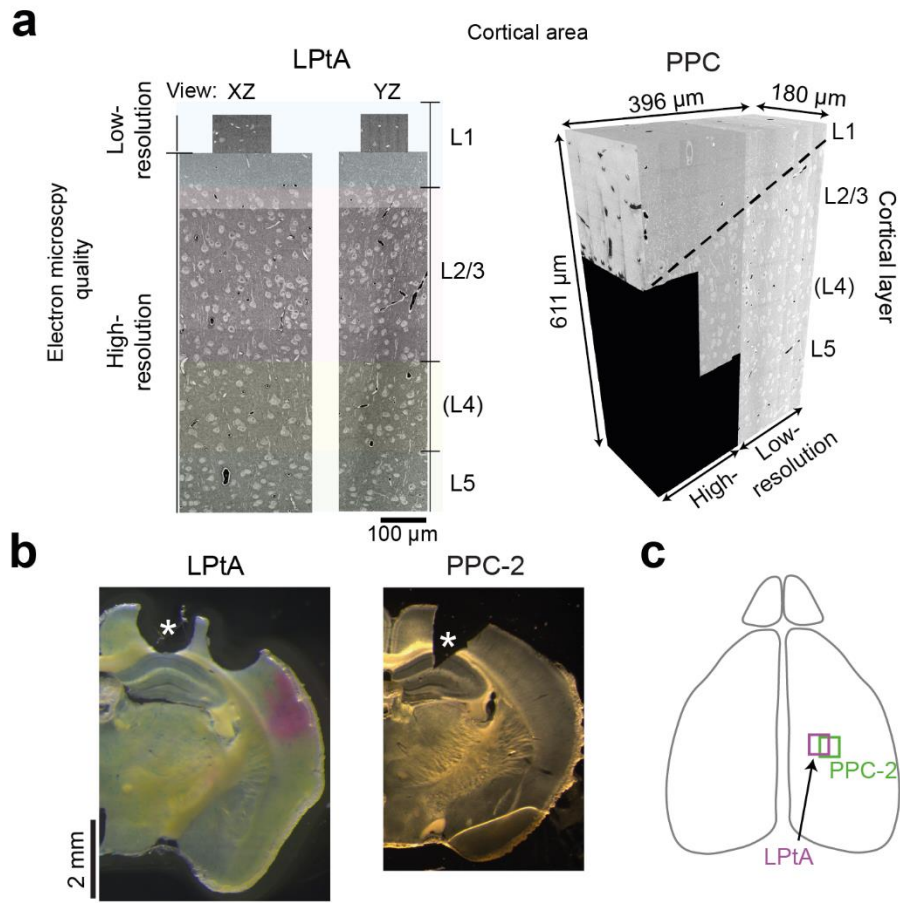


**Figure 5. Complete synaptic input mapping of the main bifurcation of apical dendrites in pyramidal neurons**

**(a)** Skeleton representation of all ADs contained in the ACC dataset volume (blue-green,  $n = 61$  layer 2 and  $n = 152$  deep layer ADs, respectively) and a subset of inhibitory axons innervating them ( $n = 62$ , yellow-orange). Note that most pyramidal neuron types stretch their apical dendrite to the L1/2 border region. **(b)** Excitatory (red spheres) and inhibitory (blue spheres) synaptic input maps of apical dendrite main bifurcations for deep layer (orange) and layer 2 (grey) pyramidal cells (example synapses, inset). **(c)** Boxplot of inhibitory (blue crosses) and excitatory (red crosses) synapse densities normalized to AD shaft path length ( $\mu\text{m}$ ) for L2 ( $n = 41$ , left) and deep layer ADs ( $n = 41$ , right) in S1, V2, PPC and ACC datasets. Wilcoxon rank-sum test,  $p < 10^{-6}$  for both synapse types. **(e)** Boxplot of the fraction of inhibitory synapses at the main bifurcation of deep (orange) and layer 2 (grey) ADs; individual ADs shown (crosses). **(d,f)** Same as in **(c,e)** separately reported by cortical region ( $n = 20$  for S1, V2 and PPC,  $n = 22$  for ACC). Asterisks indicate significance level of the Wilcoxon rank-sum test (\* $p < 0.05$ , \*\* $p < 0.01$ , \*\*\* $p < 10^{-3}$ , \*\*\*\* $p < 10^{-4}$ ). Scale bars:  $0.5 \mu\text{m}$  (inset in c). This figure is reproduced with modifications from (Karimi, Odenthal et al. 2019) and is licensed under the CC-BY-NC-ND 4.0.

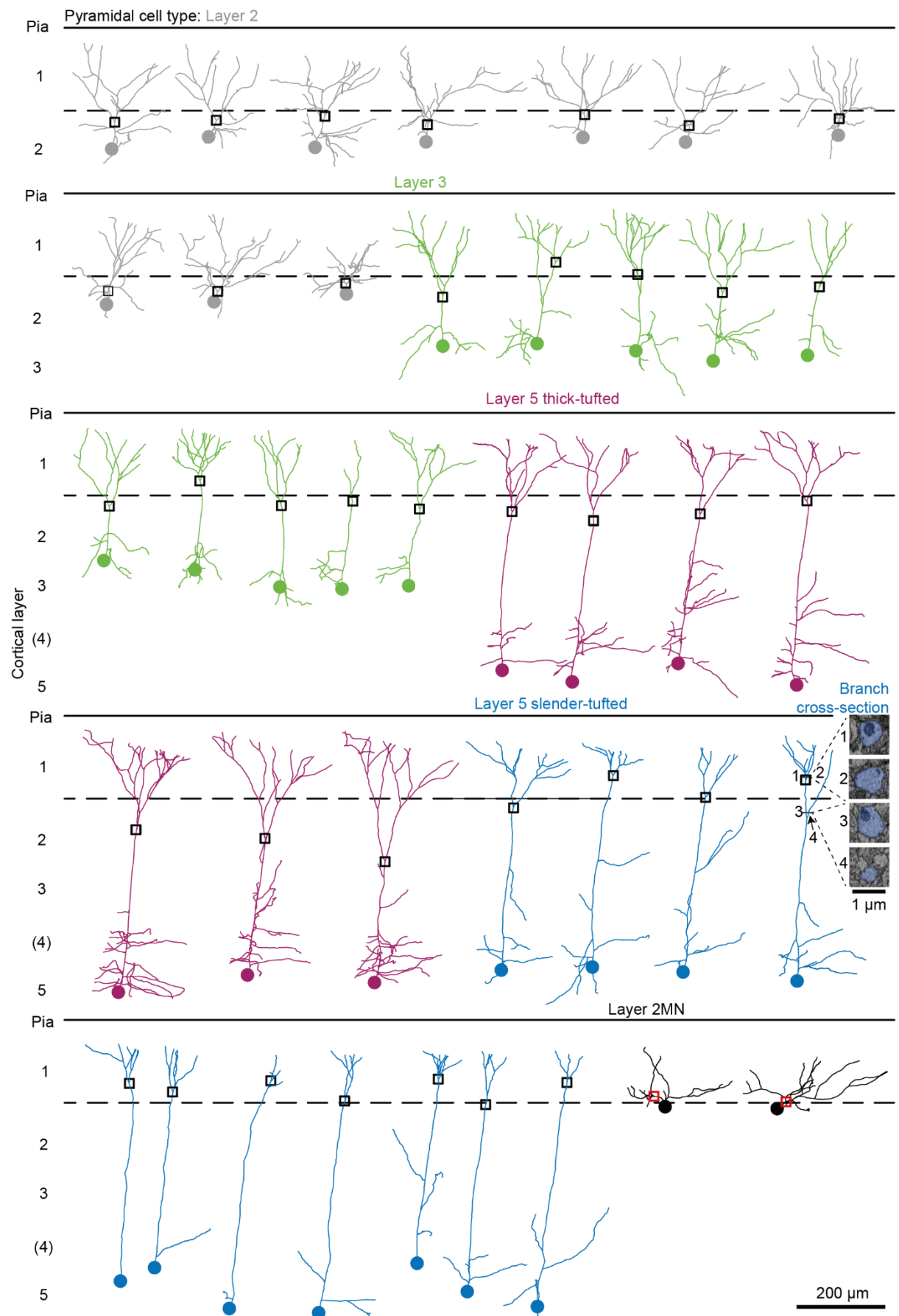
### 8.1.2. More detailed definition of cell types in datasets containing layers 1-5

We aimed to distinguish layer 3 and 5 apical dendrites by imaging a larger volume of the neocortex. Large volumes, imaged at the same resolution, require longer imaging times and increase the probability of failure. We, therefore, imaged layers 1-5 in PPC and LPtA cortices (Figure 6b, c, PPC-2 and LPtA datasets) by a combination of high- (voxel size:  $11.24 \times 11.24 \times 30 \text{ nm}^3$  for both datasets) and low-resolution 3D-EM (Figure 6a, voxel size:  $22.48 \times 22.48 \times 30 \text{ nm}^3$ ,  $44.96 \times 44.96 \times 120 \text{ nm}^3$  for PPC-2 and LPtA). The high-resolution EM volume was targeted to layers 1 and 2, where the distal apical dendrite tuft and main bifurcation of most L2-5 neurons reside (Figure 6a, LPtA and PPC-2 contain L1 and L1/2, respectively). The low-resolution EM volume covered the cortical depth to the middle of layer 5.



**Figure 6. Datasets used for detailed cell-type specific analysis**

**(a)** Two orthogonal cross-sections of the dataset from LPTA cortex (left) and volume representation of the dataset from PPC cortex (PPC-2). Note that the LPTA and PPC-2 datasets have high-resolution EM in layers 1 and 1 / 2, respectively. **(b)** Coronal sections from which LPTA and PPC-2 datasets were extracted. **(c)** Schematics demonstrating the approximate location of each dataset on the surface of mouse cortex. The LPTA dataset (a) was acquired and provided by Florian Drawitsch. The panel (b) is reproduced with modifications from (Karimi, Odenthal et al. 2019) and is licensed under the CC-BY-NC-ND 4.0.

**a**



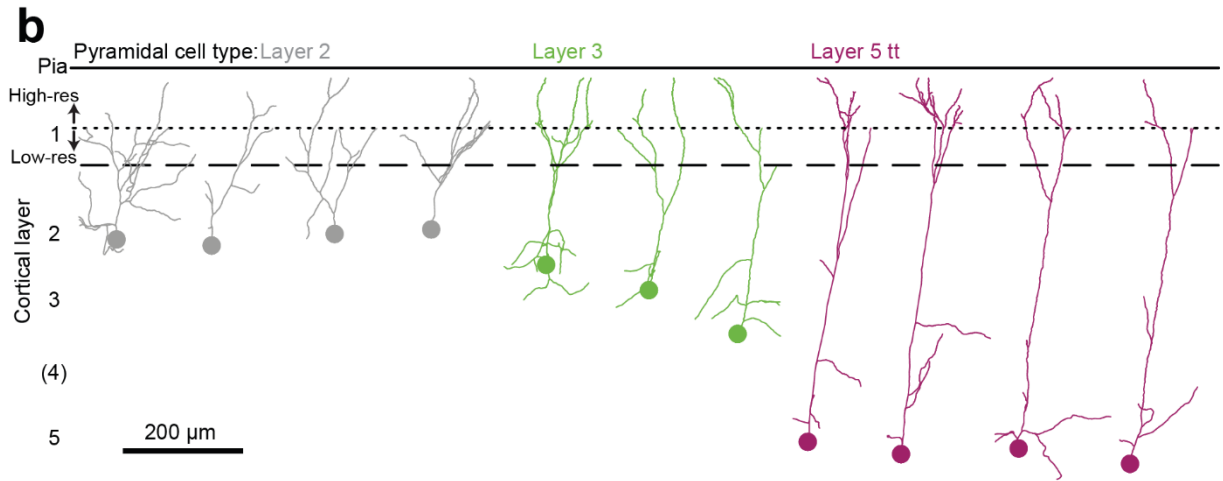


**Figure 7. Reconstruction of apical dendrites of pyramidal neurons used in cell-type specific analysis**

**(a)** Skeleton reconstruction of apical dendrites of layer 2 (grey traces,  $n = 10$ ), 2MN (black,  $n = 2$ ), 3 (green,  $n = 10$ ), 5tt (magenta,  $n = 7$ ), 5st (blue,  $n = 11$ ) pyramidal cells in PPC-2 dataset (PPC cortex). Black / red rectangles indicate the main bifurcation area used for synaptic input mapping in each annotation. The same L5st (blue) neurons are used for distal AD synaptic input mapping. Also see Figure 9a. **(b)** Same as in (a) for neurons used for distal apical dendrite tuft synaptic input mapping in the LPtA cortex. The border between the high- and low-resolution EM datasets is indicated by a dotted line. See Also Figure 10. The dashed and solid lines indicate pia and the layer 1/2 border, respectively. The cell body location of each neuron is indicated by a circle.

Next, we reconstructed the apical dendrite's trunk within the EM volumes followed by dense synaptic input mapping at the main bifurcation (Figure 7a, PPC-2 dataset) or distal apical dendrite tuft (Figure 7b, LPtA and PPC-2 datasets). Each neuron's layer of origin was defined by its soma depth relative to pial surface (Table 5, also see methods). Layer 2 marginal neurons (L2MN) and slender-tufted layer 5 (L5st) pyramidal neurons were distinguished from other L2 and 5 neurons using additional morphological features described in the following section.

### 8.1.3. Layer 2 marginal neurons (L2MN) and slender-tufted layer 5 (L5st) neurons

A subset of layer 2 neurons with cell bodies on the L1/2 border, possess a less prominent (obliquely directed) apical dendrite and are sometimes called marginal neurons (L2MN, (Larkman and Mason 1990, Luo, Hasegawa et al. 2017)). We identified two L2MN neurons and measured their inhibitory fraction to compare to other L2 neurons (Figure 7, 9, black annotations with red boxes marking their main bifurcation).

Slender-tufted layer 5 pyramidal neurons (L5st) are known to be morphologically (Larkman and Mason 1990) and functionally (Rojas-Piloni, Guest et al. 2017) different from other thick-tufted L5 neurons. We distinguished slender- and thick-tufted L5 neurons by hierarchical clustering using four morphological features (Figure 8b, upper panel). Consistent with previous reports, L5st neurons had thinner dendrites, smaller soma and AD trunk diameter and superficial main bifurcations as compared to L5tt neurons (Figure 8a). We also found lower spine density in L1/2 region for L5st neurons when compared to their L5tt counterparts (Figure 8c,  $1.4 \pm 0.23$  vs.  $0.59 \pm 0.13$  spines per  $\mu\text{m}$  path length for L5tt ( $n = 16$ ) and L5st ( $n = 17$ ), respectively, mean  $\pm$  SEM, Wilcoxon rank sum test,  $p = 0.004$ ).

Next, we investigated the relationship between morphological features of L5 neurons and the density of synapses around the main bifurcation. Interestingly, the first principal component (PC 1) of the four dimensional morphological feature space correlated with the level of thick-tuftedness in L5 neurons (Figure 8d). We found a strong linear relationship between excitatory synapse density of L5 neurons and their thick-tuftedness (Linear model,  $R^2 = 0.75$ ,  $p < 10^{-5}$ ). This resulted in a non-linear anti-correlation between fraction of inhibitory synapses and the thick-tuftedness of L5 neurons (Figure 8e, solid black line, fraction of two linear expression model,  $R^2 = 0.74$ ,  $p < 10^{-7}$ ). Using only the linear excitatory synapse density and the average inhibitory synapse density, we were able to explain most of the variance in the inhibitory fraction (Figure 8e, dashed red line,  $R^2 = 0.61$ , compare to only inhibitory (dashed blue line,  $R^2 = -0.57$ ) and combined models (dashed black line,  $R^2 = 0.39$ )).

Layer 5 pyramidal neurons were previously classified into L5A (superficial) and L5B (deep), based upon the cortical depth of their soma (Ahissar, Sosnik et al. 2001, Manns, Sakmann et al. 2004). We were, however, unable to find the same separation between the cell bodies of L5tt and L5st neurons (Figure 8f,  $556 \pm 20$  vs.  $557 \pm 39$   $\mu\text{m}$  relative to pia for L5tt and L5st, respectively, mean  $\pm$  SEM,  $n=18$ ).

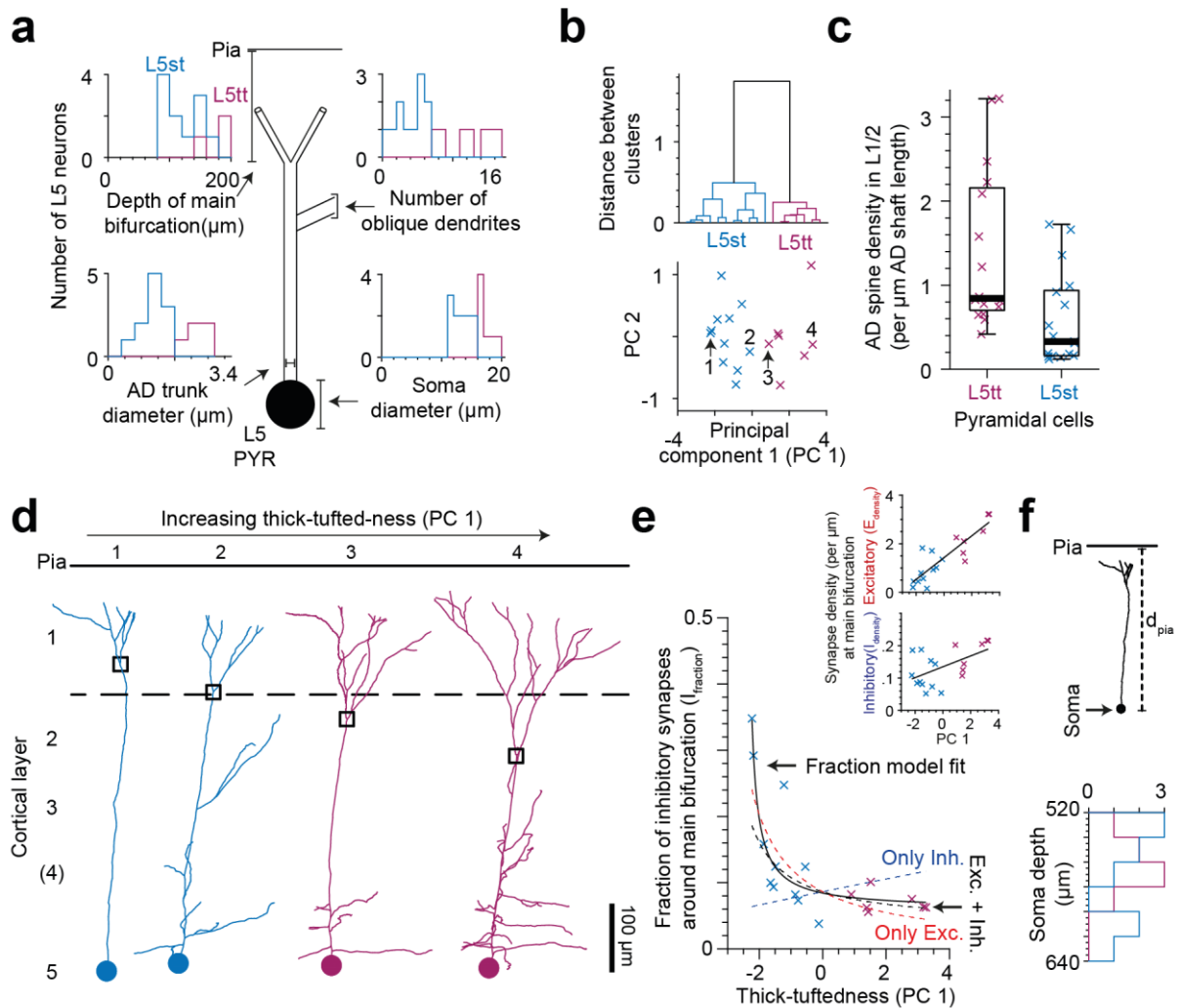


**Figure 8. Classification of L5 neurons into slender-tufted and thick-tufted subtypes.**

**(a)** Sketch illustrating four morphological features of L5 neurons used for their hierarchical classification. Insets show histograms of each feature for the L5tt (magenta,  $n = 7$ ) and L5st (blue,  $n = 11$ ) neurons. **(b)** Agglomerative hierarchical linkage tree (upper panel) and scatter plot of the first two principal components



(lower panel) for neurons in (a). Numbers in lower panel indicate the L5 neurons plotted in (d). **(c)** Boxplot of spine density for L5tt (magenta) and L5st (blue) neurons around their main bifurcation and at their distal apical dendrite tuft in L1/2. **(d)** Reconstruction of the apical dendrite of neurons indicated in (b). Note the correlation between first principle component and the thick-tuftedness of L5 neurons. **(e)** Relationship between thick-tuftedness (PC 1) of L5 neurons ( $n = 18$ ) and the inhibitory fraction at their main AD bifurcation. The solid black lines indicate a linear ( $E_{density} = 0.45 \times PC1 + 1.4$ ,  $R^2 = 0.75$ ,  $p < 10^{-5}$ ,  $I_{density} = 0.016 \times PC1 + 0.13$ ,  $R^2 = 0.26$ ,  $p = 0.017$ ) or a non-linear ( $I_{fraction} = \frac{0.035 \times PC1 + 0.12}{0.58 \times PC1 + 1.42}$ ,  $R^2 = 0.74$ ,  $p < 10^{-7}$ ) model fit. Dashed lines indicate relationships between PC1 and inhibitory fraction using only linear model fits to excitatory (red), inhibitory (blue) or both (black) synapse densities. Insets are the scatter plot of excitatory and inhibitory synapse density relative to the thick-tuftedness of L5 neurons. **(f)** Sketch illustrating the soma depth measure (upper). Histogram of soma depth for L5tt and L5st neurons (lower).

#### 8.1.4. Synaptic composition at the main bifurcation of L2-5 pyramidal neurons

We reconstructed the ADs of a random subset of L2, 2MN, 3, 5tt and 5st pyramidal cell bodies to find their main bifurcation in high-resolution EM (Figure 9a). Next, we mapped all the input synapses around the main apical dendrite bifurcation of these neurons ( $n=40$ ). The L2 main bifurcations had an increased inhibitory synapse fraction as compared to L3 and thick-tufted L5 (L5tt) neurons (Figure 9b,  $0.38 \pm 0.048$ ,  $0.08 \pm 0.008$ ,  $0.09 \pm 0.01$  for L2/2MN, 3, 5tt, respectively, mean  $\pm$  SEM,  $n=40$ , Kruskal-Wallis test,  $p < 10^{-4}$ , Post-hoc Tukey's range test,  $p = 0.001$  and  $2.7 \times 10^{-5}$  for L2 vs. L3 and L5tt, respectively).

To understand the effect of each individual synapse type on the inhibitory fraction, we investigated synapse densities normalized to the dendritic path length of ADs (Figure 9c). Inhibitory synapse density was lower in the L3 and 5 groups as compared to L2 ( $0.63 \pm 0.04$ ,  $0.27 \pm 0.05$  and  $0.2 \pm 0.02$  inhibitory density per  $\mu m$  for layers 2/2MN, 3 and 5tt, respectively, mean  $\pm$  SEM, Kruskal-Wallis test,  $p < 10^{-5}$ , followed by Tukey's range test with  $\alpha = 0.05$ ). The excitatory synapse density was increased for L3 neurons as compared to L2/2MN neurons ( $1.29 \pm 0.21$ ,  $3.17 \pm 0.4$  and

1.88±0.22 for layers 2/2MN, 3 and 5tt, respectively, mean ± SEM, Kruskal-Wallis test,  $p < 10^{-4}$ , followed by Tukey's range test with  $\alpha = 0.05$ ). This demonstrates that deep (L3 and L5tt) pyramidal neurons have similar synapse compositions at their main bifurcations.

Preliminary analysis of L2MN neuron inhibitory fraction at the main bifurcation showed similarities to other L2 pyramidal neurons (Figure 9b, 53.2% and 27.7% inhibitory fraction for L2MN,  $n = 2$ ). We, therefore, combined L2 and L2MN neurons in our analysis above. L5st neurons had slightly increased inhibitory fraction at the main bifurcation as compared to L5tt neurons (Figure 9b, 0.15±0.03 and 0.09±0.01 inhibitory fraction for L5st ( $n = 7$ ) and L5tt ( $n = 7$ ), Wilcoxon rank-sum test,  $p = 0.1$ ). Note that the synapse densities of L5st neurons were corrected with the synaptic identification error estimates as described below (Figure 9b-c, 15, grey lines connect pre- and post-correction densities).

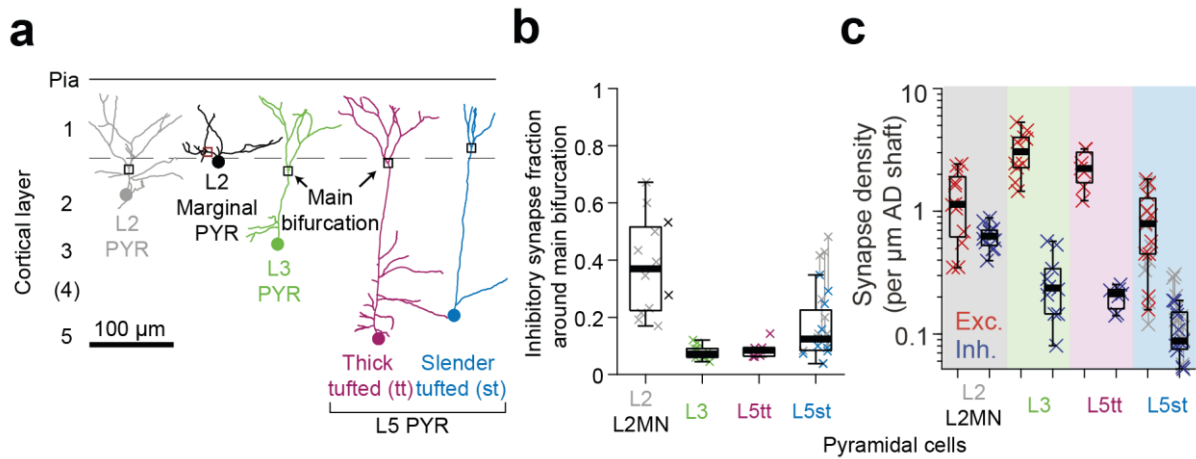


**Figure 9. Cell-type specific inhibitory size at the main bifurcation of apical dendrites**

**(a)** Skeleton reconstruction of apical dendrites contained within the high- and low-resolution volume of the PPC dataset. Main bifurcation (black/red rectangles) of ADs and their soma of origin (circles), marked for L2 (grey), L2MN (black), L3 (green), L5tt (magenta) and L5st (blue) neurons. **(b)** Boxplot of inhibitory synapse fraction around the main bifurcation of apical dendrites from layer 2 (grey,  $n = 10$ ), 2MN (black,  $n = 2$ , boxplot shared with L2 group), 3 (green,  $n = 10$ ), 5tt (magenta,  $n = 7$ ), and 5st (blue,  $n = 11$ ) pyramidal cells. Synaptic

input composition is distinct for each neuronal type at the main bifurcation. Kruskal-Wallis test,  $p < 10^{-4}$ . **(c)** Boxplot for density of excitatory (red) and inhibitory (blue) synapses around the same main bifurcations as in (b). Crosses indicate individual ADs. Panels (b-c) are reproduced with modifications from (Karimi, Odenthal et al. 2019) and licensed under the CC-BY-NC-ND 4.0.

### 8.1.5. Distal apical dendrites' synaptic composition in layer 1 for L2-5 pyramidal neurons

The composition of synapses in the distal segments of apical dendrites in L1 was also investigated since spine densities were reported to be ~5-fold lower as compared to the apical dendrite trunk for the hippocampal pyramidal neuron (Bannister and Larkman 1995, Megías, Emri et al. 2001). Therefore, we annotated synapses in 14 distal tuft dendrites (n=31 individual branches) of L2-5 pyramidal neurons in LPtA and PPC-2 datasets (Figure 10a).

Interestingly, we were unable to find a significant difference between the inhibitory synapse densities of L2 (n = 9 branches), L3 (n = 7), L5tt (n = 9) and L5st (n = 6) neurons in their distal AD tuft (Figure 10c,  $0.13 \pm 0.02 - 0.22 \pm 0.03$  inhibitory synapses per  $\mu\text{m}$  shaft path length,  $p = 0.08$ , Kruskal-Wallis test). However, the excitatory synapse densities were significantly higher for L2 and 3 cells, as compared to L5 pyramidal subtypes (Figure 10c,  $1.84 \pm 0.16$  and  $1.91 \pm 0.18$  vs.  $0.70 \pm 0.04$  and  $0.3 \pm 0.02$  excitatory synapses per  $\mu\text{m}$  shaft length for L2/3 vs. L5tt/st cells, respectively.  $p < 10^{-4}$ , Kruskal-Wallis test). Thus, the inhibitory fraction was higher for L5 pyramidal sub types as compared to L2 and 3 pyramidal neurons in this region (Figure 10b,  $11.3 \pm 1.3\%$  and  $10.2 \pm 0.9\%$  vs.  $22.5 \pm 1.7\%$  and  $31.3 \pm 1.7\%$  inhibitory fraction for L2/3 vs. L5tt/st cells, respectively.  $p < 10^{-4}$ , Kruskal-Wallis test).

Compared to the main bifurcation, L5 neurons exhibited about 2.5 fold drop in their excitatory synapse density. In combination with their relatively similar inhibitory synapse density, this meant that the inhibitory fraction was reduced by a factor of more than 2 fold for slender- and thick-tufted L5 neurons (Figure 10d, compare Figure 9c and Figure 10c). This pattern of synaptic composition follows the previous reports for hippocampal neurons (Bannister and Larkman 1995, Megías, Emri et al. 2001).

L2 pyramidal neurons reduced their inhibitory fraction about 3.4 fold in layer 1 compared to their main bifurcation by  $\sim 1.4$  fold reduction of inhibitory and  $\sim 2.8$  fold increase in excitatory synapse densities. This resulted in inhibitory hot-zones around the main bifurcation and in distal apical dendrite tuft for L2 and L5 pyramidal neurons, respectively (Figure 10d). L3 pyramidal neurons had a consistent inhibitory fraction ( $\sim 10\%$ ) along their apical dendrite. Therefore, each apical dendrite type had its unique pattern of inhibitory input fraction in the upper cortex allowing for different functional and computational properties (Figure 10d).

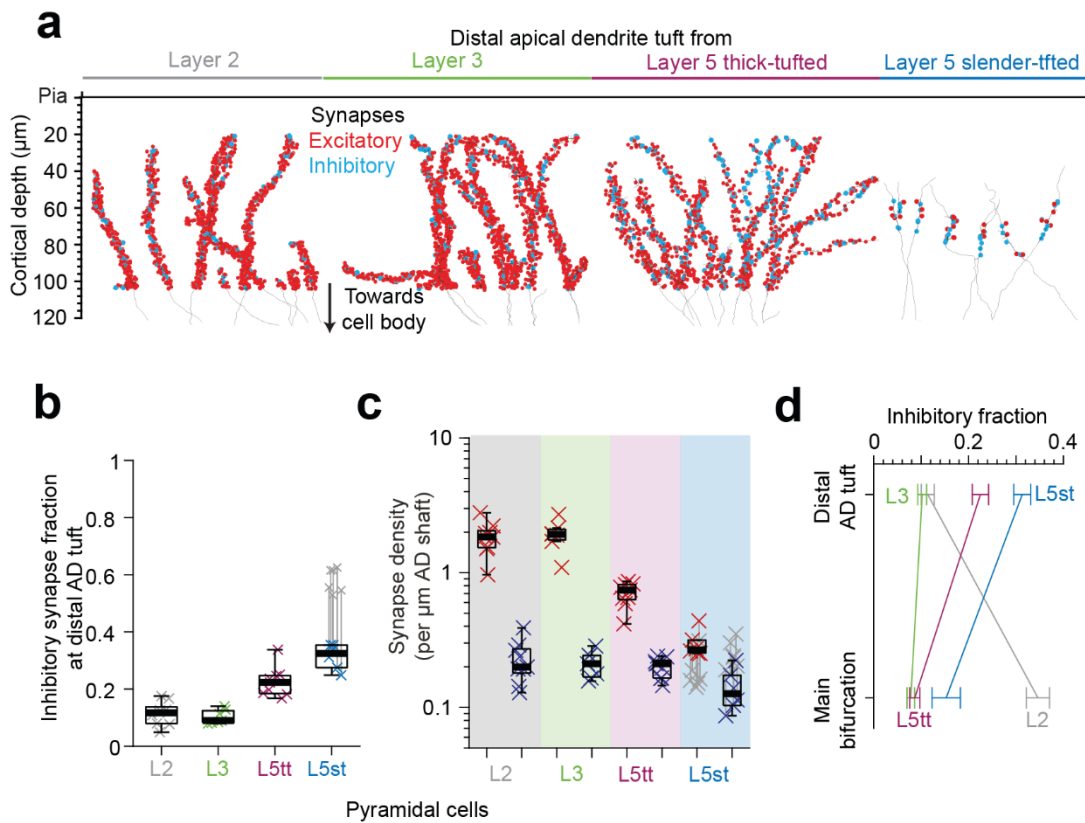


**Figure 10. Inhibitory fraction at the distal apical dendrite tuft of L2-5 pyramidal neurons**

**(a)** Excitatory (red,  $n = 3,812$ ) and inhibitory synapses (cyan,  $n = 694$ ) for 14 ADs within the high-resolution EM image volume in layer 1 of LPtA (L2, L3, L5tt) and PPC (L5st) cortex. Grey line indicates the skeleton representation of the AD shaft. **(b)** Boxplot for fraction of inhibitory synapses at the distal apical dendrite site (a) from layer 2 ( $n = 9$  individual branches, grey crosses), 3 ( $n = 7$ , green crosses), 5tt ( $n = 9$ , magenta crosses) and 5st ( $n = 6$ , blue crosses)

pyramidal cells. **(c)** Same as in (b) for density of excitatory (red crosses) and inhibitory (blue crosses) synapses. Note the clear distinction of synaptic input composition in the distal tuft for L2 and L3 vs. L5 pyramidal cells (Kruskal-Wallis test,  $p < 10^{-4}$ ). **(d)** Summary of distinct inhibitory input fraction for four main classes of apical dendrites in the cerebral cortex. Note that L3 neurons are the only cell-type with homogeneous ratio of inhibitory and excitatory synaptic inputs along their apical dendrite. Error bars indicate mean  $\pm$  SEM. This figure is reproduced with modifications from (Karimi, Odenthal et al. 2019) and is licensed under the CC-BY-NC-ND 4.0.

#### **8.1.6. Distance to the soma as a determining factor for inhibitory fraction at the main bifurcation**

Next, we asked whether the apparent difference between L2 and L3/5 inhibitory fraction at their main bifurcation could be generated through a mechanism that depends on the distance between this structure and the cell body of origin (Figure 11a). We therefore measured the path distance between the cell body and main bifurcation for each AD type and inspected the relationship with the inhibitory size at the main bifurcation (Figure 11b). The inhibitory fraction had a strong exponential relationship for almost all pyramidal cell types with the exception of L5st neurons ( $R^2 = 0.73$ ,  $p < 10^{-22}$ , exponential model). The exponential relationship was also observed within the L2 neurons. This suggests a possible soma-dependent mechanism to control the fractional number of inhibitory synapses. Interestingly, this relationship was not as strong for individual synapse densities ( $R^2 = 0.009$ , 0.55 for exponential model fits to excitatory and inhibitory synapse densities, respectively).

We were also wondering if there was a general distance-to-soma dependence of the inhibitory fraction along the apical dendrite of pyramidal neurons in regions other than the main bifurcation. To investigate this, we focused on the layer 2 pyramidal neurons where we had dense synaptic input mappings covering the first  $\sim 330 \mu\text{m}$  of the path distance to soma. We then measured the inhibitory fraction at  $10 \mu\text{m}$  distance bins from soma for all L2 annotations (Figure 11d). A strong exponential relationship between the inhibitory fraction and the distance to soma was observed (Figure 11e).

This meant that the inhibitory fraction (starting at about 100%) exponentially decreased within the first ~100  $\mu\text{m}$  path distance from the soma to reach its baseline level (~10%).

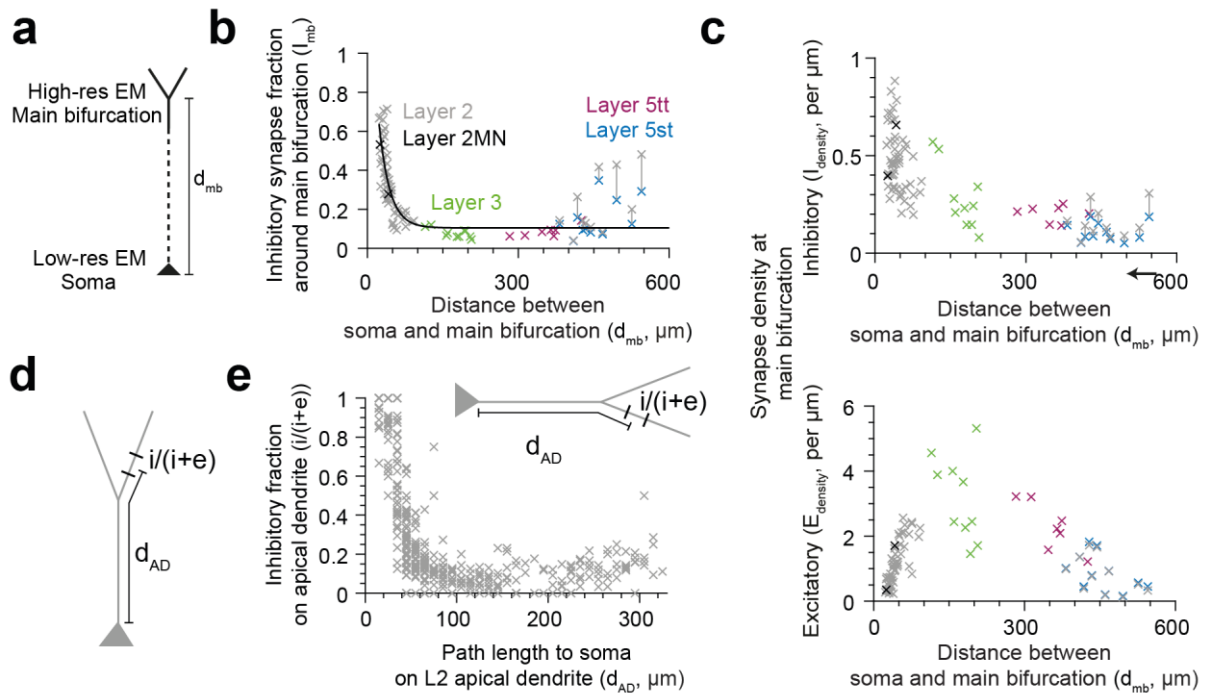


**Figure 11. Distance of the dendritic segment to soma controls inhibitory fraction**

**(a)** Schematic demonstrating the distance between soma (in low-resolution EM) and AD main bifurcation (in high-resolution EM). **(b)** Relationship between distance of main bifurcation to soma and inhibitory fraction at the main bifurcation for layer 2 ( $n = 51$ , grey), 2MN ( $n = 2$ , black), 3 ( $n = 10$ , green), 5tt ( $n = 7$ , magenta), 5st ( $n = 11$ , blue) ADs. Black line indicates single exponential regression ( $I_{mb} = 1.56 * e^{-0.046 * d_{MB}} + 0.1$ ,  $R^2 = 0.73$ ,  $p < 10^{-22}$ ). **(c)** Same as in (b) for individual inhibitory (upper panel) and excitatory (lower panel) synapse densities at the main bifurcation. **(d)** Schematic demonstrating the path distance of a dendritic segment to cell body of a layer 2 pyramidal neuron. **(e)** Scatter plot demonstrating the relationship between dendritic distance to soma ( $d$ ) and the fraction of inhibitory synapses on L2 apical dendrites ( $n = 61$ , S1, V2, PPC, ACC, PPC-2 and LPtA datasets,  $n = 12,532$  synapses). Each cross represents the inhibitory fraction ( $i/(i+e)$ ) for a single apical dendrite within a 10  $\mu\text{m}$  path length range ( $d_{AD}$ ) to cell body of origin. This figure is reproduced with

modifications from (Karimi, Odenthal et al. 2019) and is licensed under the CC-BY-NC-ND 4.0.

### 8.1.7. Depth dependence of synapse composition for pyramidal neurons

Our next goal was to understand the relationship between the cortical depth and inhibitory fraction in pyramidal cell types. To perform this analysis, we transformed all the annotations into a common coordinate system where distance to pia was matched to one of the axes (Figure 12). Next, we virtually sliced the annotations (slice thickness = 100  $\mu\text{m}$ , depth range from pia = 10-330  $\mu\text{m}$ ) and measured the synaptic composition along the superficial layers of cortical surface (Figure 13a-b). We also reported the number of unique ADs and total path length for each cell type (Figure 13c).

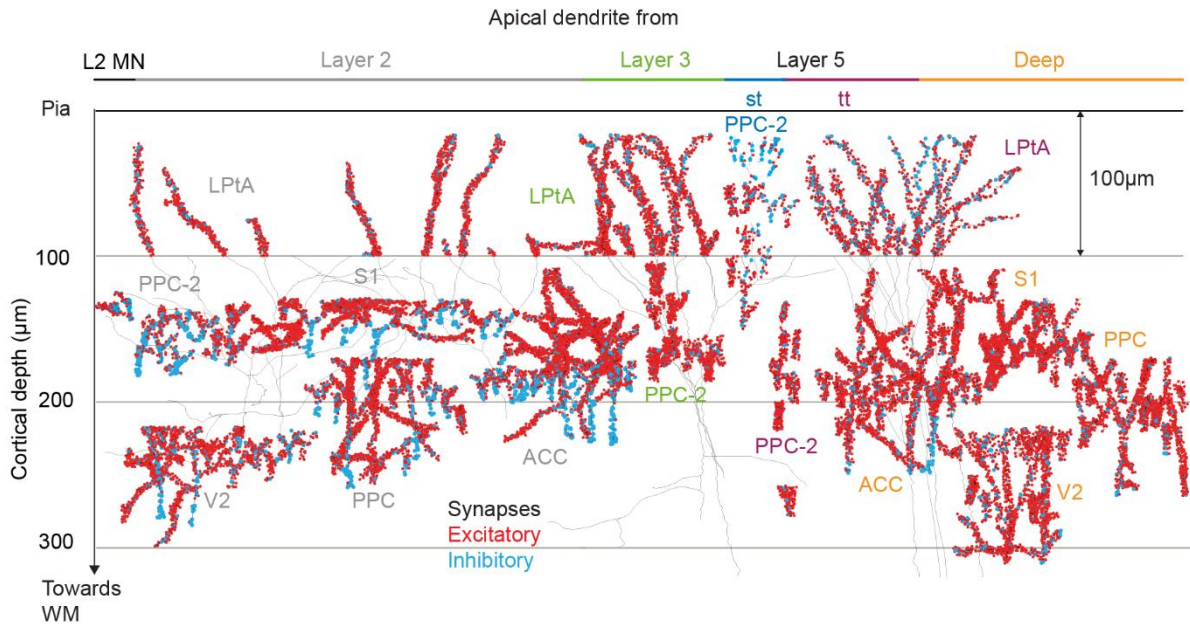


**Figure 12. Complete synaptic input map of segments of layer 2-5 pyramidal neurons**

Complete synapse annotation for 141 unique layer 2, 3, 5 ADs (red: excitatory,  $n = 22,825$ , cyan: inhibitory  $n = 3,723$ , total AD shaft path length = 14.1 mm). Four datasets containing layer 2 ( $n = 20, 20, 22, 28$  for S1, V2, PPC, ACC, respectively), one dataset from layer 1 ( $n = 11$ , LPTA), and one containing both layers ( $n = 40$ , PPC-2) was used. Note the difference in synapse densities (red/cyan sphere density) for layer 2, 3, 5tt, 5st and deep (L3/5) ADs at different

cortical depths relative to pia. Horizontal location of the skeleton reconstructions is adjusted for illustration. All annotations were done in collaboration with Jan Odenthal (equal contributions). This figure is reproduced with modifications from (Karimi, Odenthal et al. 2019) and is licensed under the CC-BY-NC-ND 4.0.

We found that similar to our targeted analysis of main bifurcation and distal AD, the synaptic composition is unique for each AD type. L2 pyramidal neurons had higher inhibitory input around the main bifurcation area (depth range: 100-200  $\mu\text{m}$ ) as compared to distally in L1 (Figure 13b, grey line). Alternatively, L5 neurons had their increased inhibitory input in their distal AD region (depth range: 0-100  $\mu\text{m}$ ). L3 neurons had consistently low inhibitory input along their apical dendrites (depth range: 0-200  $\mu\text{m}$ ).

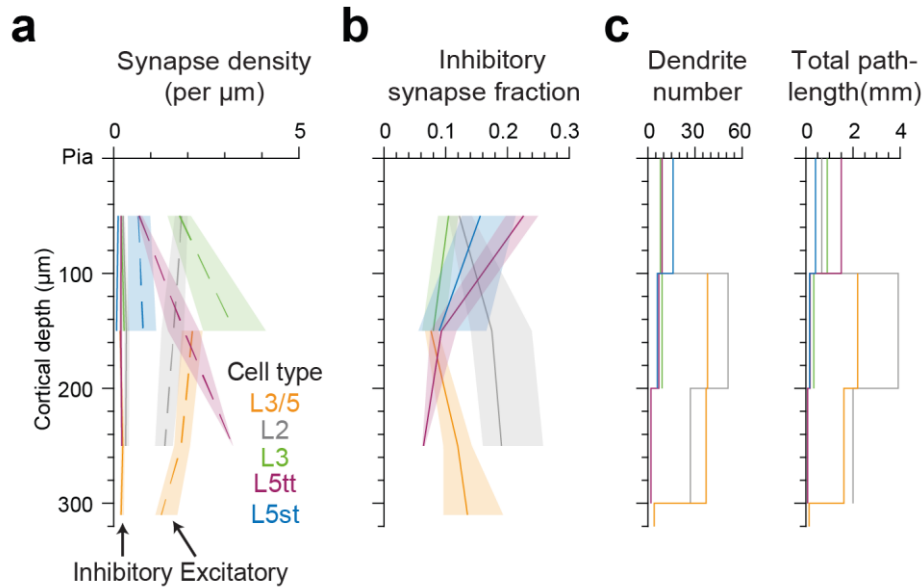


**Figure 13. Synaptic densities across upper cortex for pyramidal neurons**

**(a)** Spatial distribution of excitatory (dashed line) and inhibitory synapse densities (solid line) for L2 (gray), 3 (green), 5tt (magenta), 5st (blue) and 3/5 (deep, orange) ADs in upper cortex as shown in Figure 12 (bin size=100  $\mu\text{m}$ ). Lines and shades indicate the total average and 95% bootstrap confidence interval ( $n = 10,000$  resamples) for data combined across all datasets, respectively. **(b)** Same as in **(a)** for fraction of inhibitory synapses. **(c)** Histogram of the number of dendrites and total AD shaft path length within each cortical



depth bin. This figure is reproduced with modifications from (Karimi, Odenthal et al. 2019) and is licensed under the CC-BY-NC-ND 4.0.

#### **8.1.8. Synapse size and spine properties around the main bifurcation**

To ensure that synapse strength did not compensate for the synapse number differences between the main bifurcation of L2 and deep (L3/5) ADs, we measured the synapse size, which is indicated to predict synapse strength (Harris and Stevens 1989, Buchs and Muller 1996, Cheetham, Barnes et al. 2014, Holler-Rickauer, Koestinger et al. 2019). We assumed an elliptical shape for each synapse and measured the two axes in the EM volume to estimate the interface area (Figure 14a). We found the L2 and deep AD spine synapse (excitatory) interface areas to be similar in the S1, V2, PPC and ACC datasets (Figure 14b,  $n = 41$  per AD type,  $p = 0.12$ , Wilcoxon rank-sum test). Interestingly, the shaft synapses (inhibitory) were slightly larger in L2 ADs where their density is higher as well (Figure 14b,  $p = 0.02$ , Wilcoxon rank-sum test,  $n = 41$  per AD type).

In addition, we measured the fraction of spines which were innervated by two axonal boutons. These double-innervated spines were previously reported to receive both excitation and inhibition (Kubota, Hatada et al. 2007). The double-innervation of spines in L2 AD main bifurcations was increased as compared to deep layer ADs (Figure 14c,  $n = 41$  AD main bifurcations per AD type,  $p = 0.01$ , Wilcoxon rank-sum test). This meant that synapse number, size and double innervation of spines all point towards an increased inhibition in L2 pyramidal neurons around their main bifurcation in the cortical region investigated (Figure 5d, 14a-c).

Spine apparatus were first observed in EM micrographs of dendritic spines and their role has been enigmatic ever since (Gray and Guillery 1963) (Figure 14d, EM micrograph example). It has been suggested that the apparatus is involved in protein synthesis as well as synaptic maturation and stabilization (Špaček 1985, Segal, Vlachos et al. 2010). We, therefore, annotated a subset of spines for the existence of spine apparatus (Figure 14d). Our preliminary results ( $n = 20$  individual spines per AD type) showed a ~2-fold variation in the fraction of spines containing apparatus between pyramidal cell types, with L2 ADs having the highest (65%) and L5tt having the lowest apparatus-containing fraction (25%) (Figure 14d, upper panel). Alternatively, the

density of spines possessing a spine apparatus (per  $\mu\text{m}$  AD shaft path length) is largest for L3 ADs since they have the highest spine density as well (Figure 14d, lower panel. Also see Figure 9c for spine (excitatory synapse) densities).

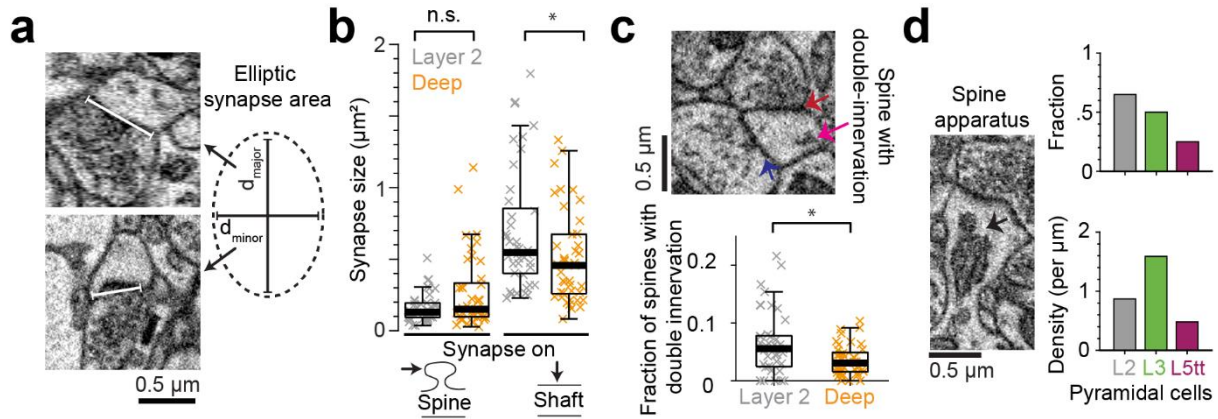


**Figure 14. Properties of synapses and spines around the main bifurcation**

**(a)** Elliptic estimation of synapse area (right) by annotating the two axis of a synaptic interface. Example EM micrographs (left). **(b)** Synaptic interface area for synapses onto deep ( $n = 41$ , orange crosses) and layer 2 ( $n = 41$ , grey crosses) ADs. **(c)** Fraction of double-innervated spines in the main bifurcation of deep (orange,  $n = 41$ ) and layer 2 (grey,  $n = 41$ ) neurons. Spine with inhibitory (shaft-preferring, blue arrow) and excitatory (spine-preferring, red arrow) inputs (inset). **(d)** Bar plots of fraction (upper panel) and density (lower panel, per  $\mu\text{m}$  AD shaft length) of spines with a spine apparatus (example EM micrograph, left) in L2, L3 and L5tt neurons ( $n = 20$  spines per cell type). Asterisks indicate significance level of the Wilcoxon rank-sum test (not significant (n.s.):  $p > 0.05$ , \*  $p < 0.05$ ). Panels (b-c) are reproduced with modifications from (Karimi, Odenthal et al. 2019) and licensed under the CC-BY-NC-ND 4.0.

### **8.1.9. Postsynaptic dendritic targets of excitatory and inhibitory synapses and the effect on the estimation of synapse densities**

We identified excitatory and inhibitory axons based upon their previously reported preference to target spine and shaft of apical dendrites, respectively (White and Rock 1980, White and Hersch 1982, Kubota, Hatada et al. 2007, Chen, Villa et al. 2012). However, exceptions to this structural distinction of inhibitory and excitatory synapses has been reported (Kwon, Merchán-Pérez et al. 2018, Santuy, Rodriguez et al. 2018).

Therefore, we reconstructed a subset of the axons innervating spine and shaft of ADs to discover their excitatory or inhibitory identity. Our goal was to use the additional synapses within the EM-volume to estimate the distribution of the spine-preference for axons seeded from each cell type (Figure 15a, 7 synapses per axon, median, range: 2-405 synapses). This would allow us to classify axons into shaft- and spine-preferring groups that likely correspond to inhibitory and excitatory, respectively. We found an almost binary preference with axons targeting either spine or shaft of dendrites in layers 1 and 2 (Figure 15b, dashed line indicates the 50% threshold). This suggests a low overall error rate of less than 4%, if synapses are classified by their spine vs. shaft incidence locations (Figure 15c, Table 4).

Interestingly, L5st neurons had a significant proportion of excitatory input on their AD shafts in L1/2 (44-60% of shaft synapses were targeted by spine-preferring axons, likely excitatory). This meant that synaptic identification based on location of synapse (spine vs. shaft) would have resulted in an over-estimation of their inhibitory fraction in L1 and 2. Therefore, we corrected the synapse densities based on the synapse type prediction errors (Figure 9, 10, pre-correction values (grey crosses) were connected to the post-correction synapse densities (blue crosses)).

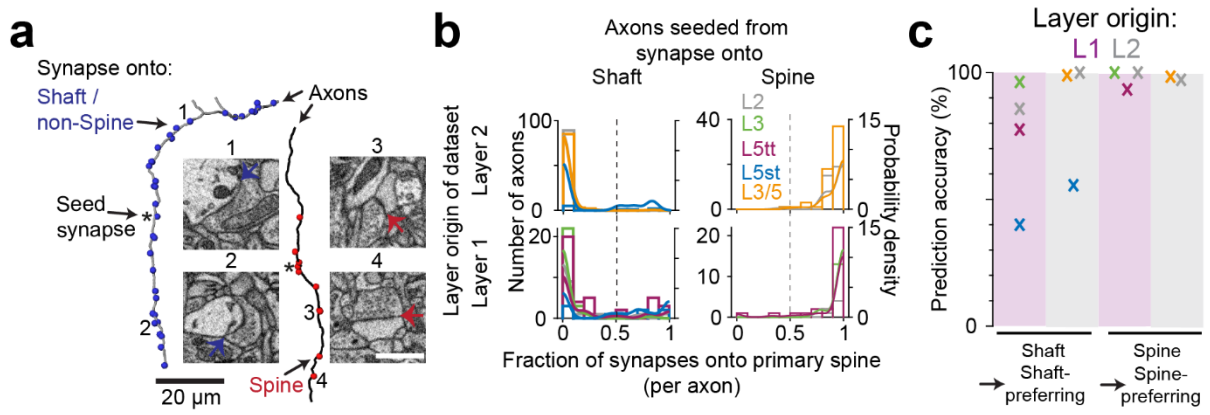


**Figure 15. The dendritic target of excitatory and inhibitory synapses and its effect on the fraction of inhibitory synapses**

**(a)** Synapses of axons (red and blue sphere: spine and shaft/non-spine, respectively) seeded from shaft (grey trace) and spine (black) of apical dendrites in PPC. Note the stark difference in spine preference between the two axons. Example EM cross-section of spine (red arrows) and shaft (blue arrows) synapses (inset). Stars indicate the seed synapse. **(b)** Histogram of the fraction of synapses made onto single-innervated spines for axons seeded from deep (orange), L2 (grey), L3 (green), L5tt (magenta) and L5st (blue) apical dendrite's shaft or spines. Annotations are from layer 1 ( $n = 142$ , LPTA, PPC-2 dataset) and layer 2 ( $n = 288$ , S1, V2, PPC, PPC-2 and ACC datasets); probability density estimations and synapse identity threshold (0.5) as solid and dashed lines, respectively. **(c)** Scattered plot for prediction accuracy of the type of presynaptic axon (spine- vs. shaft-preferring) from the location of synapse on the apical dendrite (spine vs. shaft). Note the highly bimodal distribution in (c), which results in low prediction error rates when classifying synapses based on their location on the dendrite. Scale bar inset (a):  $1 \mu\text{m}$ . Panel (b) is reproduced with modifications from (Karimi, Odenthal et al. 2019) and is licensed under the CC-BY-NC-ND 4.0.

#### 8.1.10. Synapse density normalized to surface area of dendrite

The AD diameter was slightly larger for L2 as compared to deep ADs around the main bifurcation in S1, V2, PPC and ACC (Figure 16a-b,  $2.16 \pm 0.06$  vs  $1.77 \pm 0.04 \mu\text{m}$  for L2 and deep ADs, respectively, mean  $\pm$  SEM,  $n=82$ , Wilcoxon rank sum test,  $p$

$< 10^{-4}$ ). However, the synapse density differences, normalized to the path length, were not affected in a significant manner after normalization to the surface area (compare Figure 16c and Figure 5c). For example, the inhibitory synapse density was still higher for the L2 main bifurcations as compared to L3/5 (Figure 16c, 61% vs. 86% more inhibitory synapses for density normalized to surface and length of dendrite, respectively).

We performed the same analysis for cell-type specific synaptic input maps around the main bifurcation (Figure 16d, see also Figure 9) and in distal apical tuft dendrite (Figure 16e, see also Figure 10). L2 ADs were again larger in diameter as compared to other ADs, especially the L5st main bifurcations (Figure 16d, left panel,  $1.78 \pm 0.06$ ,  $1.38 \pm 0.09$ ,  $1.76 \pm 0.1$ ,  $0.88 \pm 0.04$   $\mu\text{m}$  for L2, L3, L5tt and L5st, respectively,  $n=45$ , Kruskal-Wallis test,  $p < 10^{-4}$ ). In distal apical tufts, L2/3 neurons had thicker dendrites compared to L5 subtypes (Figure 16e, left panel,  $0.89 \pm 0.05$ ,  $0.93 \pm 0.05$  vs.  $0.67 \pm 0.02$ ,  $0.50 \pm 0.02$   $\mu\text{m}$  for L2, L3, L5tt and L5st, respectively,  $n=31$  tuft branches,  $p < 10^{-4}$ , Kruskal-Wallis test). However, the difference between cell types was less distinct for path length and surface normalized densities (Right panels in Figure 16d, e, compare to Figure 10c, 9c).

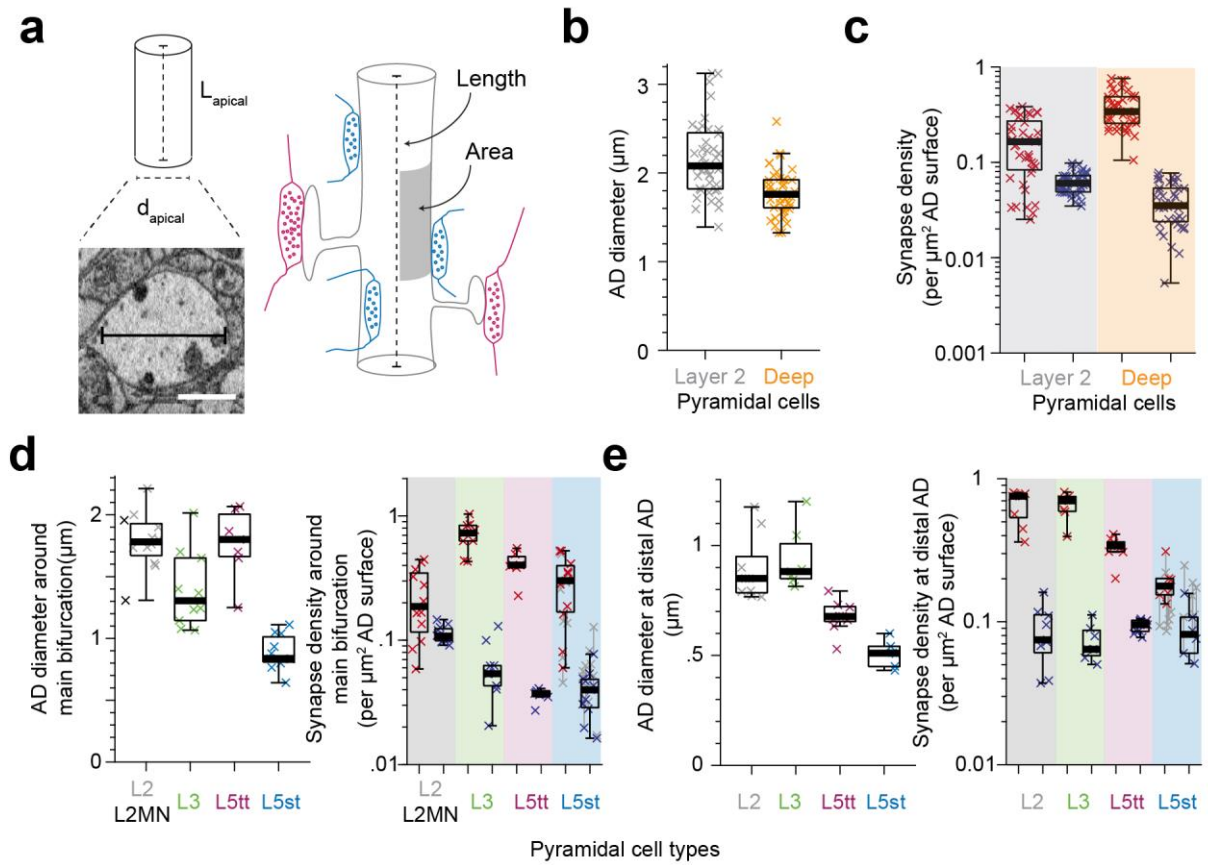


**Figure 16. Apical dendrite diameter and synapse density normalized to the surface area of dendrites**

**(a)** Sketch illustrating the measurement of AD diameter (left panel) and the surface area (right panel) used for synapse density normalization. **(b)** Boxplot of the average diameter of layer 2 (grey,  $n = 41$ ) and deep (orange,  $n = 41$ ) ADs around their main bifurcation in S1, V2, PPC and ACC ( $p < 10^{-4}$ , Wilcoxon rank-sum test). **(c)** Boxplot of inhibitory and excitatory synapse densities (per  $\mu\text{m}^2$  of AD shaft surface area, blue and red crosses, respectively) for L2 ( $n = 41$ , left) and L3/5 ADs ( $n = 41$ , right). Wilcoxon rank-sum test,  $p < 10^{-6}$  for both densities. **(d)** Same as (b, c) for the main AD bifurcation of L2/2MN ( $n = 12$ ), L3 ( $n = 10$ ), L5tt ( $n = 7$ ), L5st ( $n = 11$ ) pyramidal neurons in PPC-2 dataset. Kruskal-Wallis test, AD diameter:  $p < 10^{-5}$ , synapse densities:  $p < 10^{-4}$ . **(e)** Same as (b, c) for the distal apical dendrite tuft of L2 ( $n = 9$ ), L3 ( $n = 7$ ), L5tt ( $n = 9$ ), L5st ( $n = 6$ ) pyramidal neurons in LPtA and PPC-2 dataset. Kruskal-Wallis test, AD diameter:  $p < 10^{-4}$ , excitatory:  $p < 10^{-4}$ , inhibitory density:  $p = 0.43$ . Scale bar in inset (a):  $1 \mu\text{m}$

## 8.2. Innervation profile of AD-targeting inhibitory axons in layer 2 of neocortex

In the following section, we investigated the targeting of subcellular structures in layer 2 of mouse neocortex by AD-targeting inhibitory axons.

### 8.2.1. Cell-type innervation specificity of AD-targeting axons in layer 2

After finding the difference in the inhibitory innervation of AD types (Figure 5), we wanted to understand whether inhibitory axons targeting apical dendrites were specific for the type of AD. Our approach was to measure the conditional innervation probability of L2 and deep ADs conditioned on the target of the seed synapse (Figure 17a, conditional innervation  $P(B|A)$ , A: AD target type of seed (first) synapse, B: AD target type of other synapses).

Next, we reconstructed axons that were randomly seeded from inhibitory shaft synapses of L2 and deep ADs in S1, V2, PPC and ACC cortex (target “A”, Figure 17a, d). The other synaptic targets of these axons were identified and classified within the EM volume. AD-targeting axons innervated apical dendrites with ~20% of all their synapses (Figure 17b, e,  $n=183$ ). To estimate the conditional innervation probability, we calculated the fraction of targets belonging to a specific AD type (see also methods above). The innervation showed about a 3-fold conditional dependence on the seed AD type, rejecting a model of indiscriminate innervation (Figure 17a-c): Axons seeded from deep ADs comprised  $15.4 \pm 1.6\%$  (mean  $\pm$  SEM) of their other output synapses (“B” targets) onto deep apical dendrites (i.e. 71.2% of AD synapses) and only  $5.2 \pm 0.8\%$  (mean  $\pm$  SEM) onto L2 ADs (28.8% of AD synapses, Figure 17b (second row), c (orange crosses),  $n=91$ , Wilcoxon rank-sum test,  $p < 10^{-8}$ ). In contrast, L2 AD-seeded axons only targeted deep ADs  $4.1 \pm 0.6\%$  (mean  $\pm$  SEM,  $n = 92$ ). They rather innervate layer 2 apical dendrites ( $15.9 \pm 1.4\%$ , mean  $\pm$  SEM, i.e. 77.4% of AD synapses).

Next, we identified the other postsynaptic targets of the AD-targeting inhibitory axons and quantified their innervation fraction ( $P(B|A)$ ). As previously reported (Kubota, Hatada et al. 2007), the spine targets of inhibitory axons were almost always co-innervated by an additional (likely excitatory) synapse. In addition, we found L2-seeded axons to be ~2-fold more likely to target layer 2 somata as compared to their

deep-seeded counterparts (Figure 17e,  $19.5 \pm 1.7\%$  vs.  $11 \pm 1.7\%$  of postsynaptic targets for axons seeded from L2 and deep ADs, mean  $\pm$  SEM,  $n = 183$ ). This can, at least partly, be explained by the differences in soma innervation fraction between cortical regions (Figure 20c, see also below).

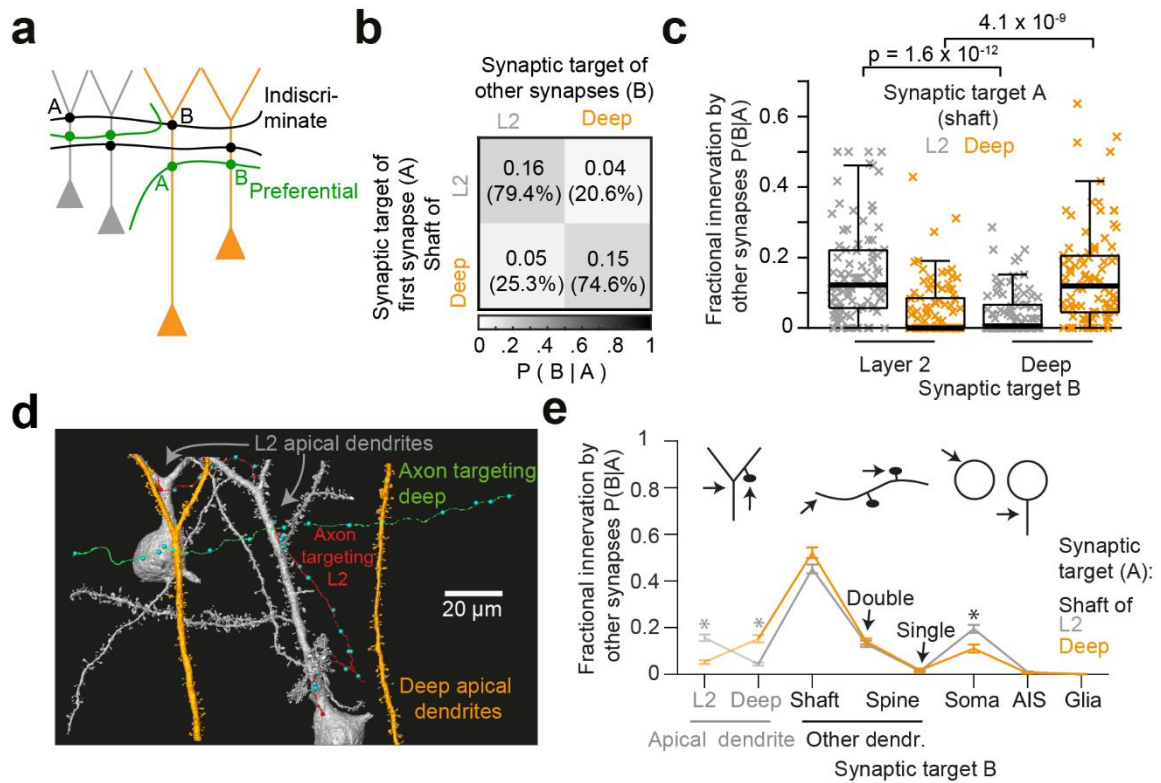


**Figure 17. Cell-type specific innervation of apical dendrites by inhibitory axons in layer 2 of neocortex**

**(a)** Sketch illustrating extreme examples of two innervation models for AD-targeting inhibitory axons: innervation could be selective for the type of AD (L2 vs L3/5 pyramidal cells, green), or rather indiscriminate for the type of AD (black). In the latter case, conditional dependence of targeting  $p(B|A)$  would be expected to be absent. **(b)** Conditional dependence of synaptic innervation  $p(B|A)$  shown as the mean probability of deep and layer 2 AD targeting (target “B”) given the target of the first synapse of an axon (target “A”). Probabilities are the maximum-likelihood estimate mean of a Dirichlet-multinomial fit to the data. Numbers represent the absolute and fractional (in percent) innervation



probability for ADs. **(c)** Boxplot of AD fractional innervation for axons seeded from layer 2 ( $n = 92$ , grey crosses) and deep ( $n = 91$ , orange crosses) ADs, corresponding to the entries in the innervation matrix (b).  $P$  values are from the Wilcoxon rank-sum test. Note the innervation preference for AD types. **(d)** Two example axons targeting layer 2 (grey) and deep layer (orange) apical dendrites preferentially. Blue spheres indicate the location of all their output synapses in the PPC dataset. **(e)** Mapping of axonal output onto subcellular targets. Error bars indicate mean  $\pm$  SEM; asterisks: significance of bootstrapping test with  $\alpha=0.05$  and Bonferroni correction. This figure is reproduced with modifications from (Karimi, Odenthal et al. 2019) and is licensed under the CC-BY-NC-ND 4.0.

### 8.2.2. Distribution of pre- and postsynaptic targets across cortex

One possible way to implement innervation specificity is to physically separate the pre- or post-synaptic targets along the depth of the cortex (Figure 18a). Therefore, we mapped the density of pre- and postsynaptic partners along the cortical depth in S1, V2, PPC and ACC. Pre-synaptically, we found the density of the investigated main bifurcation to be similar across the upper cortex (Figure 18b,  $n = 41$  per AD type). In addition, the density of axonal path was nearly identical across the same cortical depth (Figure 18c, 18.1 vs. 16.7 mm for deep and L2, respectively,  $n = 183$ ). This suggests connectivity specificity beyond geometric separation of synaptic partners.

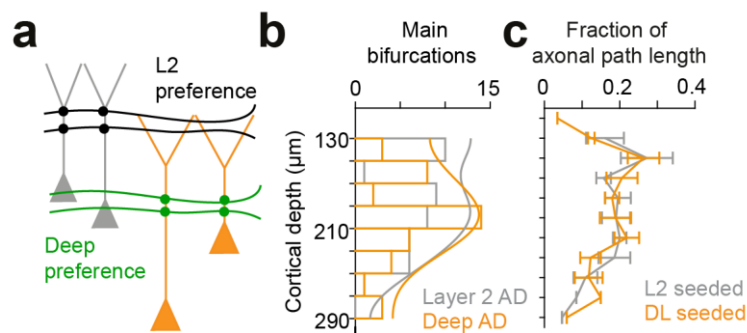


**Figure 18. Spatial distribution of main bifurcation of ADs and axons across the upper cortical layers**

**(a)** Sketch illustrating how geometric separation could result in targeting preference of AD-targeting inhibitory axons. **(b)** Distribution of analyzed main bifurcations along the cortical depth ( $n = 41$  per AD type; probability density estimates, lines). **(c)** Distribution of axonal path length along cortical depth. ( $n = 183$  axons, of these  $n = 92$  seeded at L2 (gray) and  $n = 91$  seeded at deep layer ADs (orange)). Note that neither the pre- nor the post-synaptic targets are sorted along the cortical axis, excluding simple layering effects (a) for the conditional innervation (Figure 17a-c). Error bars indicate mean  $\pm$  SEM over cortical region (S1, V2, PPC and ACC). Panels (b-c) are reproduced with modifications from (Karimi, Odenthal et al. 2019) and licensed under the CC-BY-NC-ND 4.0.

### 8.2.3. Multiple innervation of apical dendrites by inhibitory axons

Axons are known to innervate pyramidal neurons multiple times in a clustered manner (Schmidt, Gour et al. 2017, Bloss, Cembrowski et al. 2018). We, therefore, quantified the extent of multiple-innervation of ADs by inhibitory axons and its impact on innervation specificity (Figure 19a). Interestingly, inhibitory axons mostly target apical dendrites by a single synapse within a volume of about  $10^6 \mu\text{m}^3$  in S1, V2, PPC and ACC (Figure 19d, 75.6% vs 79.1% of total targets for axons seeded from L2 and deep ADs, respectively). We also measured the average number of synapses onto individual ADs for each axon and found it to be similar between L2- and deep-seeded axons (Figure 19b,  $1.32 \pm 0.05$  vs.  $1.28 \pm 0.04$  synapses per AD target for axons seeded from L2 and deep layer ADs, respectively, Wilcoxon rank sum test,  $p = 0.83$ ). To understand the effect of multiple innervation on AD innervation preference, we measured the fraction of individual L2 and L3/5 AD targets ignoring multiple innervation of the same AD (Figure 19c,  $70 \pm 3.6\%$  vs.  $35.2 \pm 4.1\%$  individual L2 target fraction for axons seeded from L2 and deep layer ADs, respectively, mean  $\pm$  SEM,  $n=159$ , Wilcoxon rank sum test,  $p < 10^{-7}$ ).

It is more likely to select axons that target the seed AD multiple times if the process is random on the individual synapse level. Interestingly, we found the distribution of the number of times the seed structure was innervated to be skewed towards multi-innervation, as compared to the other targets (compare Figure 19d,e, 59.5% vs. 21% of single-innervation for seed vs. other targets). Therefore, we removed

all the seed synapses to calculate the individual AD innervation fraction (Figure 19c, bottom matrix).

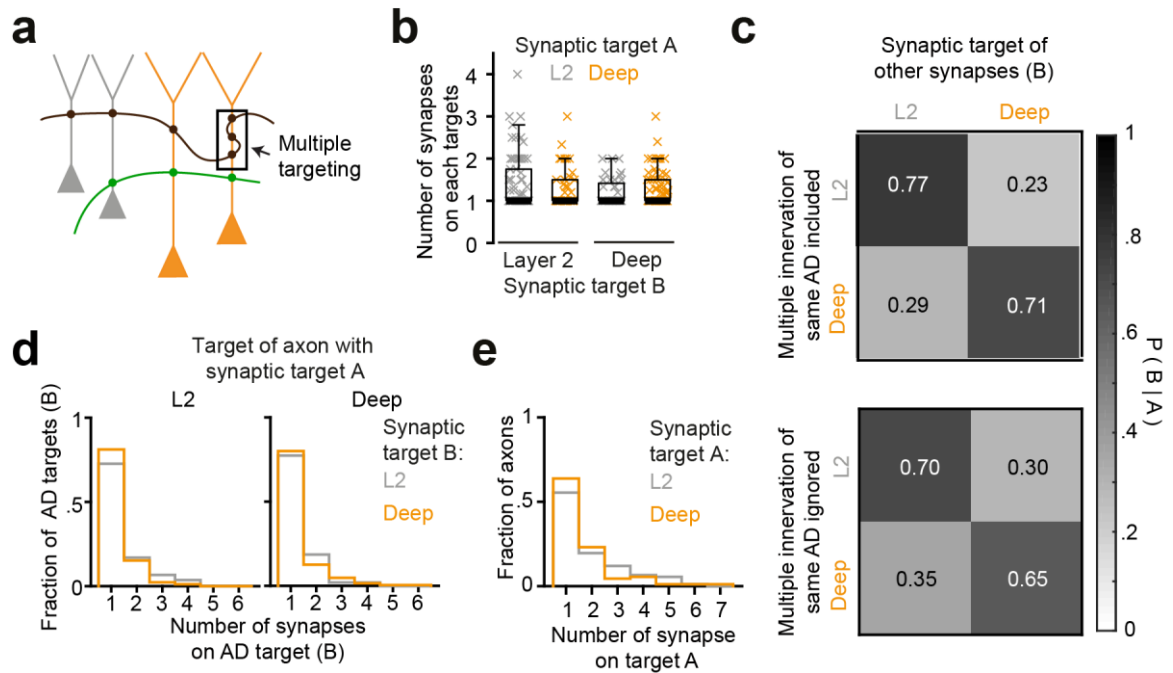


**Figure 19. Multiple innervations of apical dendrites by inhibitory axons**

**(a)** Sketch illustrating multiple innervation of one apical dendrite by the same axon. **(b)** Boxplot of the average number of synapses on L2 (left) and deep AD targets (right). Wilcoxon rank-sum test,  $p = 0.54$ ,  $0.20$  for axons with first synapse on L2 (grey) and deep (orange) ADs, respectively. **(c)** Matrix of conditional targeting probability of an AD type (target "B", also see Figure 17a-b), given the type of AD the axon is seeded from (target "A" or seed, rows). The probability is given using two methods: 1. Average over fractional innervation of individual axons (top matrix, only first seed ("A") synapse excluded). 2. Multiple innervations of the same AD target ignored (bottom matrix, all seed innervations excluded). **(d)** Histogram of the number of synapses per AD target for axons seeded from L2 (left panel) and deep (right) ADs. Note the majority of targets receive one synapse (75.6% and 79.1% of targets for axons seeded from L2 and deep ADs, respectively). **(e)** Histogram of the seed "A" targeting multiplicity of inhibitory axons. Note the longer tail compared to (d) due to the seeding process (see text above).

### 8.2.4. Comparing inhibitory axon innervation preference across mouse cortex

Across four cortical regions, we found the distribution of postsynaptic innervation probability for L2- and deep-seeded inhibitory axons to be quantitatively consistent (Figure 20a-c). We only found the somatic innervation by the deep-seeded axons to be significantly different across cortical regions (Figure 20b-c, MANOVA test, followed by multiple one-way ANOVAs with Bonferroni correction).

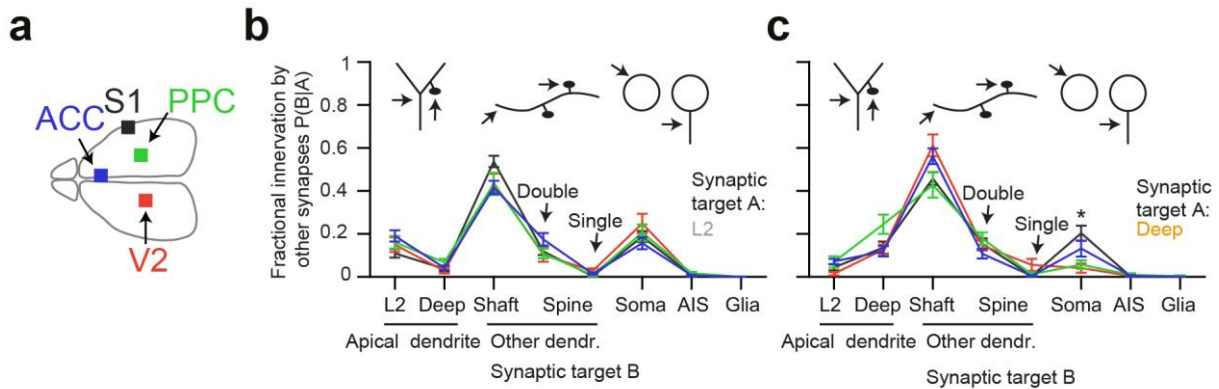


**Figure 20. Consistent innervation profile of inhibitory axons across the neocortex**

**(a)** Sketch of the mouse cortex with the four regions investigated (S1, V2, ACC and PPC). See also Figure 4a-c. **(b,c)** Comparative analysis across cortical regions. Postsynaptic target specificity for axons seeded from (b) layer 2 ADs ( $n = 21, 20, 21, 30$  for S1, V2, PPC and ACC, respectively) and (c) deep layer ADs ( $n = 19, 20, 20, 32$  for S1, V2, PPC and ACC, respectively). Note the quantitative consistency of synaptic innervation across cortices with one exception: somatic innervation in axons seeded from deep layer ADs. Error bars indicate mean  $\pm$  SEM. \* $p < 0.05$  MANOVA test followed by multiple one-way ANOVA tests with Bonferroni correction. This figure is reproduced with modifications from (Karimi, Odenthal et al. 2019) and is licensed under the CC-BY-NC-ND 4.0.

### **8.3. Correlative 3D-EM in the posterior parietal cortex**

In the following section, we describe the analysis of long-range input to posterior parietal cortex (PPC) and the automated aberration adjustment software used to acquire an SBEM dataset spanning layers 1-5 of PPC.

#### **8.3.1. Automatic aberration adjustment of long-term SBEM experiments**

To acquire a dataset spanning layers 1-5 of neocortex, it was essential to implement an automated routine to monitor aberrations of the electron microscope (EM). The EM beam cross-section needs to be minimized at the surface of the sample to get the highest image resolution. To achieve this goal, the strength of the objective lens and two stigmator elements are usually optimized by imaging a sacrificial area repeatedly (Figure 21a). This was not possible in heat-sensitive SBEM samples with repetitive ultra-thin sectioning. Therefore, we implemented a previously reported heuristic approach using the shape of the autocorrelation of SBEM images (Figure 21b, (Binding, Mikula et al. 2013), “heuristic algorithm”).

The autocorrelation of an image is dependent on the level of detail (high-frequency elements) present. We, therefore, excluded large objects by a combination of edge detection and morphological heuristics in EM-micrographs (Figure 21d). We next cropped a pixel region containing neuropil and calculated its autocorrelation (Figure 21b, example EM micrographs and their autocorrelation). Subsequently, a set of 6 masks was used to get an uncalibrated estimator for the aberrations present in the EM image (2 masks per aberration, Figure 21c). Finally, we used test images with known aberrations to calibrate these estimators for each microscope. This software package was successfully used across two microscopes to acquire 10 datasets from 3 animal models by 5 experimenters (Figure 22, Table 6).

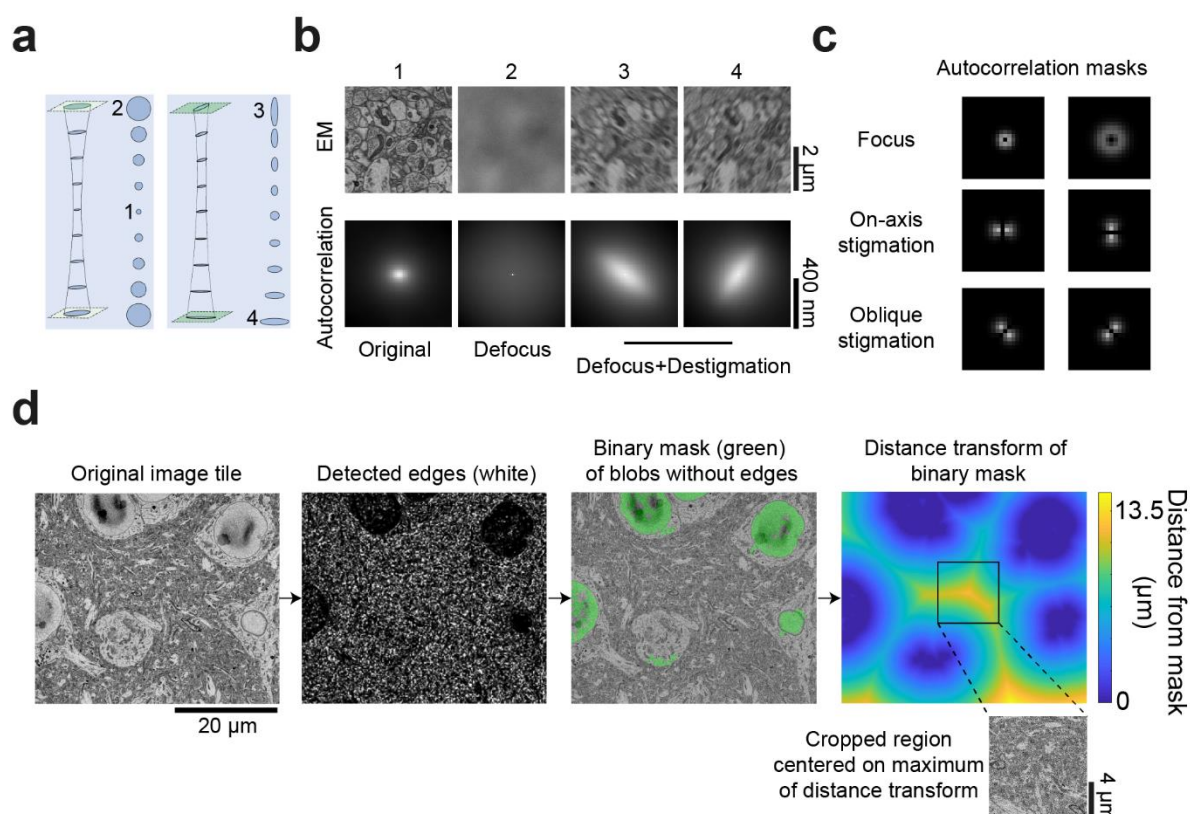


**Figure 21. Design of software for automatic adjustment of objective lens and stigmators in 3D electron microscopy**

**(a)** Illustration of symmetric (left) and asymmetric (right) beam cross-section around the focal point of the beam. **(b)** EM micrographs (top row) and the corresponding center of the autocorrelation image (bottom row) for images with best manual focus/stigmatism (1), 100  $\mu\text{m}$  defocus (2), 10  $\mu\text{m}$  under (3) and over (4) focus with one of the EM stigmators deviated from optimum. Numbers match the schematics in (a). Note the asymmetric loss of image details in 3 and 4. **(c)** Weight functions used for obtaining deviation coefficients for focus and stigmatism from the autocorrelation of an image. Note that the shape of these weight functions is suitable for determining symmetric (focus) and asymmetric (stigmatism) aberrations. **(d)** Image processing pipeline for avoiding large objects (blood vessels and nuclei) using edge detection, heuristic morphological operation and a distance transform. The detected edges were dilated for visualization purposes (second panel from left). The cropped region is used for aberration estimation. Panel (a) is reprinted with permission from Springer

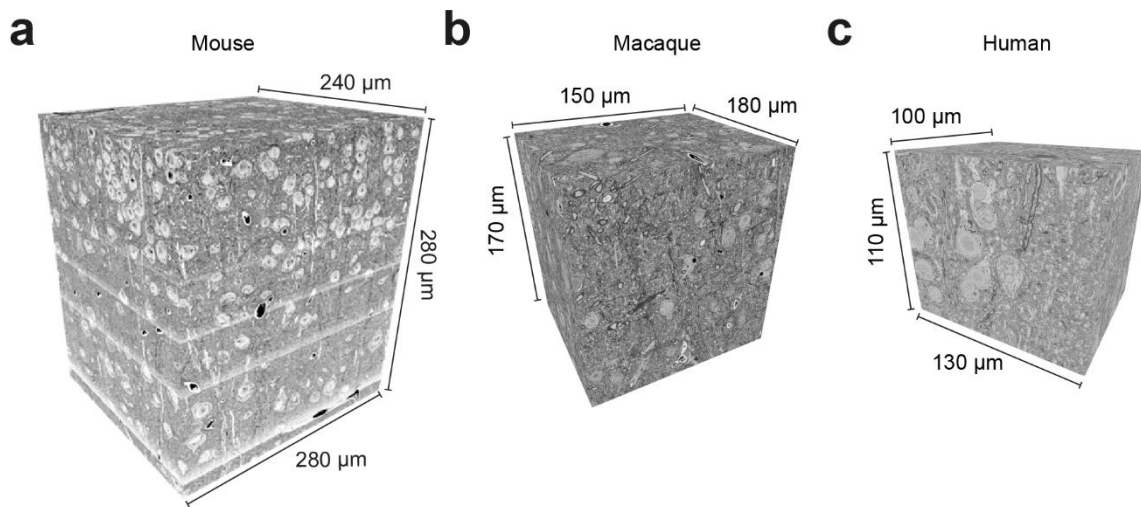


**Figure 22. Example datasets acquired by colleagues using automatic aberration adjustment software**

**(a-c)** Datasets acquired using the automated aberration adjustment software from layer 4 of primary somatosensory cortex (S1) in mouse (a), macaque monkey (b), and medial temporal gyrus of human (c). Datasets were acquired and their overview image here provided by Kun Song (a), Jakob Straehle and Sahil Loomba (b,c). See Table 6 for details.

### **8.3.2. Application of FluoEM to input from secondary motor (M2) and primary visual (V1) areas to posterior parietal cortex (PPC)**

We applied the correlative fluorescent light and electron microscopy technique developed in our lab to investigate the synaptic targets of long-range innervation to PPC (Figure 23, FluoEM, (Drawitsch, Karimi et al. 2018)). The long-range axons from V1 and M2 expressed the fluorescent proteins eGFP (green) and tdTomato (red) by targeted injection of adeno-associated viruses (AAVs). We next acquired a correlated volume of  $216 \times 162 \times 93 \mu\text{m}^3$  in PPC using 3D confocal laser scanning microscopy and SBEM (Figure 23b). The fluorescently labelled axons were matched to their EM counterparts using the “FluoEM” approach (Drawitsch, Karimi et al. 2018). FluoEM



matches axons across LM and EM datasets using morphological constraints, such as, axonal path and bouton placement.

We matched 24 axons between the two datasets using 384 axonal boutons as control points (Figure 23c-d, residual error:  $1.5 \pm 0.8 \mu\text{m}$  vs.  $86 \pm 100 \text{ nm}$  for affine and freeform transformations, respectively, mean  $\pm$  SD). We next mapped all the synapses of long-range axons within the EM volume and found the synapse density to match the previously reported cortico-cortical excitatory axons (Figure 23e, see also (Motta, Berning et al. 2019)).

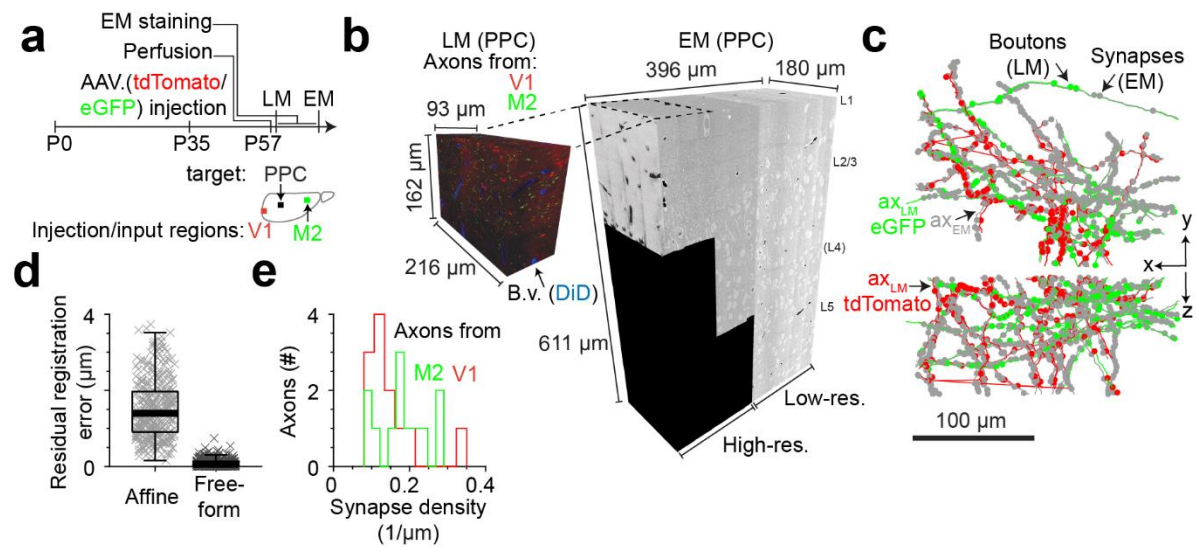


**Figure 23. Application of FluoEM, correlated light and electron microscopy, to motor (M2) and visual (V1) input to posterior parietal cortex (PPC)**

**(a)** Illustration of experimental steps: injection of wild-type C57BL/6 mouse with adeno-associated viruses (AAVs) for expression of fluorescent proteins in secondary motor (M2, AAV.eGFP, green) and primary visual cortices (V1, AAV.tdTomato, red) at postnatal day 35 (P35). Sample was extracted from posterior parietal cortex (PPC, black) for 3D fluorescent confocal light (LM) and electron microscopy (EM). Illustration of the approximate location of input and target cortical regions in horizontal view of the mouse cortex (inset). **(b)** High and low-resolution 3D-EM data (right, voxel size of  $11.24 \times 11.24 \times 30$  and  $22.48 \times 22.48 \times 30 \text{ nm}^3$ , respectively) and the corresponding LM dataset (left, voxel size:  $115 \times 115 \times 444 \text{ nm}$ ). Voxels inside axons expressing eGFP and tdTomato



are green and red, respectively. Blood vessels (blue) were perfused with DiI for coarse registration. **(c)** Overlay of EM skeleton reconstruction of 24 axons (grey) and their matched affine-transformed LM counterpart (red, green traces). The transformation was constrained using axonal boutons and their corresponding synapses in EM (spheres,  $n=348$  control points). Note that some synapses in EM are not detected as boutons in LM. **(d)** Boxplot of residual Euclidian distance between matched control points in (c) for affine and freeform transformations. **(e)** Preliminary analysis of bouton density for long-range axons from V1 (red,  $n = 12$ ) and M2 (green,  $n = 12$ ). Panel (a) is reproduced with modifications from (Drawitsch, Karimi et al. 2018) and is licensed under the CC BY 4.0.

All postsynaptic targets of the long-range axons from M2 and V1 were annotated and handed to student annotators for reconstruction (Figure 24a-b,  $n = 407$  and  $1212$  for axons from M2 and V1, respectively). The students were asked to reconstruct the dendrite fully within the dataset and note the location of soma. About half the postsynaptic targets were found within the volume in our preliminary analysis (Figure 24c-d,  $804/1619$  targets with at least 1 redundant annotation reporting the cell body location).

We next mapped the location of postsynaptic targets for long-range input (Figure 24e,  $n = 660$ ,  $144$  for V1 and M2, respectively). Our goal was to determine whether long-range axons carrying sensory or motor information were specific for the neuronal type of their target. Our initial analysis showed that synaptic input from V1 was more likely to innervate neurons with their soma residing in layer 3 of PPC as compared to input from M2 (Figure 24e-g)

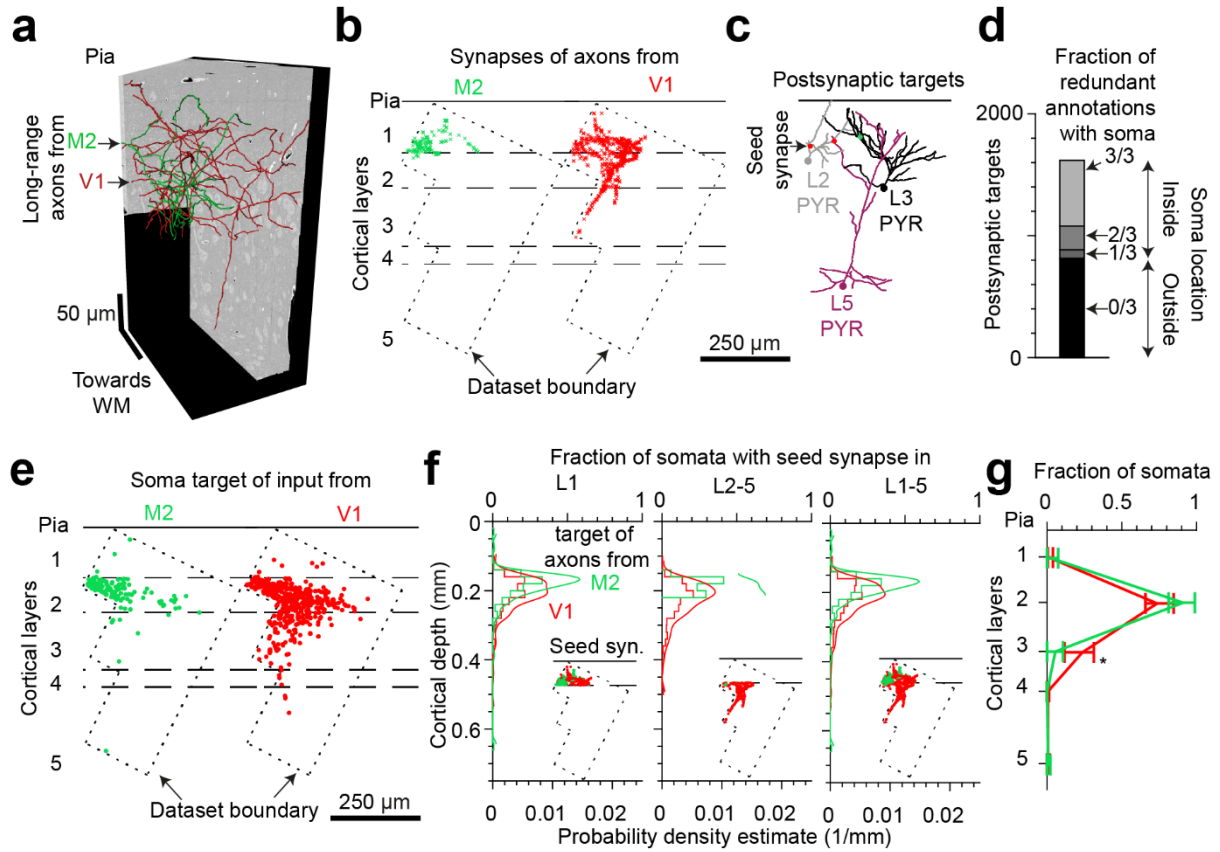


**Figure 24. The depth profile of cell bodies in PPC innervated by axons from secondary motor (M2) and visual (V1) cortices**

**(a)** Skeleton reconstruction of axons in EM with their long-range source extracted using FluoEM ( $n = 24$ , M2: green, V1: red). **(b)** Location of synapses formed by long-range input from M2 (green,  $n = 407$ ) and V1 (red,  $n = 1212$ ). Note that V1 synapses cover a larger area of the dataset in L2-5. **(c)** Example reconstruction of L2 (grey), L3 (black) and L5 (magenta) pyramidal dendrite targets of synapses from long-range M2 (green sphere) and V1 (red sphere) input. **(d)** Bar plot indicating the fraction of redundant annotations ( $n = 3$ ) that reported the location of cell body for their postsynaptic targets; 49.66% (804/1619) of postsynaptic targets had their soma location reported by at least one student annotator. **(e)** Soma depth of postsynaptic targets of axons from M2 ( $n = 144$ ) and V1 ( $n = 660$ ). Note the difference in the propensity of V1 and M2 axons to target L3 neurons. **(f)** Histogram of the fraction of postsynaptic targets (somata, same as in (e)) at each cortical depth (bin size =  $20 \mu\text{m}$ ) for synapses located in L1 (left,  $n = 579$ ), L2-5 (center,  $n = 225$ ) and L1-5 (right,  $n$

= 804). Lines indicate the probability density estimate. Insets in each figure demonstrate the cortical depth of long-range synapses used to generate the corresponding histogram. **(g)** Fraction of soma targets located within each cortical layer for (e). Lines and error bars indicate the gross average and 95% bootstrap confidence interval ( $n = 10,000$  resamples), respectively. Star indicates non-overlapping bootstrap confidence intervals. Dataset boundary and cortical layers were noted with dotted and dashed lines respectively (b,e,f).

We also asked whether the location of synapses formed could generate such a difference in the innervation specificities along the cortex. Therefore, we restricted our analysis to long-range synapses formed in layer 1 and found a similar tendency for V1 axons to target neurons deeper in L2/3 (Figure 24f, left panel).

To find the cortical layers with differential innervation by long-range axons, we compared the bootstrap distributions of postsynaptic target fractions across cortical layers (Figure 24g, left panel, error bars indicate the 95% bootstrap confidence interval,  $n = 10,000$  resamples). L3 neurons were receiving significantly higher fractional input from V1 as compared to M2 (23% vs. 5% of total postsynaptic targets for V1 and M2, respectively). Furthermore, this innervation preference was also observed in targets of individual long-range axons (Figure 25).

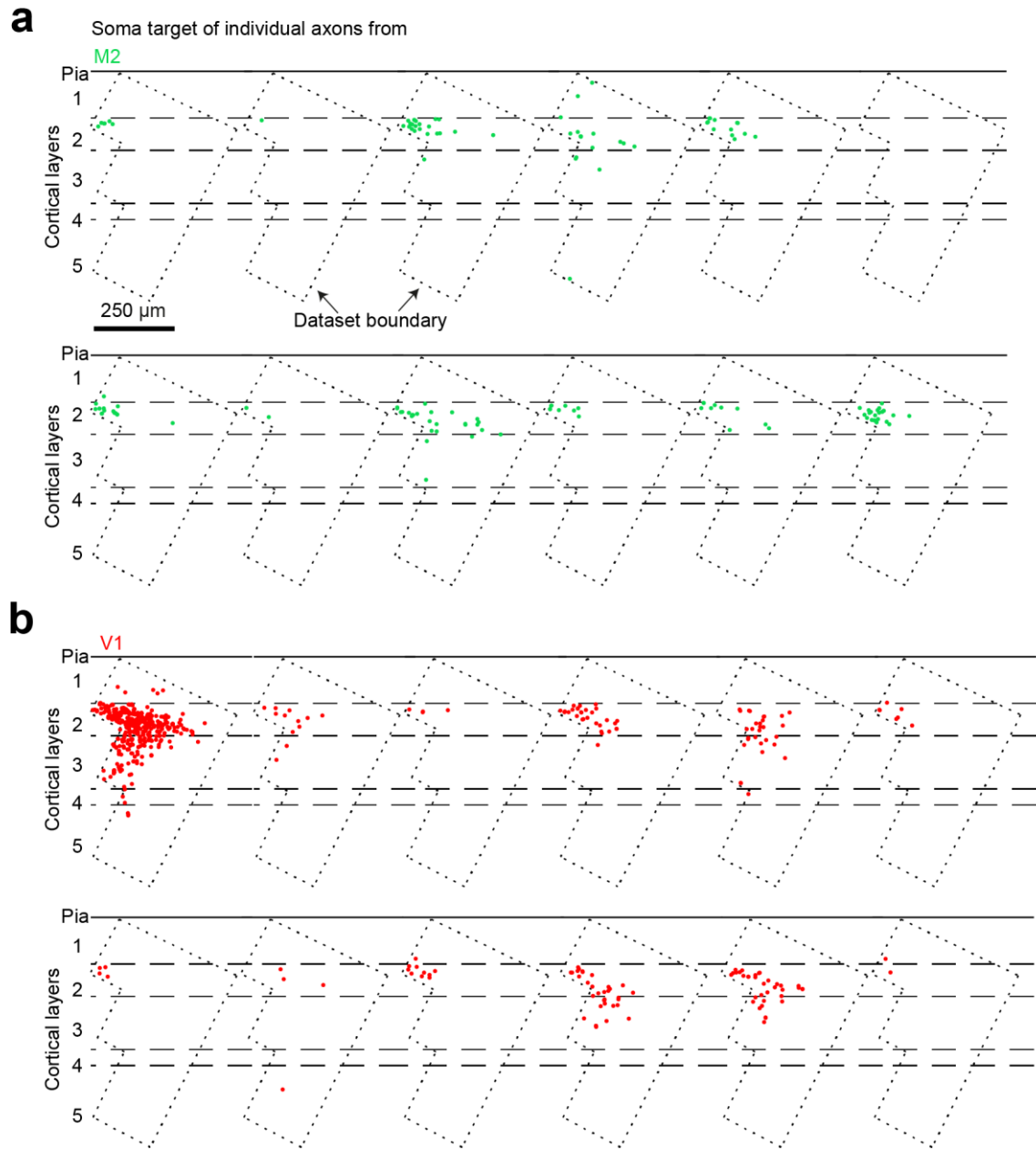


**Figure 25. Cortical depth of soma for postsynaptic targets of individual axons from V1 and M2 cortical regions**

**(a)** Postsynaptic targets of individual long-range axons in PPC from M2 cortex (green spheres,  $n = 12$ ). **(b)** Same as in (a) for axons originating from projection neurons in V1 ( $n = 12$ ). Dataset boundary and cortical layers were noted with dotted and dashed lines, respectively. Note the difference in the innervation of L3 neurons by V1 and M2 long-range axons.

## **9. Discussion**

### **9.1. Cell-type specific synaptic innervation in apical dendrites of pyramidal neurons**

We applied 3D-EM imaging to acquire the first quantitative synaptic innervation map of apical dendrites (ADs) in six image volumes from S1, V2, PPC, ACC and LPtA (Figure 4, 6). The pattern of inhibitory/excitatory synaptic composition on the surface of ADs was distinct for L2, L3, L5tt and L5st pyramidal neurons in layers 1 and 2 (Figure 5, 9, 10, 12, 13). We quantified, or estimated, the effect of the factors that confound or mediate the differences between cell types: distance between soma and point-of-interest on AD (Figure 11), synapse strength (size), double-innervation of dendritic spines (Figure 14), classification criteria (Figure 15), and dendrite diameter (Figure 16). Subsequently, we investigated the innervation specificity in AD-targeting inhibitory axons in S1, V2, PPC and ACC (Figure 17, 20). As controls, we measured the geometric distribution of pre- and postsynaptic structures (Figure 18) and multi-innervation of ADs (Figure 19). In the following sections, the details and context of these results are discussed.

#### **9.1.1. Cell-type specific synaptic composition on apical dendrites**

We used 3D-EM to find distinct patterns of inhibition for the apical dendrites of L2, 3, 5tt and 5st pyramidal neurons in the upper cortex. We focused on measurement of the fraction of inhibitory synapses since the balance between excitation and inhibition controls cellular activity (Koch, Poggio et al. 1983, Liu 2004). Further, inhibitory neurons comprise about 10% of cells in the mammalian cortex (Meyer, Schwarz et al. 2011). Assuming a similar number of local synapses per neuron, the “baseline” fraction of inhibitory synapses within a volume of cortex should also be ~10% (Braitenberg and Schüz 1998). Previously, the dendrites of pyramidal neurons were reported to contain a balanced inhibitory/excitatory ratio (Iascone, Li et al. 2018). Our goal was to find regions where this balance was modified.

We found the inhibition along the apical dendrite to be cell-type specific. L2 pyramidal neurons receive about a ~3-fold increase in inhibition around the main

bifurcation of their apical dendrites. In contrast, L5 neurons receive a ~2-fold increase in the fraction of inhibitory synapses in layer 1. Only L3 has a homogenous baseline fraction of inhibitory synapses around the main bifurcation and more distally in L1. In addition, our preliminary analysis of slender-tufted neurons in L5 (L5st) shows a neuron subtype with increased inhibitory fraction and low excitatory synapse density along its apical dendrite. The pattern of inhibition was surprisingly consistent across S1, V2, PPC and ACC (Figure 10, 12, 13).

We detected the main bifurcation of the apical dendrite for layer 3 and 5 pyramidal neurons by two methods based upon the size and location of the dataset. In datasets containing only layer 2, we examined the main bifurcation of apical dendrites arising from somata located in deeper cortical layers (Figure 4, 5). The second approach used the larger datasets containing layers 2-5 to find the main bifurcation by the apical dendrite reconstruction of a subset of neurons in each layer (Figure 6, 7, 9). The distribution of synaptic densities of L3/5 AD main bifurcations (deep, method I, Figure 5c-f: orange) were similar to that of L3 and L5tt groups combined (method II, Figure 9b-c: green and magenta, respectively). This suggests unbiased sampling of the L3 and L5tt AD types. However, our sample of deep (L3/5) main bifurcations did not include slender-tufted L5 ADs. The reason we didn't detect L5st ADs is most likely due to a combination of our sampling method and L5st's thin diameter (Figure 16d, e). In addition, we specifically searched for L2 marginal neurons using the oblique direction of their apical dendrite relative to pia. In our preliminary analysis, we measured the synaptic densities at the main bifurcation of two L2MN neurons and found similar inhibitory fraction to other L2 neurons (Figure 9).

We expected to see significant inhibitory input to the main bifurcation of layer 5 thick-tufted pyramidal neurons where the amplification of distal input by calcium spikes occurs (Helmchen, Svoboda et al. 1999, Larkum and Zhu 2002, Larkum, Senn et al. 2004). Surprisingly, we found the location with increased inhibitory input, above baseline, to be the distal tuft of apical dendrites in layer 1. This is in agreement with the theoretical investigation demonstrating the effectiveness of distal inhibition on a hot zone of excitatory input around the main bifurcation (Gidon and Segev 2012). Conversely, the L2/3 neurons lacked such distal inhibition.

Across behavioral states, electrical recordings from L2/3 neurons showed a ~10-fold reduced firing frequency as compared to L5 pyramidal neurons (de Kock and Sakmann 2009). Therefore, L2/3 encodes sensory stimuli in a sparser manner compared to L5 (de Kock and Sakmann 2009, Barth and Poulet 2012). The differences in the synapse densities along the AD (Figure 10d) could contribute to the physiological properties of neurons. However, active membrane currents could modify or even reverse the synapse density difference and should be taken into account in a realistic biophysical model (Waters, Larkum et al. 2003, Ledergerber and Larkum 2012).

It is important to note the power of 3D electron microscopy where even the smallest spines and synapses are detectable (Helmstaedter 2013). In light microscopic studies, the general approach is to detect spines and assume each spine has an excitatory synapse (Iascone, Li et al. 2018). Inhibitory synapses are detected by Teal-Gephyrin tagging. However, these methods are error-prone, depending on the size of the synapses. For example, Chen et al. (Chen, Villa et al. 2012) reported missing 20% of spines. In addition, 3D-EM allows for accurate measurement of certain (confounding) features of spines and synapses, such as synapse size, double-innervated spines and spine apparatus (Figure 14). To conclude, these methods can replace 3D-EM if the error-rate tolerance of the scientific question is higher.

### **9.1.2. Non-specific volume transmission and inhibition of L5 apical dendrites**

The neurogliaform (NGF) inhibitory interneurons were described to inhibit almost all pyramidal neurons within their axonal arborization (Tamás, Lőrincz et al. 2003, Oláh, Füle et al. 2009). This is done through non-specific volume transmission, which has slower kinetics compared to synaptic inhibition. In contrast to specific synaptic inhibition activating GABA<sub>A</sub> receptors, NGF cells activate extra-synaptic GABA<sub>B</sub> receptors by increasing the GABA concentration in the extracellular space. The activation of GABA<sub>B</sub> receptors on the surface of thick-tufted L5 apical dendrites was shown to directly inhibit voltage-gated calcium channels involved in Ca<sup>2+</sup> spike generation (Pérez-Garci, Gassmann et al. 2006, Pérez-Garci, Larkum et al. 2013, Abs, Poorthuis et al. 2018). Together, with our finding of baseline inhibition levels around the main bifurcation of L5tt neurons, this points towards the importance of volume transmission in the inhibition of calcium spikes in L5tt ADs at their main bifurcation.

### **9.1.3. Distance to soma as a determining factor of inhibitory strength at the main bifurcation of pyramidal neurons**

Surprisingly, we found significant differences in the inhibitory fraction at the main bifurcation of neurons from the upper (L2) and lower (L3) segments of the supra-granular cortex (Figure 5, 9). These neurons are generally grouped together under L2/3 pyramidal type both functionally (Petersen and Crochet 2013) and anatomically (Larkman and Mason 1990) even though certain properties were reported to depend on the somatic depth. For example, Svoboda et al. (Svoboda, Denk et al. 1997, Svoboda, Helmchen et al. 1999) reported that the location of the peak of calcium response along the AD depends on the somatic depth in L2/3 neurons.

We found an exponential relationship between the inhibitory fraction at the main bifurcation and the distance between soma and this structure. This relationship was present even within the L2 neuron population. In contrast, L5st neurons were the only cell-type that did not follow this relationship. Therefore, pyramidal cells in L2/3 have different synaptic composition at their main bifurcation, depending on the length of their apical dendrite trunk before the main bifurcation (Figure 11a-b). Interestingly, the exponential relationship is not as strongly present in either inhibitory or excitatory synapse densities (Figure 11c). This implies a cellular control mechanism specific for the relative inhibitory size that allows for variability in either synapse density.

We also mapped the inhibitory synaptic strength's relationship to cortical depth relative to pial surface (Figure 12). The inhibitory hot-zone for the main bifurcation of L2 pyramidal neurons was also observed in layer 2 (Figure 13a-b). However, cortical depth is not the ideal predictor of inhibitory strength since apical oblique dendrites at the same cortical depth tend to have a higher level of excitatory input. Therefore, such depth analysis discards the difference between inhibitory strength of oblique dendrites and the main trunk of apical dendrites.

Our mapping of synaptic inputs to apical dendrites in 6 EM-datasets allowed us to measure the relative inhibitory size along the apical dendrite of L2 pyramidal neurons before and after the main bifurcation (Figure 11d-e). We found a relationship where fraction of inhibitory synapses decreased exponentially with increasing distance to soma. The relationship is similar to the decrease in inhibitory fraction at the main



bifurcation of L2-5 ADs with distance to soma (Compare Figure 11a-b and d-e), which suggests a possible similar origin.

#### **9.1.4. Definition of L5 pyramidal neuron subtypes**

We defined the pyramidal cell types based upon the layer origin of their cell bodies. In layer 5, we found a cell variant with slender AD morphology, small cell body, AD diameter, and superficial main bifurcation as previously reported (Figure 8, (Larkman and Mason 1990, Groh, Meyer et al. 2009)). These cells were reported to have different physiological and structural properties as compared to their thick-tufted counterparts (Feldmeyer, Roth et al. 2005, Economo, Viswanathan et al. 2018). We also found L5st spine density to be significantly lower than their L5tt. Interestingly, the cell body depth was not different between the two cell types as hypothesized previously (L5A vs. L5B). This means that cells with different synaptic properties can coexist within the same cortical layer.

We also found a linear relationship between excitatory synapse density and the “thick-tuftedness” of pyramidal neurons. The thick-tuftedness was the first principal component of four morphological features used for classification of L5 subtypes. Our goal was to investigate whether the synaptic and morphological L5 subtypes differ in a gradual or sudden manner. Surprisingly, we see a graded change from slender-tufted to thick-tufted L5 types suggesting a possible continuum of L5 neuronal types.

#### **9.1.5. Composition of synapses onto shaft and spine of apical dendrites**

Excitatory synapses (asymmetric) are distinguished in EM micrographs from inhibitory synapses (symmetric) as based upon existence of features, such as, prominent postsynaptic density and round presynaptic vesicle shape (Gray 1957, Colonnier 1968). However, the resolution of the 3D-EM datasets did not allow for unambiguous distinction of these two synapse types (see examples in Figure 15a). In Gray’s original account and subsequent reports, excitatory (Braitenberg and Schüz 1998) and inhibitory synapses (Kubota, Karube et al. 2016) were described to target spines and shafts of dendrites, respectively. Additional reports also confirm this structural tendency for two synapse types to varying degrees, depending on the dendrite type investigated (White and Rock 1980, White and Hersch 1982, Chen, Villa

et al. 2012). Initially, we used this structural definition to distinguish excitatory and inhibitory synapse types.

However, reports suggested the possibility of excitatory input onto the shaft of pyramidal neurons (Parnavelas, Sullivan et al. 1977, Kwon, Merchán-Pérez et al. 2018). We, therefore, measured the tendency of axons to prefer spine and shaft of ADs, and found it to be almost binary with the exception of L5st neurons (Figure 15). These cells had significant spine-preferring input onto the shaft of their dendrites. Our results, combined with previous reports, suggest that location of synapse (spine vs. shaft) could be used to identify synapses (excitatory vs. inhibitory) in most cortical pyramidal neurons with few errors (<4%). Finally, double-innervated spines were reportedly innervated by one excitatory and one inhibitory input (Kubota, Hatada et al. 2007). We annotated all spines with double innervation to add them to both inhibitory and excitatory synapse groups (Figure 14c).

#### **9.1.6. Synapse density normalized to the surface area of apical dendrites**

The input impedance of a dendrite is inversely correlated with its diameter and surface area (Rall and Rinzel 1973, Rinzel and Rall 1974). This means that activation of the same number of synapses along the unit length of two dendrites creates a larger voltage change across the dendrite with smaller diameter (assuming other factors, such as, driving force remain constant). Therefore, synapse densities have been normalized to the unit surface area of dendrites to account for the larger surface area and lower input impedance of thicker dendrites (Bloss, Cembrowski et al. 2016). Additionally, apical dendrites are known to taper towards their distal tuft branches with the thick main bifurcation generating  $\text{Ca}^{2+}$  spikes in response to NMDA spikes in thin distal tuft branches (Katz, Menon et al. 2009, Larkum, Nevian et al. 2009).

We observed a ~2-fold reduction in average apical diameter between the main bifurcation and tuft branches of pyramidal cells, similar to previous light microscopic reports (Figure 16d,e, compare panels, (Larkum, Nevian et al. 2009)). This means that activation of a similar number of synapses could be more effective in distal tuft branches. Interestingly, L2 ADs (largest) were about ~2-fold larger in diameter as compared to L5st AD (smallest, Figure 16b, e). L3 and L5tt neurons had distributions between the L2 and L5st.

Next, we normalized the synapse densities to the surface area of ADs. Our main findings regarding cell-type specific synapse density difference were robust against surface area normalization (compare Figure 16 with Figure 5, 9, 10). Finally, the fraction of inhibitory synapses, which represents the relative possible inhibitory strength, is unaffected by diameter change.

#### **9.1.7. Specific innervation of L2 and L3/5 ADs**

Inhibitory neurons are known for targeting specific subcellular structures, such as, axon initial segments (Somogyi 1977), apical dendrites and cell bodies (for a review see (Kubota, Karube et al. 2016)). We, therefore, reconstructed AD-targeting inhibitory axonal segments in our 3D-EM data, and found two subpopulations preferring either L2 or L3/5 pyramidal neurons. The preference for both subpopulations was about 3-fold (Figure 17). This adds to previous physiological work, suggesting separate circuits controlling distinct populations of pyramidal neurons (Jiang, Wang et al. 2013).

As a control, we measured the pre- and postsynaptic target densities along the depth of the cortex to understand whether geometric separation could explain any of the observed innervation preferences (Figure 18). We found no such spatial separation of the ADs or the inhibitory axons innervating them.

In addition, we annotated other postsynaptic targets of pyramidal neurons into a total of 8 postsynaptic types (Figure 17e). Other than AD targeting preference, the L2 and L3/5(deep)-seeded populations were only different in their somatic innervation probability. This is, at least partly, caused by cortical region differences (see below).

#### **9.1.8. Multi-innervation of apical dendrites by inhibitory axons**

Inhibitory axons were previously shown to innervate apical dendrites by multiple synaptic contacts to control their electrical activity (~9 contacts per AD, (Silberberg and Markram 2007, Gidon and Segev 2012)). Our analysis of multi-innervation by inhibitory AD-targeting axons demonstrated that mono-innervation dominates within volumes of about  $10^6 \mu\text{m}^3$ . Only ~20% of ADs were targeted by multiple synapses of the same axonal segment (Figure 19). Reconstruction of complete inhibitory axons in a larger volume could determine whether the majority of the innervation is with a single synapse or multi-innervation happens across larger volumes.

We found that AD-type specific innervation was robust against removal of multiple targets on the same AD (Figure 19). Therefore, inhibitory axons preferentially innervate either L2 or deep ADs mostly through mono-synaptic innervation without generation of multiple contacts. However, we saw a slight drop in fractional innervation by inhibitory axons seeded from L2 (Figure 19c). Interestingly, the random selection process for the seed synapse was biased towards multi-innervating axons (compare Figure 19d and e). This generated a slight inflation in our fractional innervation of the L2 type, which was decreased by removal of all seed synapses.

#### **9.1.9. Quantitative consistency of axonal innervation across cortical regions**

To understand the variation of inhibitory innervation across the cortex, we applied our analysis to axons of S1, V2, PPC and ACC. Innervation probability was quantitatively consistent for 8 postsynaptic targets of AD-targeting axons across the cortical regions investigated (Figure 20). To our knowledge, this is the first report of such innervation consistency across multiple cortical regions, including primary sensory and high-order cortices.

The only variability between cortical regions was in innervation probability of L2 cell bodies by L3/5 AD-preferring axons (Figure 20c). In addition to variability between cortical regions, confounders, such as dataset location, could generate such L2 cell body innervation preferences (see Figure 4a for dataset location comparison of datasets).

In conclusion, we found specific inhibitory innervation of apical dendrites of pyramidal neurons in the upper layers of the mouse cortex. This suggests separate inhibitory neuronal circuitry involved in controlling apical dendrite activity. In addition, the cell-type specific pattern of inhibitory and excitatory input implies variable computational capabilities for apical dendrites of L2, L3 and L5 pyramidal neurons.

## **9.2. EM connectomic analysis of long-range input to posterior parietal cortex (PPC)**

### **9.2.1. Importance of image quality control routines in long-term high throughput volumetric 3D-EM**

Block-face volumetric imaging techniques, such as SBEM, are gaining popularity due to their mostly automatic process for 3D imaging. Currently, they are commercially available from the two most popular EM vendors: Zeiss (FIB-SEM) and FEI (ThermoFisher Scientific, VolumeScope). SBEM is well-suited for imaging sub-cubic millimeter samples. However, errors resulting in section loss are fatal in an SBEM experiment. One important source of error is defocus and astigmatism of electron beam due to factors, such as, daily temperature oscillations in the environment. Commercial focus and astigmatism correction software available in traditional SEMs depend on sequential imaging of a sacrificial area that creates a significant overhead for long-running experiments.

We, therefore, implemented a previously reported heuristic approach (Binding, Mikula et al. 2013) to aberration correction with an additional image processing step to avoid large objects, such as, blood vessels and nuclei (Figure 21). The autocorrelation-based approach to aberration estimation generates spurious results when applied to such large objects that lack detail (high frequency elements). This aberration correction routine was used to image 10 datasets across two microscopes by five experimenters (Figure 22, Table 6). The parameters for calibration of the aberration estimates needed to be corrected for each individual microscope. However, they were stable for imaging samples from different brain regions. Conversely, the heuristic parameters for the morphological operations to detect large objects were sensitive to variations of image texture from different experiments. Therefore, they need to be optimized for each dataset. The need for such parameter optimization would be removed with the use of convolutional neural networks for detection of large objects (LeCun, Boser et al. 1989, Dorkenwald, Schubert et al. 2017). These methods are robust against variability present in their training data.

### **9.2.2. Cell-type specific innervation of neurons in PPC by long-range input from M2 and V1**

PPC is an associative cortical region involved in visual decision making processes (Harvey, Coen et al. 2012). PPC neurons encode for both sensory and motor variables by receiving long-range cortical input (Goard, Pho et al. 2016). The importance of long-range innervation has been studied extensively in the primary somatosensory cortex of mice (Aronoff, Matyas et al. 2010). Long-range motor input was reported to encode whisker movement and touch variables (Petreanu, Gutnisky et al. 2012). Such motor information could be sampled by the apical dendrite of pyramidal neurons in S1 and interact with the  $\text{Ca}^{2+}$  spike initiation site to alter their output. In addition, inactivation of long-range motor input to S1 was shown to hamper non-declarative (perceptual) memory retention processes during sleep (Miyamoto, Hirai et al. 2016).

However, the cell-type specific innervation of cortical neurons by long-range innervation has not been extensively studied at the synaptic level. Imaging and analysis of even sub-cubic millimeter 3D-EM volumes was technically challenging until recently (Motta, Berning et al. 2019). To image long-range innervation using only 3D-EM requires volume sizes that are large fractions of the whole mouse brain. Even though efforts exist to image the full mouse brain (Mikula 2016), such volumetric imaging is beyond current technology available to most labs.

Thus, we applied a correlative light and electron microscopy approach to map long-range input to PPC from secondary motor (M2) and primary visual (V1) cortices (FluoEM, (Drawitsch, Karimi et al. 2018)). This technique uses the full color spectrum of the fluorescence light microscope. The advantage of FluoEM is the matching process of fluorescently labelled axons to their EM counterparts using the unique morphological fingerprint of each axon. Therefore, there's no need for laborious and error-prone electron-dense label conversion or infra-red fiducial marking. The matching process becomes progressively faster as more control points refine the transformation between two datasets.

Our preliminary analysis of layer-specific innervation of neurons in PPC by long-range innervation showed motor (M2) input's tendency to target only superficial

neurons in L2/3 (Figure 24, 25). L3 neurons comprised only 5% of the postsynaptic targets of long-range input from M2. In comparison, L3 neurons accounted for ~23% of the total postsynaptic targets of axons from V1 (~4-fold higher as compared to M2). This adds to our previous evidence suggesting significant differences in the innervation of L2 vs. L3 pyramidal neurons at their main bifurcation (Figure 9). However, multiple confounding factors, such as the spatial distribution of long-range axonal paths, errors in reconstruction, and the effect of dataset shape, require further investigation to confirm this finding.

## 10. Tables

	<b>S1</b>	<b>V2*</b>	<b>PPC*</b>	<b>ACC</b>	<b>LPtA</b>	<b>PPC-2</b>
<b>Mouse age (postnatal days)</b>	28	56	56	56	46	57
<b>Sample location (in mm) relative to bregma (AP,ML)</b>	(-1.2, -3.9)	(-2.6,1.7)	(-2,-1.7)	(0.8,-0.15)	(-2.1, -1.3)	(-2, -1.5)
<b>Sample section thickness (μm)</b>	1000	600	600	600	1000	600
<b>SEM type (FEI, USA)</b>	Magellan	Quanta	Quanta	Quanta	Verios	Magellan
<b>Electron landing energy (keV)</b>	2.8	2.8	2.8	2.8	2.8	2.8
<b>Beam current (nA)</b>	3.2	0.2	0.2	0.11-0.2	0.8	1.6
<b>Beam dwell time (μs)</b>	0.1	2.1 - 2.8	2.3	2.1 - 2.8	0.5	0.2
<b>Tile configuration in plane (x, y)</b>	3 x 3	1 x 2	1 x 2	1 x 3	4 x 5	5x5, 5x10
<b>Overlap between tiles (x, y)</b>	(21%, 11%)	(N/A, 8%)	(N/A, 6%)	(N/A, 4.5%)	(8%, 12%)	(6%, 7%)
<b>Single tile resolution (pixels)</b>	3072x2048	6144x4096	6144x4096	6144x4096	3072x2048	4096x3536
<b>voxel size (nm<sup>3</sup>)</b>	11.24x11.24x28	12x12x30	12x12x30	12x12x30	11.24x11.24x30	11.24x11.24x30
<b>Final high-resolution volume (μm<sup>3</sup>)</b>	66x89x202	72x91x153	72x93x141	70x141x98	130x110x85	200x185x200 200x370x100
<b>Dataset distance from pia (μm)</b>	125	215	170	110	20	10
<b>Low-resolution EM **</b>					X	X



Staining approach	Manual	AMW assistance	AMW assistance	AMW assistance	AMW assistance	Manual
Staining protocol	Conventional	Modified Hua	Modified Hua	Modified Hua	Modified Hua	Modified Hua

**Table 1. Experimental details**

This table summarizes the experimental parameters used for sample preparation and volumetric electron microscopy in 6 datasets from 5 cortical regions. \*From opposing hemispheres of same animal, \*\*Used for finding the apical dendrite's cell body of origin and apical dendrite reconstruction. This table is reproduced with modifications from (Karimi, Odenthal et al. 2019) and is licensed under the CC-BY-NC-ND 4.0.

	<b>V2</b>	<b>PPC</b>	<b>ACC</b>	<b>PPC-2</b>
<b>50% Ethanol</b>	30 min @ 4°C	30 min @ 4°C	30 min @ 4°C	30 min @ RT (cooled)
<b>75% Ethanol</b>	45 min @ 4°C	45 min @ 4°C	45 min @ 4°C	30 min @ RT (cooled)
<b>100% Ethanol</b>	45 min @ RT	45 min @ RT	45 min @ RT	2 times, 30 min @ RT
<b>Pure acetone</b>	3 times , 45 min each @ RT	3 times , 45 min each @ RT	3 times , 45 min each @ RT	4 times, 20 min each @ RT
<b>50% Spurr's resin in acetone</b>	3 hr @ RT (no rotation, closed tube). Next, open tube for 90 min initial rotation + overnight @ RT	3 hr @ RT (no rotation, closed tube). Next, open tube for 90 min initial rotation + overnight @ RT	3 hr @ RT (no rotation, closed tube). Next, open tube for 90 min initial rotation + overnight @ RT	4 hr @ RT, closed tube cap, slow rotation
<b>75% Spurr's resin</b>	N/A	N/A	N/A	Overnight @ RT. Slow rotation, closed caps.
<b>100% Spurr's resin</b>	6 hr @ RT	6 hr @ RT	6 hr @ RT	2 times, 3 hr @ RT each. No rotation

**Table 2. Temperature and times of dehydration and embedding steps for 3D-EM samples**

Time and duration of each dehydration and embedding step for samples from 3 cortical regions (n = 4). This table is reproduced with modifications from (Karimi, Odenthal et al. 2019) and is licensed under the CC-BY-NC-ND 4.0.

	<b>S1</b>	<b>V2*</b>	<b>PPC*</b>	<b>ACC</b>	<b>LPtA</b>	<b>PPC-2</b>
<b>Main bifurcation input mapping</b>	X	X	X	X		X
<b>Dense apical dendrite reconstruction</b>				X		
<b>Synapse size estimation</b>	X	X	X	X		
<b>Spine innervation fraction</b>		X	X	X	X	
<b>Double spine fraction</b>	X	X	X	X		
<b>Fractional innervation of inhibitory axons</b>	X	X	X	X		
<b>Cell type comparisons of inhibitory fraction</b>	X (only L2)	X(only L2)	X(only L2)	X(only L2)	X	X
<b>Path distance to soma dependency</b>	X (only L2)	X(only L2)	X(only L2)	X(only L2)	X	X
<b>Profile of inhibitory fraction along upper cortex</b>	X	X	X	X	X	X

**Table 3. Data analysis**

Summary of analyses carried out in all 6 datasets. This table is reproduced with modifications from (Karimi, Odenthal et al. 2019) and is licensed under the CC-BY-NC-ND 4.0.

Dataset layer origin	L1		L2	
Seed structure	Shaft	Spine	Shaft	Spine
Layer 2	14,29 (n = 14)	100 (n = 5)	0 (n = 92)	97,1 (n = 35)
Layer 3	3,7 (n = 27)	100 (n = 16)	N/A	N/A
Layer 5tt	22,5 (n = 40)	93,3 (n = 30)	N/A	N/A
Deep (Layer 3/5)	N/A	N/A	1,1 (n = 91)	98,4 (n = 61)
Layer 5st	60 (n=10)	N/A	44,44 (n = 9)	N/A

**Table 4. Fraction of spine-preferring (excitatory) input on spine and shaft of apical dendrites**

The percentage of spine-preferring (excitatory) synapses onto the shaft and spine of apical dendrites for L2-5 pyramidal cell types in layers 1 and 2. Number of axons used to calculate the fraction is given inside the parenthesis.

	Somatic depth relative to pia ( $\mu\text{m}$ )	
Dataset name	PPC-2	LPtA
Layer 2	208-250	268-295
Layer 2MN	166-172	N/A
Layer 3	304-376	327-442
Layer 5tt	524-582	621-657
Layer 5st	507-620	N/A

**Table 5. The somatic depth of pyramidal neurons relative to pial surface**

Somatic depth of pyramidal neurons residing in layers 2-5 ( $n = 40$ , 11 for PPC-2 and LPtA, respectively). See also Figure 7.

Microscope type (FEI)	Experimenter	Species	Age	Sex	Brain region (layer)	Dimensions ( $\mu\text{m}^3$ )
Verios	Jakob Straehle	Human	41 years	Female	Medial temporal gyrus	110x130x100 (Figure 22c)
			63 years	Male	Superior temporal gyrus	140x120 x100
		Non-human primate (Macaque)	7 years	N/A	Primary somatosensory cortex (L4)	180x170x150 (Figure 22b)
			7 years	N/A	Primary somatosensory cortex (L2/3)	224x176x100
	Vijayan Gangadharan	Mouse (C57BL/6)	168 days	Male	Anterior cingulate cortex (L1-3)	225x175x120
			168 days		Primary somatosensory cortex (L3-4)	225x175x200
			112 days		Medial entorhinal cortex (L2/3)	225x175x120
Magellan	Kun Song	(C57BL/6)	27 days	Male	Primary somatosensory cortex (L4-5)	280x240x280 (Figure 22a)
	Marcel Beining		28 days		Dentate gyrus	322x207x200
	Ali Karimi		57 days		PPC (L1-5)	200x185x200 200x370x100

**Table 6. Datasets acquired using automated aberration adjustment**

Properties of 10 datasets acquired using the automated aberration adjustment software from 3 species by 5 experimenters.

## 11. References

- Abbe, E. (1883). "XV.—The Relation of Aperture and Power in the Microscope (continued)\*." Journal of the Royal Microscopical Society **3**(6): 790-812.
- Abs, E., R. B. Poorthuis, D. Apelblat, K. Muhammad, M. B. Pardi, L. Enke, D. Kushinsky, D.-L. Pu, M. F. Eizinger, K.-k. Conzelmann, I. Spiegel and J. J. Letzkus (2018). "Learning-Related Plasticity in Dendrite-Targeting Layer 1 Interneurons." Neuron **100**(3): 684-699.e686.
- Ahissar, E., R. Sosnik, K. Bagdasarian and S. Haidarliu (2001). "Temporal Frequency of Whisker Movement. II. Laminar Organization of Cortical Representations." Journal of Neurophysiology **86**(1): 354-367.
- Andres, B., U. Köthe, M. Helmstaedter, W. Denk and F. A. Hamprecht (2008). Segmentation of SBFSEM Volume Data of Neural Tissue by Hierarchical Classification. Pattern Recognition, Berlin, Heidelberg, Springer Berlin Heidelberg.
- Aronoff, R., F. Matyas, C. Mateo, C. Ciron, B. Schneider and C. C. H. Petersen (2010). "Long-range connectivity of mouse primary somatosensory barrel cortex." European Journal of Neuroscience **31**(12): 2221-2233.
- Bang, B. G. and F. B. Bang (1957). "Graphic reconstruction of the third dimension from serial electron microphotographs." Journal of Ultrastructure Research **1**(2): 138-146.
- Bannister, N. J. and A. U. Larkman (1995). "Dendritic morphology of CA1 pyramidal neurones from the rat hippocampus: II. Spine distributions." Journal of Comparative Neurology **360**(1): 161-171.
- Barth, A. L. and J. F. A. Poulet (2012). "Experimental evidence for sparse firing in the neocortex." Trends in Neurosciences **35**(6): 345-355.
- Berger, H. (1929). "Über das elektroencephalogramm des menschen." European Archives of Psychiatry and Clinical Neuroscience **87**(1): 527-570.
- Berning, M., K. M. Boergens and M. Helmstaedter (2015). "SegEM: Efficient Image Analysis for High-Resolution Connectomics." Neuron **87**(6): 1193-1206.
- Betzig, E., G. H. Patterson, R. Sougrat, O. W. Lindwasser, S. Olenych, J. S. Bonifacino, M. W. Davidson, J. Lippincott-Schwartz and H. F. Hess (2006). "Imaging Intracellular Fluorescent Proteins at Nanometer Resolution." Science **313**(5793): 1642-1645.
- Binding, J., S. Mikula and W. Denk (2013). "Low-Dosage Maximum-A-Posteriori Focusing and Stigmatism." Microscopy and Microanalysis **19**(01): 38-55.
- Birch-Andersen, A. (1955). "Reconstruction of the nuclear sites of Salmonella typhimurium from electron micrographs of serial sections." Microbiology **13**(2): 327-329.
- Bishop, D., I. Nikić, M. Brinkoetter, S. Knecht, S. Potz, M. Kerschensteiner and T. Misgeld (2011). "Near-infrared branding efficiently correlates light and electron microscopy." Nature Methods **8**(7): 568-570.
- Bisley, J. W. and M. E. Goldberg (2010). "Attention, intention, and priority in the parietal lobe." Annual review of neuroscience **33**: 1-21.

Bloss, E. B., M. S. Cembrowski, B. Karsh, J. Colonell, R. D. Fetter and N. Spruston (2016). "Structured Dendritic Inhibition Supports Branch-Selective Integration in CA1 Pyramidal Cells." Neuron **89**(5): 1016-1030.

Bloss, E. B., M. S. Cembrowski, B. Karsh, J. Colonell, R. D. Fetter and N. Spruston (2018). "Single excitatory axons form clustered synapses onto CA1 pyramidal cell dendrites." Nature Neuroscience **21**(3): 353-363.

Bock, D. D., W.-C. A. Lee, A. M. Kerlin, M. L. Andermann, G. Hood, A. W. Wetzel, S. Yurgenson, E. R. Soucy, H. S. Kim and R. C. Reid (2011). "Network anatomy and in vivo physiology of visual cortical neurons." Nature **471**(7337): 177-182.

Boergens, K. M., M. Berning, T. Bocklisch, D. Bräunlein, F. Drawitsch, J. Frohnhofen, T. Herold, P. Otto, N. Rzepka, T. Werkmeister, D. Werner, G. Wiese, H. Wissler and M. Helmstaedter (2017). "WebKnossos: Efficient online 3D data annotation for connectomics." Nature Methods **14**(7): 691-694.

Bohland, J. W., C. Wu, H. Barbas, H. Bokil, M. Bota, H. C. Breiter, H. T. Cline, J. C. Doyle, P. J. Freed, R. J. Greenspan, S. N. Haber, M. Hawrylycz, D. G. Herrera, C. C. Hilgetag, Z. J. Huang, A. Jones, E. G. Jones, H. J. Karten, D. Kleinfeld, R. Kötter, H. A. Lester, J. M. Lin, B. D. Mensh, S. Mikula, J. Panksepp, J. L. Price, J. Safdieh, C. B. Saper, N. D. Schiff, J. D. Schmahmann, B. W. Stillman, K. Svoboda, L. W. Swanson, A. W. Toga, D. C. Van Essen, J. D. Watson and P. P. Mitra (2009). "A Proposal for a Coordinated Effort for the Determination of Brainwide Neuroanatomical Connectivity in Model Organisms at a Mesoscopic Scale." PLoS Comput Biol **5**(3): e1000334-e1000334.

Boyden, E. S., F. Zhang, E. Bamberg, G. Nagel and K. Deisseroth (2005). "Millisecond-timescale, genetically targeted optical control of neural activity." Nature Neuroscience **8**(9): 1263-1268.

Braitenberg, V. and A. Schüz (1998). Cortex: statistics and geometry of neuronal connectivity, Springer Science & Business Media.

Braitenberg, V. B. and A. Schuz (1991). Anatomy of the Cortex: Statistics and Geometry.

Brecht, M., M. Schneider, B. Sakmann and T. W. Margrie (2004). "Whisker movements evoked by stimulation of single pyramidal cells in rat motor cortex." Nature **427**(6976): 704-710.

Briggman, K. L. and D. D. Bock (2012). "Volume electron microscopy for neuronal circuit reconstruction." Current opinion in neurobiology **22**(1): 154-161.

Briggman, K. L. and W. Denk (2006). "Towards neural circuit reconstruction with volume electron microscopy techniques." Current Opinion in Neurobiology **16**(5): 562-570.

Briggman, K. L., M. Helmstaedter and W. Denk (2011). "Wiring specificity in the direction-selectivity circuit of the retina." Nature **471**(7337): 183-188.

Buchs, P. A. and D. Muller (1996). "Induction of long-term potentiation is associated with major ultrastructural changes of activated synapses." Proceedings of the National Academy of Sciences of the United States of America **93**(15): 8040-8045.

Buniatyan, D., S. Popovych, D. Ih, T. Macrina, J. Zung and H. S. Seung (2020). Weakly Supervised Deep Metric Learning for Template Matching. Advances in Computer Vision, Cham, Springer International Publishing.



Bush, P. C. and T. J. Sejnowski (1994). "Effects of inhibition and dendritic saturation in simulated neocortical pyramidal cells." Journal of Neurophysiology **71**(6): 2183-2193.

Cajal, S. R., J. DeFelipe and E. G. Jones (1988). Cajal on the Cerebral Cortex: An Annotated Translation of the Complete Writings, Oxford University Press.

Cajal, S. R. y. (1899). Textura del sistema nervioso del hombre y de los vertebrados: estudios sobre el plan estructural y composición histológica de los centros nerviosos adicionados de consideraciones fisiológicas fundadas en los nuevos descubrimientos, N. Moya.

Canny, J. (1986). "A Computational Approach to Edge Detection." IEEE Transactions on Pattern Analysis and Machine Intelligence **PAMI-8**(6): 679-698.

Cauler, L. J., B. Clancy and B. W. Connors (1998). "Backward cortical projections to primary somatosensory cortex in rats extend long horizontal axons in layer I." Journal of Comparative Neurology **390**(2): 297-310.

Cheetham, C. E. J., S. J. Barnes, G. Albieri, G. W. Knott and G. T. Finnerty (2014). "Pansynaptic enlargement at adult cortical connections strengthened by experience." Cerebral cortex (New York, N.Y. : 1991) **24**(2): 521-531.

Chen, F., P. W. Tillberg and E. S. Boyden (2015). "Expansion microscopy." Science **347**(6221): 543-548.

Chen, J. L., K. L. Villa, J. W. Cha, P. T. C. So, Y. Kubota and E. Nedivi (2012). "Clustered Dynamics of Inhibitory Synapses and Dendritic Spines in the Adult Neocortex." Neuron **74**(2): 361-373.

Chen, J. L., F. F. Voigt, M. Javadzadeh, R. Krueppel and F. Helmchen (2016). "Long-range population dynamics of anatomically defined neocortical networks." Elife **5**: e14679.

Chen, T. W., T. J. Wardill, Y. Sun, S. R. Pulver, S. L. Renninger, A. Baohan, E. R. Schreiter, R. A. Kerr, M. B. Orger, V. Jayaraman, L. L. Looger, K. Svoboda and D. S. Kim (2013). "Ultrasensitive fluorescent proteins for imaging neuronal activity." Nature **499**(7458): 295-300.

Cheney, P. D. (1985). "Role of Cerebral Cortex in Voluntary Movements: A Review." Physical Therapy **65**(5): 624-635.

Colonnier, M. (1968). "Synaptic patterns on different cell types in the different laminae of the cat visual cortex. An electron microscope study." Brain Research **9**(2): 268-287.

Constantinople, C. M. and R. M. Bruno (2013). "Deep Cortical Layers Are Activated Directly by Thalamus." Science **340**(6140): 1591.

Conti, F., A. Rustioni, P. Petrusz and A. C. Towle (1987). "Glutamate-positive neurons in the somatic sensory cortex of rats and monkeys." The Journal of neuroscience : the official journal of the Society for Neuroscience **7**(6): 1887-1901.

Coogan, T. A. and A. Burkhalter (1990). "Conserved patterns of cortico-cortical connections define areal hierarchy in rat visual cortex." Experimental Brain Research **80**(1): 49-53.

Crick, F. and C. Koch Towards a neurobiological theory of consciousness, Saunders Scientific Publications.

de Broglie, L. (1925). "Recherches sur la théorie des Quanta." Ann. Phys. **10**(3): 22-128.

de Kock, C. P. J. and B. Sakmann (2009). "Spiking in primary somatosensory cortex during natural whisking in awake head-restrained rats is cell-type specific." Proceedings of the National Academy of Sciences **106**(38): 16446-16450.

Denk, W. (2006). "Two-photon scanning photochemical microscopy: mapping ligand-gated ion channel distributions." Proceedings of the National Academy of Sciences **91**(14): 6629-6633.

Denk, W., K. L. Briggman and M. Helmstaedter (2012). "Structural neurobiology: missing link to a mechanistic understanding of neural computation." Nature reviews. Neuroscience **13**(5): 351-358.

Denk, W. and H. Horstmann (2004). "Serial block-face scanning electron microscopy to reconstruct three-dimensional tissue nanostructure." PLoS Biology **2**(11).

Denk, W., J. H. Strickler and W. W. Webb (1990). "Two-photon laser scanning fluorescence microscopy." Science **248**(4951): 73-76.

Dombeck, D. a., A. N. Khabbaz, F. Collman, T. L. Adelman and D. W. Tank (2007). "Imaging Large-Scale Neural Activity with Cellular Resolution in Awake, Mobile Mice." Neuron **56**: 43-57.

Dorkenwald, S., P. J. Schubert, M. F. Killinger, G. Urban, S. Mikula, F. Svara and J. Kornfeld (2017). "Automated synaptic connectivity inference for volume electron microscopy." Nature Methods **14**(4): 435-442.

Douglas, R. J. and K. A. C. Martin (2004). "NEURONAL CIRCUITS OF THE NEOCORTEX." Annual Review of Neuroscience **27**(1): 419-451.

Drawitsch, F., A. Karimi, K. M. Boergens and M. Helmstaedter (2018). "FluoEM, virtual labeling of axons in three-dimensional electron microscopy data for long-range connectomics." eLife **7**: e38976-e38976.

Ebbesen, C. L., G. Doron, C. Lenschow and M. Brecht (2017). "Vibrissa motor cortex activity suppresses contralateral whisking behavior." Nature Neuroscience **20**(1): 82-89.

Eberle, a. L., S. Mikula, R. Schalek, J. W. Lichtman, M. L. K. Tate and D. Zeidler (2015). "High-resolution, high-throughput imaging with a multibeam scanning electron microscope." Journal of Microscopy **00**(0): n/a-n/a.

Economo, M. N., S. Viswanathan, B. Tasic, E. Bas, J. Winnubst, V. Menon, L. T. Graybuck, T. N. Nguyen, K. A. Smith, Z. Yao, L. Wang, C. R. Gerfen, J. Chandrashekar, H. Zeng, L. L. Looger and K. Svoboda (2018). "Distinct descending motor cortex pathways and their roles in movement." Nature **563**(7729): 79-84.

Feldmeyer, D., V. Egger, J. Lübke and B. Sakmann (1999). "Reliable synaptic connections between pairs of excitatory layer 4 neurones within a single 'barrel' of developing rat somatosensory cortex." The Journal of Physiology **521**(1): 169-190.

Feldmeyer, D., G. Qi, V. Emmenegger and J. F. Staiger (2018). "Inhibitory Interneurons and their Circuit Motifs in the Many Layers of the Barrel Cortex." Neuroscience **368**: 132-151.

Feldmeyer, D., A. Roth and B. Sakmann (2005). "Monosynaptic Connections between Pairs of Spiny Stellate Cells in Layer 4 and Pyramidal Cells in Layer 5A Indicate That Lemniscal and Paralemniscal Afferent Pathways Converge in the Infragranular Somatosensory Cortex." The Journal of Neuroscience **25**(13): 3423.

Fiala, J. C. (2005). "Reconstruct: a free editor for serial section microscopy." Journal of Microscopy **218**(1): 52-61.

Frank, L. and I. Müllerová (1999). "Strategies for low-and ver-low-energy SEM." Microscopy **48**(3): 205-219.

Franklin, K. and G. Paxinos (2008). The mouse brain in stereotaxic coordinates.

Fried, S. I., T. A. Münch and F. S. Werblin (2002). "Mechanisms and circuitry underlying directional selectivity in the retina." Nature **420**(6914): 411-414.

Genoud, C., B. Titze, A. Graff-Meyer and R. W. Friedrich (2018). "Fast Homogeneous En Bloc Staining of Large Tissue Samples for Volume Electron Microscopy." Frontiers in Neuroanatomy **12**: 76.

Gidon, A. and I. Segev (2012). "Principles Governing the Operation of Synaptic Inhibition in Dendrites." Neuron **75**(2): 330-341.

Glickfeld, L. L., M. H. Histed and J. H. R. Maunsell (2013). "Mouse Primary Visual Cortex Is Used to Detect Both Orientation and Contrast Changes." The Journal of Neuroscience **33**(50): 19416.

Goard, M. J., G. N. Pho, J. Woodson and M. Sur (2016). "Distinct roles of visual, parietal, and frontal motor cortices in memory-guided sensorimotor decisions." eLife **5**(AUGUST): 1-30.

Gold, J. I. and M. N. Shadlen (2007). "The neural basis of decision making." Annu. Rev. Neurosci. **30**: 535-574.

Goldstein, J. I., D. E. Newbury, J. R. Michael, N. W. M. Ritchie, J. H. J. Scott and D. C. Joy (2017). Scanning electron microscopy and X-ray microanalysis, Springer.

Graham, B. J., D. G. C. Hildebrand, A. T. Kuan, J. T. Maniates-Selvin, L. A. Thomas, B. L. Shanny and W.-C. A. Lee (2019). "High-throughput transmission electron microscopy with automated serial sectioning." bioRxiv: 657346.

Gray, B. E. G. (1957). "Axo-Somatic and Axo-Dendritic Synapses of the Cerebral Cortex : an Electron Microscope Study."

Gray, E. G. (1957). "Axo-Somatic and Axo-Dendritic Synapses of the Cerebral Cortex: an Electron Microscope Study."

Gray, E. G. and R. W. Guillery (1963). "A NOTE ON THE DENDRITIC SPINE APPARATUS." Journal of anatomy **97**(Pt 3): 389-392.

Gray, E. G. and L. H. Hamlyn (1962). "Electron microscopy of experimental degeneration in the avian optic tectum." Journal of anatomy **96**(Pt 3): 309-316.305.

Groh, A., H. S. Meyer, E. F. Schmidt, N. Heintz, B. Sakmann and P. Krieger (2009). "Cell-Type Specific Properties of Pyramidal Neurons in Neocortex Underlying a Layout that Is Modifiable Depending on the Cortical Area." Cerebral Cortex **20**(4): 826-836.

Guo, Zengcai V., N. Li, D. Huber, E. Ophir, D. Gutnisky, Jonathan T. Ting, G. Feng and K. Svoboda (2014). "Flow of Cortical Activity Underlying a Tactile Decision in Mice." Neuron **81**(1): 179-194.

Hamill, O. P., A. Marty, E. Neher, B. Sakmann and F. J. Sigworth (1981). "Improved patch-clamp techniques for high-resolution current recording from cells and cell-free membrane patches." Pflügers Archiv **391**(2): 85-100.

Harris, K. M. and J. K. Stevens (1988). "Dendritic spines of rat cerebellar Purkinje cells: serial electron microscopy with reference to their biophysical characteristics." Journal of Neuroscience **8**(12): 4455-4469.

Harris, K. M. and J. K. Stevens (1989). "Dendritic spines of CA 1 pyramidal cells in the rat hippocampus: serial electron microscopy with reference to their biophysical characteristics." The Journal of Neuroscience **9**(8): 2982 LP-2997.

Harvey, C. D., P. Coen and D. W. Tank (2012). "Choice-specific sequences in parietal cortex during a virtual-navigation decision task." Nature **484**(7392): 62-68.

Harvey, C. D. and K. Svoboda (2007). "Locally dynamic synaptic learning rules in pyramidal neuron dendrites." Nature **450**(7173): 1195-1200.

Hayat, M. A. (1981). Principles and techniques of electron microscopy. Biological applications, Edward Arnold.

Hayworth, K., N. Kasthuri, R. Schalek and J. Lichtman (2006). "Automating the Collection of Ultrathin Serial Sections for Large Volume TEM Reconstructions." Microscopy and Microanalysis **12**(S02): 86-87.

Hayworth, K. J., D. Peale, M. Januszewski, G. W. Knott, Z. Lu, C. S. Xu and H. F. Hess (2019). "Gas cluster ion beam SEM for imaging of large tissue samples with 10 nm isotropic resolution." Nature Methods.

Hayworth, K. J., C. S. Xu, Z. Lu, G. W. Knott, R. D. Fetter, J. C. Tapia, J. W. Lichtman and H. F. Hess (2015). "Ultrastructurally smooth thick partitioning and volume stitching for large-scale connectomics." Nature Methods **12**: 319.

Hell, S. W. and J. Wichmann (1994). "Breaking the diffraction resolution limit by stimulated emission: stimulated-emission-depletion fluorescence microscopy." Optics Letters **19**(11): 780-782.

Helmchen, F. and W. Denk (2005). "Deep tissue two-photon microscopy." Nature Methods **2**(12): 932-940.

Helmchen, F., W. Denk and J. N. D. Kerr (2013). "Miniaturization of two-photon microscopy for imaging in freely moving animals." Cold Spring Harbor Protocols **2013**: 904-913.

Helmchen, F., K. Svoboda, W. Denk and D. W. Tank (1999). "In vivo dendritic calcium dynamics in deep-layer cortical pyramidal neurons." Nature Neuroscience **2**: 989-996.

Helmstaedter, M. (2013). "Cellular-resolution connectomics: challenges of dense neural circuit reconstruction." Nature methods **10**(6): 501-507.

Helmstaedter, M. (2015). "The Mutual Inspirations of Machine Learning and Neuroscience." Neuron **86**(1): 25-28.

Helmstaedter, M., K. L. Briggman and W. Denk (2011). "High-accuracy neurite reconstruction for high-throughput neuroanatomy." Nature Neuroscience **14**(8): 1081-1088.

Helmstaedter, M., K. L. Briggman and W. Denk (2011). "High-accuracy neurite reconstruction for high-throughput neuroanatomy." Nature Neuroscience **14**: 1081.

Hennig, P. and W. Denk (2007). "Point-spread functions for backscattered imaging in the scanning electron microscope." Journal of Applied Physics **102**(12): 123101.

Herculano-Houzel, S. (2009). "The human brain in numbers: a linearly scaled-up primate brain." Frontiers in Human Neuroscience **3**.

Hess, S. T., T. P. K. Girirajan and M. D. Mason (2006). "Ultra-High Resolution Imaging by Fluorescence Photoactivation Localization Microscopy." Biophysical Journal **91**(11): 4258-4272.

Heymann, J. A. W., M. Hayles, I. Gestmann, L. A. Giannuzzi, B. Lich and S. Subramaniam (2006). "Site-specific 3D imaging of cells and tissues with a dual beam microscope." Journal of structural biology **155**(1): 63-73.

Hodgkin, A. L. and A. F. Huxley (1952). "A quantitative description of membrane current and its application to conduction and excitation in nerve." The Journal of Physiology **117**(4): 500-544.

Holler-Rickauer, S., G. Koestinger, K. A. C. Martin, G. F. P. Schuhknecht and K. J. Stratford (2019). "Structure and function of a neocortical synapse." bioRxiv: 2019.2012.2013.875971.

Holt, Christine E. and Erin M. Schuman (2013). "The Central Dogma Decentralized: New Perspectives on RNA Function and Local Translation in Neurons." Neuron **80**(3): 648-657.

Hua, Y., P. Laserstein and M. Helmstaedter (2015). "Large-volume en-bloc staining for electron microscopy-based connectomics." Nature communications **6**: 7923-7923.

Huang, B., M. Bates and X. Zhuang (2009). "Super-Resolution Fluorescence Microscopy." Annual Review of Biochemistry **78**(1): 993-1016.

Hubel, D. H. and T. N. Wiesel (1959). "Receptive fields of single neurones in the cat's striate cortex." The Journal of Physiology **148**: 574-591.

Hübener, M. and J. Bolz (1988). "Morphology of identified projection neurons in layer 5 of rat visual cortex." Neuroscience Letters **94**(1): 76-81.

Hübener, M., C. Schwarz and J. Bolz (1990). "Morphological types of projection neurons in layer 5 of cat visual cortex." Journal of Comparative Neurology **301**(4): 655-674.

Iascone, D. M., Y. Li, U. Sumbul, M. Doron, H. Chen, V. Andreu, F. Goudy, I. Segev, H. Peng and F. Polleux (2018). "Whole-neuron synaptic mapping reveals local balance between excitatory and inhibitory synapse organization." bioRxiv: 395384-395384.

Ito, M., M. Kato and M. Kawabata (1998). "Premature bifurcation of the apical dendritic trunk of vibrissa-responding pyramidal neurones of X-irradiated rat neocortex." Journal of Physiology **512**(2): 543-553.

J. Lee, T., A. Kumar, A. H. Balwani, D. Brittain, S. Kinn, C. A. Tovey, E. Dyer, N. M. da Costa, R. C. Reid, C. Forest and D. J. Bumbarger (2018). Large-scale neuroanatomy using LASSO: Loop-based Automated Serial Sectioning Operation.

Jain, V., J. F. Murray, F. Roth, S. Turaga, V. Zhigulin, K. L. Briggman, M. N. Helmstaedter, W. Denk and H. S. Seung (2007). Supervised Learning of Image Restoration with Convolutional Networks. 2007 IEEE 11th International Conference on Computer Vision.

Januszewski, M., J. Kornfeld, P. H. Li, A. Pope, T. Blakely, L. Lindsey, J. Maitin-Shepard, M. Tyka, W. Denk and V. Jain (2018). "High-precision automated reconstruction of neurons with flood-filling networks." Nature Methods **15**(8): 605-610.

Jiang, X., G. Wang, A. J. Lee, R. L. Stornetta and J. J. Zhu (2013). "The organization of two new cortical interneuronal circuits." Nature neuroscience **16**(2): 210-218.

Karimi, A., J. Odenthal, F. Drawitsch, K. M. Boergens and M. Helmstaedter (2019). "Cell-type specific innervation of cortical pyramidal cells at their apical tufts." bioRxiv: 571695-571695.

Kasthuri, N., K. J. Hayworth, D. R. Berger, R. L. Schalek, J. A. Conchello, S. Knowles-Barley, D. Lee, A. Vázquez-Reina, V. Kaynig, T. R. Jones, M. Roberts, J. L. Morgan, J. C. Tapia, H. S. Seung, W. G. Roncal, J. T. Vogelstein, R. Burns, D. L. Sussman, C. E. Priebe, H. Pfister and J. W. Lichtman (2015). "Saturated Reconstruction of a Volume of Neocortex." Cell **162**(3): 648-661.

Kasthuri, N., Kenneth J. Hayworth, Daniel R. Berger, Richard L. Schalek, José A. Conchello, S. Knowles-Barley, D. Lee, A. Vázquez-Reina, V. Kaynig, Thouis R. Jones, M. Roberts, Josh L. Morgan, Juan C. Tapia, H. S. Seung, William G. Roncal, Joshua T. Vogelstein, R. Burns, Daniel L. Sussman, Carey E. Priebe, H. Pfister and Jeff W. Lichtman (2015). "Saturated Reconstruction of a Volume of Neocortex." Cell **162**(3): 648-661.

Kato, Hiroyuki K., Shea N. Gillet and Jeffry S. Isaacson (2015). "Flexible Sensory Representations in Auditory Cortex Driven by Behavioral Relevance." Neuron **88**(5): 1027-1039.

Katz, Y., V. Menon, D. A. Nicholson, Y. Geinisman, W. L. Kath and N. Spruston (2009). "Synapse Distribution Suggests a Two-Stage Model of Dendritic Integration in CA1 Pyramidal Neurons." Neuron **63**(2): 171-177.

Klar, T. A. and S. W. Hell (1999). "Subdiffraction resolution in far-field fluorescence microscopy." Optics Letters **24**(14): 954-956.

Kleinfeld, D., A. Bharioke, P. Blinder, D. D. Bock, K. L. Briggman, D. B. Chklovskii, W. Denk, M. Helmstaedter, J. P. Kaufhold, W.-C. A. Lee, H. S. Meyer, K. D. Micheva, M. Oberlaender, S. Prohaska, R. C. Reid, S. J. Smith, S. Takemura, P. S. Tsai and B. Sakmann (2011). "Large-Scale Automated Histology in the Pursuit of Connectomes." The Journal of Neuroscience **31**(45): 16125-16138.

Knoll, M. and E. Ruska (1932). "Das elektronenmikroskop." Zeitschrift für physik **78**(5-6): 318-339.

Knott, G., H. Marchman, D. Wall and B. Lich (2008). "Serial Section Scanning Electron Microscopy of Adult Brain Tissue Using Focused Ion Beam Milling." The Journal of Neuroscience **28**(12): 2959.

Koch, C., T. Poggio and V. Torre (1983). "Nonlinear interactions in a dendritic tree: localization, timing, and role in information processing." Proceedings of the National Academy of Sciences **80**(9): 2799.

Kolb, B. and J. Walkey (1987). "Behavioural and anatomical studies of the posterior parietal cortex in the rat." Behavioural brain research **23**: 127-145.

Kornfeld, J. and W. Denk (2018). "Progress and remaining challenges in high-throughput volume electron microscopy." Current Opinion in Neurobiology **50**: 261-267.

Krieg, W. J. S. (1946). "Connections of the cerebral cortex. I. The albino rat. B. Structure of the cortical areas." The Journal of Comparative Neurology **84**(3): 277-323.

Krizhevsky, A., I. Sutskever and G. E. Hinton Imagenet classification with deep convolutional neural networks.

Krizhevsky, A., I. Sutskever and G. E. Hinton (2012). Imagenet classification with deep convolutional neural networks. Advances in neural information processing systems.

Kubota, Y., S. Hatada, S. Kondo, F. Karube and Y. Kawaguchi (2007). "Neocortical Inhibitory Terminals Innervate Dendritic Spines Targeted by Thalamocortical Afferents." Journal of Neuroscience **27**(5): 1139-1150.

Kubota, Y., F. Karube, M. Nomura and Y. Kawaguchi (2016). "The Diversity of Cortical Inhibitory Synapses." **10**(April): 1-15.

Kubota, Y., J. Sohn and Y. Kawaguchi (2018). "Large Volume Electron Microscopy and Neural Microcircuit Analysis." Frontiers in Neural Circuits **12**: 98.

Kwon, T., A. Merchán-Pérez, E. M. Rial Verde, J.-R. Rodríguez, J. DeFelipe and R. Yuste (2018). "Ultrastructural, Molecular and Functional Mapping of GABAergic Synapses on Dendritic Spines and Shafts of Neocortical Pyramidal Neurons." Cerebral Cortex.

Larkman, A. and A. Mason (1990). "Correlations between morphology and electrophysiology of pyramidal neurons in slices of rat visual cortex. I. Establishment of cell classes." The Journal of neuroscience : the official journal of the Society for Neuroscience **10**(5): 1407-1414.

Larkman, A. U. (1991). "Dendritic Morphology of Pyramidal Neurones of the Visual Cortex of the Rat: 111. Spine Distributions." the Journal of Comparative Neurology **306**: 332-343.

Larkum, M. (2013). "A cellular mechanism for cortical associations: An organizing principle for the cerebral cortex." Trends in Neurosciences **36**(3): 141-151.

Larkum, M. E., T. Nevian, M. Sandler, A. Polsky and J. Schiller (2009). "Synaptic Integration in Tuft Dendrites of Layer 5 Pyramidal Neurons: A New Unifying Principle." Science **325**(5941): 756-760.

Larkum, M. E., L. S. Petro, R. N. S. Sachdev and L. Muckli (2018). "A Perspective on Cortical Layering and Layer-Spanning Neuronal Elements." Frontiers in Neuroanatomy **12**(56).

Larkum, M. E., W. Senn and H.-R. Lüscher (2004). "Top-down Dendritic Input Increases the Gain of Layer 5 Pyramidal Neurons." Cerebral Cortex **14**(10): 1059-1070.

Larkum, M. E. and J. J. Zhu (2002). "Signaling of layer 1 and whisker-evoked Ca<sup>2+</sup> and Na<sup>+</sup> action potentials in distal and terminal dendrites of rat neocortical pyramidal neurons in vitro and in vivo." The Journal of neuroscience : the official journal of the Society for Neuroscience **22**(16): 6991-7005.

Larkum, M. E., J. J. Zhu and B. Sakmann (1999). "A new cellular mechanism for coupling inputs arriving at different cortical layers." Nature **398**(6725): 338-341.

Larkum, M. E., J. J. Zhu and B. Sakmann (2001). "Dendritic mechanisms underlying the coupling of the dendritic with the axonal action potential initiation zone of adult rat layer 5 pyramidal neurons." Journal of Physiology **533**(2): 447-466.

Lecun, Y., Y. Bengio and G. Hinton (2015). "Deep learning." Nature **521**(7553): 436-444.

LeCun, Y., B. Boser, J. S. Denker, D. Henderson, R. E. Howard, W. Hubbard and L. D. Jackel (1989). "Backpropagation Applied to Handwritten Zip Code Recognition." Neural Computation **1**(4): 541-551.

Ledergerber, D. and M. E. Larkum (2010). "Properties of Layer 6 Pyramidal Neuron Apical Dendrites." Journal of Neuroscience **30**(39): 13031-13044.

Ledergerber, D. and M. E. Larkum (2012). "The time window for generation of dendritic spikes by coincidence of action potentials and EPSPs is layer specific in somatosensory cortex." PLoS ONE **7**(3): 3-7.

Leighton, S. B. (1981). "SEM images of block faces, cut by a miniature microtome within the SEM-a technical note." Scanning electron microscopy(Pt 2): 73-76.

Liu, G. (2004). "Local structural balance and functional interaction of excitatory and inhibitory synapses in hippocampal dendrites." Nature Neuroscience **7**(4): 373-379.

Logothetis, N. K. (2008). "What we can do and what we cannot do with fMRI." Nature **453**(7197): 869-878.

Luo, H., K. Hasegawa, M. Liu and W.-J. Song (2017). "Comparison of the Upper Marginal Neurons of Cortical Layer 2 with Layer 2/3 Pyramidal Neurons in Mouse Temporal Cortex." Frontiers in Neuroanatomy **11**: 115.

Lynch, J. C. (1980). "The functional organization of posterior parietal association cortex." Behavioral and Brain Sciences **3**(04): 485-499.

Manns, I. D., B. Sakmann and M. Brecht (2004). "Sub- and suprathreshold receptive field properties of pyramidal neurones in layers 5A and 5B of rat somatosensory barrel cortex." The Journal of Physiology **556**(2): 601-622.

Mao, T., D. Kusefoglu, Bryan M. Hooks, D. Huber, L. Petreanu and K. Svoboda (2011). "Long-Range Neuronal Circuits Underlying the Interaction between Sensory and Motor Cortex." Neuron **72**(1): 111-123.

Markram, H., J. Lübke, M. Frotscher and B. Sakmann (1997). "Regulation of Synaptic Efficacy by Coincidence of Postsynaptic APs and EPSPs." Science **275**(5297): 213-215.



Markram, H., M. Toledo-Rodriguez, Y. Wang, A. Gupta, G. Silberberg and C. Wu (2004). "Interneurons of the neocortical inhibitory system." Nature Reviews Neuroscience **5**(10): 793-807.

Megías, M., Z. Emri, T. F. Freund and A. I. Gulyás (2001). "Total number and distribution of inhibitory and excitatory synapses on hippocampal CA1 pyramidal cells." Neuroscience **102**(3): 527-540.

Meyer, H. S., D. Schwarz, V. C. Wimmer, A. C. Schmitt, J. N. D. Kerr, B. Sakmann and M. Helmstaedter (2011). "Inhibitory interneurons in a cortical column form hot zones of inhibition in layers 2 and 5A." Proceedings of the National Academy of Sciences **108**(40): 16807.

Micheva, K. D. and S. J. Smith (2007). "Array Tomography: A New Tool for Imaging the Molecular Architecture and Ultrastructure of Neural Circuits." Neuron **55**(1): 25-36.

Migliore, M. and G. M. Shepherd (2002). "EMERGING RULES FOR THE DISTRIBUTIONS OF ACTIVE DENDRITIC CONDUCTANCES." **3**(May): 362-370.

Mikula, S. (2016). "Progress Towards Mammalian Whole-Brain Cellular Connectomics." Frontiers in neuroanatomy **10**: 62-62.

Mikula, S. (2017). In-Chamber Reel-to-Reel System for Random-Access Volume Electron Microscopy.

Mikula, S., J. Binding and W. Denk (2012). "Staining and embedding the whole mouse brain for electron microscopy." Nature Methods **9**: 1198.

Mikula, S. and W. Denk (2015). "High-resolution whole-brain staining for electron microscopic circuit reconstruction." Nature Methods **12**: 541.

Minka, T. P. (2000). "Estimating a Dirichlet distribution."

Mitchell, E., S. Keselj, S. Popovych, D. Buniatyan and H. S. Seung (2019). "Siamese encoding and alignment by multiscale learning with self-supervision." arXiv preprint arXiv:1904.02643.

Miyamoto, D., D. Hirai, C. C. A. Fung, A. Inutsuka, M. Odagawa, T. Suzuki, R. Boehringer, C. Adaikkan, C. Matsubara, N. Matsuki, T. Fukai, T. J. McHugh, A. Yamanaka and M. Murayama (2016). "Top-down cortical input during NREM sleep consolidates perceptual memory." Science **352**(6291): 1315.

Motta, A., M. Berning, K. M. Boergens, B. Staffler, M. Beining, S. Loomba, P. Hennig, H. Wissler and M. Helmstaedter (2019). "Dense connectomic reconstruction in layer 4 of the somatosensory cortex." Science: eaay3134.

Mountcastle, V. B. (1957). "MODALITY AND TOPOGRAPHIC PROPERTIES OF SINGLE NEURONS OF CAT'S SOMATIC SENSORY CORTEX." Journal of Neurophysiology **20**(4): 408-434.

Nakai, J., M. Ohkura and K. Imoto (2001). "A high signal-to-noise Ca(2+) probe composed of a single green fluorescent protein." Nature Biotechnology **19**(2): 137-141.

Narayanan, R. T., R. Egger, A. S. Johnson, H. D. Mansvelder, B. Sakmann, C. P. J. de Kock and M. Oberlaender (2015). "Beyond Columnar Organization: Cell Type- and Target

Layer-Specific Principles of Horizontal Axon Projection Patterns in Rat Vibrissal Cortex." Cerebral Cortex **25**(11): 4450-4468.

Neher, E. and B. Sakmann (1976). "Single-channel currents recorded from membrane of denervated frog muscle fibres." Nature **260**(5554): 799-802.

Ni, J. and J. L. Chen (2017). "Long-range cortical dynamics: a perspective from the mouse sensorimotor whisker system." European Journal of Neuroscience **46**(8): 2315-2324.

Nitz, D. A. (2006). "Tracking route progression in the posterior parietal cortex." Neuron **49**: 747-756.

Ogawa, S., T.-M. Lee, A. R. Kay and D. W. Tank (1990). "Brain magnetic resonance imaging with contrast dependent on blood oxygenation." Proceedings of the National Academy of Sciences **87**(24): 9868-9872.

Oh, S. W., J. a. Harris, L. Ng, B. Winslow, N. Cain, S. Mihalas, Q. Wang, C. Lau, L. Kuan, A. M. Henry, M. T. Mortrud, B. Ouellette, T. N. Nguyen, S. a. Sorensen, C. R. Slaughterbeck, W. Wakeman, Y. Li, D. Feng, A. Ho, E. Nicholas, K. E. Hirokawa, P. Bohn, K. M. Joines, H. Peng, M. J. Hawrylycz, J. W. Phillips, J. G. Hohmann, P. Wohnoutka, C. R. Gerfen, C. Koch, A. Bernard, C. Dang, A. R. Jones and H. Zeng (2014). "A mesoscale connectome of the mouse brain." Nature **508**(7495): 207-214.

Oláh, S., M. Füle, G. Komlósi, C. Varga, R. Báldi, P. Barzó and G. Tamás (2009). "Regulation of cortical microcircuits by unitary GABA-mediated volume transmission." Nature **461**(7268): 1278-1281.

Paden, R. S. and W. C. Nixon (1968). "Retarding field scanning electron microscopy." Journal of Physics E: Scientific Instruments **1**(11): 1073-1080.

Palade, G. E. (1952). "A STUDY OF FIXATION FOR ELECTRON MICROSCOPY." The Journal of Experimental Medicine **95**(3): 285.

Pallotto, M., P. V. Watkins, B. Fubara, J. H. Singer and K. L. Briggman (2015). "Extracellular space preservation aids the connectomic analysis of neural circuits." eLife **4**: e08206.

Palmer, L. M., J. M. Schulz, S. C. Murphy, D. Ledergerber, M. Murayama and M. E. Larkum (2012). "The Cellular Basis of GABAB-Mediated Interhemispheric Inhibition." Science **335**(February): 989-993.

Palomero-Gallagher, N. and K. Zilles (2015). Isocortex, Strukturelle und funktionelle Organisation des Gehirns.

Parnavelas, J. G., K. Sullivan, A. R. Lieberman and K. E. Webster (1977). "Neurons and their synaptic organization in the visual cortex of the rat." Cell and Tissue Research **183**(4): 499-517.

Pennycook, S. J. and P. D. Nellist (2011). Scanning transmission electron microscopy: imaging and analysis, Springer Science & Business Media.

Pérez-Garci, E., M. Gassmann, B. Bettler and M. E. Larkum (2006). "The GABAB1b Isoform Mediates Long-Lasting Inhibition of Dendritic Ca<sup>2+</sup> Spikes in Layer 5 Somatosensory Pyramidal Neurons." Neuron **50**(4): 603-616.

Pérez-García, E., M. E. Larkum and T. Nevian (2013). "Inhibition of dendritic Ca<sup>2+</sup> spikes by GABAB receptors in cortical pyramidal neurons is mediated by a direct Gi/o-β-subunit interaction with Cav1 channels." The Journal of physiology **591**(Pt 7): 1599-1612.

Petersen, C. C. H. and S. Crochet (2013). "Synaptic computation and sensory processing in neocortical layer 2/3." Neuron **78**(1): 28-48.

Petreaanu, L., D. A. Gutnisky, D. Huber, N.-I. Xu, D. H. O'Connor, L. Tian, L. Looger and K. Svoboda (2012). "Activity in motor-sensory projections reveals distributed coding in somatosensation." Nature **489**(7415): 299-303.

Petreaanu, L., D. Huber, A. Sobczyk and K. Svoboda (2007). "Channelrhodopsin-2-assisted circuit mapping of long-range callosal projections." Nature Neuroscience **10**(5): 663-668.

Petreaanu, L., T. Mao, S. M. Sternson and K. Svoboda (2009). "The subcellular organization of neocortical excitatory connections." Nature **457**(7233): 1142-1145.

Phifer, D., L. Tuma, T. Vystavel, P. Wandrol and R. J. Young (2009). "Improving SEM Imaging Performance Using Beam Deceleration." Microscopy Today **17**(4): 40-49.

Polsky, A., B. W. Mel and J. Schiller (2004). "Computational subunits in thin dendrites of pyramidal cells." Nature Neuroscience **7**(6): 621-627.

Preibisch, S., S. Saalfeld and P. Tomancak (2009). "Globally optimal stitching of tiled 3D microscopic image acquisitions." Bioinformatics **25**(11): 1463-1465.

Rall, W. (1959). "Branching dendritic trees and motoneuron membrane resistivity." Experimental Neurology **1**(5): 491-527.

Rall, W. and J. Rinzel (1973). "Branch Input Resistance and Steady Attenuation for Input to One Branch of a Dendritic Neuron Model." Biophysical Journal **13**(7): 648-688.

Rash, J. E., T. Yasumura and F. E. Dudek (1998). "ULTRASTRUCTURE, HISTOLOGICAL DISTRIBUTION, AND FREEZE-FRACTURE IMMUNOCYTOCHEMISTRY OF GAP JUNCTIONS IN RAT BRAIN AND SPINAL CORD." Cell Biology International **22**(11-12): 731-749.

Reep, R. L., H. C. Chandler, V. King and J. V. Corwin (1994). "Rat posterior parietal cortex: topography of corticocortical and thalamic connections." Experimental Brain Research **100**(1): 67-84.

Rinzel, J. and W. Rall (1974). "Transient response in a dendritic neuron model for current injected at one branch." Biophysical journal **14**(10): 759-790.

Rojas-Piloni, G., J. M. Guest, R. Egger, A. S. Johnson, B. Sakmann and M. Oberlaender (2017). "Relationships between structure, in vivo function and long-range axonal target of cortical pyramidal tract neurons." Nature Communications **8**(1): 870.

Rosenblatt, F. (1958). "The perceptron: a probabilistic model for information storage and organization in the brain." Psychological review **65**(6): 386.

Rust, M. J., M. Bates and X. Zhuang (2006). "Sub-diffraction-limit imaging by stochastic optical reconstruction microscopy (STORM)." Nature Methods **3**(10): 793-796.

Samuel, A. L. (1959). "Some Studies in Machine Learning Using the Game of Checkers." IBM Journal of Research and Development **3**(3): 210-229.

Santuy, A., J. R. Rodriguez, J. DeFelipe and A. Merchan-Perez (2018). "Volume electron microscopy of the distribution of synapses in the neuropil of the juvenile rat somatosensory cortex." Brain Structure and Function **223**(1): 77-90.

Sato, T. (1968). "A Modified Method for Lead Staining of Thin Sections." Microscopy **17**(2): 158-159.

Schaefer, A. T. (2003). "Coincidence Detection in Pyramidal Neurons Is Tuned by Their Dendritic Branching Pattern." Journal of Neurophysiology **89**(6): 3143-3154.

Scheffer, L. K., B. Karsh and S. Vitaladevun (2013). "Automated Alignment of Imperfect EM Images for Neural Reconstruction." 1-23.

Schmidt, H., A. Gour, J. Straehle, K. M. Boergens, M. Brecht and M. Helmstaedter (2017). "Axonal synapse sorting in medial entorhinal cortex." Nature.

Segal, M., A. Vlachos and E. Korkotian (2010). "The Spine Apparatus, Synaptopodin, and Dendritic Spine Plasticity." The Neuroscientist **16**(2): 125-131.

Seligman, A. M., H. L. Wasserkrug and J. S. Hanker (1966). "A NEW STAINING METHOD (OTO) FOR ENHANCING CONTRAST OF LIPID-CONTAINING MEMBRANES AND DROPLETS IN OSMIUM TETROXIDE-FIXED TISSUE WITH OSMIOPHILIC THIOCARBOHYDRAZIDE (TCH)." The Journal of Cell Biology **30**(2): 424.

Silberberg, G. and H. Markram (2007). "Disynaptic Inhibition between Neocortical Pyramidal Cells Mediated by Martinotti Cells." Neuron **53**(5): 735-746.

Somogyi, P. (1977). "A specific 'axo-axonal' interneuron in the visual cortex of the rat." Brain Research **136**(2): 345-350.

Soto, G. E., S. J. Young, M. E. Martone, T. J. Deerinck, S. Lamont, B. O. Carragher, K. Hama and M. H. Ellisman (1994). "Serial Section Electron Tomography: A Method for Three-Dimensional Reconstruction of Large Structures." NeuroImage **1**(3): 230-243.

Špaček, J. (1985). "Three-dimensional analysis of dendritic spines." Anatomy and Embryology **171**(2): 235-243.

Spruston, N. (2008). "Pyramidal neurons: Dendritic structure and synaptic integration." Nature Reviews Neuroscience **9**(3): 206-221.

Spurr, A. R. (1969). "A low-viscosity epoxy resin embedding medium for electron microscopy." Journal of Ultrastructure Research **26**(1): 31-43.

Staffler, B., M. Berning, K. M. Boergens, A. Gour, P. van der Smagt and M. Helmstaedter (2017). "SynEM, automated synapse detection for connectomics." eLife **6**: 1-25.

Stepanyants, A., L. M. Martinez, A. S. Ferecskó and Z. F. Kisvárdy (2009). "The fractions of short- and long-range connections in the visual cortex." Proceedings of the National Academy of Sciences **106**(9): 3555.

Stuart, G. J., H. U. Dodt and B. Sakmann (1993). "Patch-clamp recordings from the soma and dendrites of neurons in brain slices using infrared video microscopy." Pflügers Archiv : European journal of physiology **423**: 511-518.

Stuart, G. J. and B. Sakmann (1994). "Active propagation of somatic action potentials into neocortical pyramidal cell dendrites." Nature **367**(6458): 69-72.

Südhof, Thomas C. (2013). "Neurotransmitter Release: The Last Millisecond in the Life of a Synaptic Vesicle." Neuron **80**(3): 675-690.

Svoboda, K., W. Denk, D. Kleinfeld and D. W. Tank (1997). In vivo dendritic calcium dynamics in neocortical pyramidal neurons. **385**: 161-165.

Svoboda, K., F. Helmchen, W. Denk and D. W. Tank (1999). "Spread of dendritic excitation in layer 2/3 pyramidal neurons in rat barrel cortex in vivo." Nature Neuroscience **2**: 65-73.

Svoboda, K., D. W. Tank and W. Denk (1996). "Direct Measurement of Coupling Between Dendritic Spines and Shafts." Science **272**(5262): 716-719.

Takahashi, N., T. G. Oertner, P. Hegemann and M. E. Larkum (2016). "Active cortical dendrites modulate perception." Science **354**(6319): 1587-1590.

Tamás, G., A. Lőrincz, A. Simon and J. Szabadics (2003). "Identified sources and targets of slow inhibition in the neocortex." Science **299**(5614): 1902-1905.

Tapia, J. C., N. Kasthuri, K. J. Hayworth, R. Schalek, J. W. Lichtman, S. J. Smith and J. Buchanan (2012). "High-contrast en bloc staining of neuronal tissue for field emission scanning electron microscopy." Nature protocols **7**(2): 193-206.

Tasic, B., Z. Yao, L. T. Graybiel, K. A. Smith, T. N. Nguyen, D. Bertagnolli, J. Goldy, E. Garren, M. N. Economo, S. Viswanathan, O. Penn, T. Bakken, V. Menon, J. Miller, O. Fong, K. E. Hirokawa, K. Lathia, C. Rimorin, M. Tieu, R. Larsen, T. Casper, E. Barkan, M. Kroll, S. Parry, N. V. Shapovalova, D. Hirschstein, J. Pendergraft, H. A. Sullivan, T. K. Kim, A. Szafer, N. Dee, P. Groblewski, I. Wickersham, A. Cetin, J. A. Harris, B. P. Levi, S. M. Sunkin, L. Madisen, T. L. Daigle, L. Looger, A. Bernard, J. Phillips, E. Lein, M. Hawrylycz, K. Svoboda, A. R. Jones, C. Koch and H. Zeng (2018). "Shared and distinct transcriptomic cell types across neocortical areas." Nature **563**(7729): 72-78.

Titze, B. and W. Denk (2013). "Automated in-chamber specimen coating for serial block-face electron microscopy." Journal of microscopy **250**(2): 101-110.

Titze, B. and C. Genoud (2016). "Volume scanning electron microscopy for imaging biological ultrastructure." Biology of the Cell **108**(11): 307-323.

Titze, B., C. Genoud and R. W. Friedrich (2018). "SBEMImage: versatile acquisition control software for serial block-face electron microscopy." Frontiers in neural circuits **12**: 54.

Treisman, A. (1996). "The binding problem." Current Opinion in Neurobiology **6**(2): 171-178.

Venable, J. H. and R. Coggeshall (1965). "A SIMPLIFIED LEAD CITRATE STAIN FOR USE IN ELECTRON MICROSCOPY." The Journal of cell biology **25**(2): 407-408.

von Ardenne, M. (1938). "Das elektronen-rastermikroskop. Praktische ausführung." Zeitschrift für technische Physik **19**(11): 407-416.

W. A. Spencer, E. R. K. (1959). "ELECTROPHYSIOLOGY OF HIPPOCAMPAL NEURONS: IV. FAST PREPOTENTIALS." Potentials(32).

Walton, J. (1979). "Lead asparate, an en bloc contrast stain particularly useful for ultrastructural enzymology." Journal of Histochemistry & Cytochemistry **27**(10): 1337-1342.

Waters, J., M. Larkum, B. Sakmann and F. Helmchen (2003). "Supralinear Ca<sup>2+</sup> influx into dendritic tufts of layer 2/3 neocortical pyramidal neurons in vitro and in vivo." The Journal of neuroscience : the official journal of the Society for Neuroscience **23**(24): 8558-8567.

Watson, M. L. (1958). "Staining of tissue sections for electron microscopy with heavy metals." The Journal of Cell Biology **4**(4): 475-478.

Weisenburger, S., F. Tejera, J. Demas, B. Chen, J. Manley, F. T. Sparks, F. Martínez Traub, T. Daigle, H. Zeng, A. Losonczy and A. Vaziri (2019). "Volumetric Ca<sup>2+</sup> Imaging in the Mouse Brain Using Hybrid Multiplexed Sculpted Light Microscopy." Cell: 1-17.

White, E. L. and S. M. Hersch (1982). "A quantitative study of thalamocortical and other synapses involving the apical dendrites of corticothalamic projection cells in mouse Sml cortex." Journal of Neurocytology **11**(1): 137-157.

White, E. L. and M. P. Rock (1980). "Three-dimensional aspects and synaptic relationships of a Golgi-impregnated spiny stellate cell reconstructed from serial thin sections." Journal of Neurocytology **9**(5): 615-636.

White, J. G., E. Southgate, J. N. Thomson and S. Brenner (1986). "The Structure of the Nervous System of the Nematode *Caenorhabditis elegans*." Philosophical Transactions of the Royal Society of London B: Biological Sciences **314**(1165): 1-340.

Whitlock, J. R., G. Pfuhl, N. Dagslott, M. B. Moser and E. I. Moser (2012). "Functional Split between Parietal and Entorhinal Cortices in the Rat." Neuron **73**(4): 789-802.

Whitlock, J. R., R. J. Sutherland, M. P. Witter, M.-B. Moser and E. I. Moser (2008). "Navigating from hippocampus to parietal cortex." Proceedings of the National Academy of Sciences of the United States of America **105**(39): 14755-14762.

Willingham, M. C. and A. V. Rutherford (1984). "The use of osmium-thiocarbohydrazide-osmium (OTO) and ferrocyanide-reduced osmium methods to enhance membrane contrast and preservation in cultured cells." Journal of Histochemistry & Cytochemistry **32**(4): 455-460.

Wimmer, V. C., R. M. Bruno, C. P. J. de Kock, T. Kuner and B. Sakmann (2010). "Dimensions of a Projection Column and Architecture of VPM and POM Axons in Rat Vibrissal Cortex." Cerebral Cortex **20**(10): 2265-2276.

Winnubst, J., E. Bas, T. A. Ferreira, Z. Wu, M. N. Economo, P. Edson, B. J. Arthur, C. Bruns, K. Rokicki, D. Schauder, D. J. Olbris, S. D. Murphy, D. G. Ackerman, C. Arshadi, P. Baldwin, R. Blake, A. Elsayed, M. Hasan, D. Ramirez, B. Dos Santos, M. Weldon, A. Zafar, J. T. Dudman, C. R. Gerfen, A. W. Hantman, W. Korff, S. M. Sternson, N. Spruston, K. Svoboda and J. Chandrashekar (2019). "Reconstruction of 1,000 Projection Neurons Reveals New Cell Types and Organization of Long-Range Connectivity in the Mouse Brain." Cell **179**(1): 268-281.e213.

Woolsey, T. A. and H. Van der Loos (1970). "The structural organization of layer IV in the somatosensory region (S I) of mouse cerebral cortex: The description of a cortical field composed of discrete cytoarchitectonic units." Brain Research **17**(2): 205-242.

Xu, C. S., K. J. Hayworth, Z. Lu, P. Grob, A. M. Hassan, J. G. García-Cerdán, K. K. Niyogi, E. Nogales, R. J. Weinberg and H. F. Hess (2017). "Enhanced FIB-SEM systems for large-volume 3D imaging." eLife **6**: e25916.

Yamawaki, N., X. Li, L. Lambot, L. Y. Ren, J. Radulovic and G. M. G. Shepherd (2019). "Long-range inhibitory intersection of a retrosplenial thalamocortical circuit by apical tuft-targeting CA1 neurons." Nature neuroscience **22**(4): 618-626.

Yuste, R. and W. Denk (1995). Dendritic spines as basic functional units of neuronal integration, Nature Publishing Group. **375**: 682-684.

Yuste, R., M. J. Gutnick, D. Saar, K. R. Delaney and D. W. Tank (1994). "Ca<sup>2+</sup> accumulations in dendrites of neocortical pyramidal neurons: An apical band and evidence for two functional compartments." Neuron **13**(1): 23-43.

Zhang, Q., W.-C. A. Lee, D. L. Paul and D. D. Ginty (2019). "Multiplexed peroxidase-based electron microscopy labeling enables simultaneous visualization of multiple cell types." Nature Neuroscience **22**(5): 828-839.

Zheng, Z., J. S. Lauritzen, E. Perlman, C. G. Robinson, M. Nichols, D. Milkie, O. Torrens, J. Price, C. B. Fisher, N. Sharifi, S. A. Calle-Schuler, L. Kmecova, I. J. Ali, B. Karsh, E. T. Trautman, J. A. Bogovic, P. Hanslovsky, G. S. X. E. Jefferis, M. Kazhdan, K. Khairy, S. Saalfeld, R. D. Fetter and D. D. Bock (2018). "A Complete Electron Microscopy Volume of the Brain of Adult *Drosophila melanogaster*." Cell **174**(3): 730-743.e722.

## 12. Curriculum vitae (CV)

Ali Karimi, M.Sc.

E-mail: [ali.karimi@brain.mpg.de](mailto:ali.karimi@brain.mpg.de)

Nationality: Iranian

### EDUCATION:

**Max Planck Institute for Brain Research**  
**Doctoral Student**

Frankfurt, Germany  
10/2015-present

**Machine learning summer school**

Two week lecture series on the recent advances in machine learning

Stellenbosch, South Africa  
1/2019

**Graduate Training Center of Neuroscience at Tübingen Universität**  
**Master of Science** in Cellular & Molecular Neuroscience: GPA: 1.3  
**Dean's List**

Tübingen, Germany  
9/2013-8/2015  
10/2013-7/2014

**Department of Biotechnology, University of Tehran**  
**Bachelor of Science** in Biotechnology: GPA: 18.34/20

Tehran, Iran  
9/2009-7/2013

**Pre-University Education in Bio-Experimental Sciences**  
**Hasheminejad Pre-University Institute:** GPA: 19.05/20

Mashhad, Iran  
9/2008-6/2009

Supervised by NODET (National Organization for the Development of Exceptional Talents)

**High School Education in Bio-Experimental Sciences**

**Hasheminejad High School** (under the supervision of NODET): GPA: 19.7/20

Mashhad, Iran  
9/2005-6/2008

### RESEARCH INVOLVEMENT:

**Max Planck Institute for Brain Research, PhD studies**

Frankfurt, Germany

**Department of Connectomics Supervised by Dr. Moritz Helmstaedter**

10/2015-present

Studied pre- and post-synaptic innervation patterns in the apical tuft dendrite of pyramidal neurons in 4 neocortical regions in mouse.

Used correlative light and electron microscopy to study long-range innervation input to posterior parietal cortex (PPC) at the synaptic level from visual and premotor cortices.

**Max Planck Institute for Brain Research, Master Thesis**

Frankfurt, Germany

**Department of Connectomics Supervised by Dr. Moritz Helmstaedter**

1/2015-8/2015

Studied the micro-connectivity underlying navigational decision making in the posterior parietal cortex.

**Max Planck Institute for Brain Research, Laboratory Rotation**

Frankfurt, Germany

**Department of Connectomics Supervised by Dr. Moritz Helmstaedter**

9/2014-12/2014

Prepared large volume electron microscopy samples for micro-connectivity analysis of the posterior parietal cortex

**Max Planck Institute for Developmental Biology, Laboratory Rotation**

Tübingen, Germany

**Evolutionary Biology Department, Supervised by Martin Wilecki**

2/2014-3/2014

Analyzed predatory behavior in *Pristionchus pacificus*.

**Institute of Molecular Biotechnology, Summer Internship**

Vienna, Austria

**Penninger Group, Supervised by Dr. Vanja Nagy**

7/2012-9/2012

Studied the role of RANK in learning and memory.

**University of Tehran, Department of Biotechnology, Research Assistant**

Tehran, Iran

**Genetics and Molecular Biology Laboratory of Prof. Elahe Elahi**

4/2011-8/2013

Analyzed the effects of eye microRNAs on expression level of glaucoma related genes.



Screened ADAMTS10 for mutations in primary open angle glaucoma (POAG) patients.

GRANTS & SCHOLARSHIPS:

<b>Hertie Foundation Scholarship for Excellent International Students</b>	10/2013-9/2014
<b>Vienna Biocenter (VBC) Summer Program Stipendium</b>	Summer 2012
<b>Iran Ministry of Science, Research and Technology Fellowship</b>	2009-2013

HONORS & MEMBERSHIPS:

<b>Member of the National Elite Foundation of Iran</b>	2009-Present
<b>National University Entrance Exam</b> , awarded 153 <sup>rd</sup> place among ~300,000 students	2009
<b>Acceptance to the Direct PhD program of Biotechnology</b> , University of Tehran	2009
<b>National Biology Olympiad</b> , awarded Silver medal	2008

TEACHING EXPERIENCE:

<b>Collaborative Science Symposium</b>	Nairobi, Kenya
Taught basics of microscopy and data analysis with MATLAB at University of Nairobi	01/2019
<b>Biology Olympiad Instructor</b>	Tehran, Iran
Taught at most prominent high schools in Tehran (AllameHelli, Salam, Mofid, etc.)	2010-2013
<b>High School Biology Olympiad Instructor</b>	Mashhad, Iran
Taught at Hasheminejad High School	2012
<b>Cell Biology Instructor</b>	Tehran, Iran
Taught in part for the National Olympiad Team Selection	2012

CONFERENCES:

<b>NeNa 2018</b> , invited speaker	Schramberg, Germany 9/2018
<b>FENS Forum of neuroscience</b> , poster presenter	Berlin, Germany 7/2018
<b>Connectomics Conference</b> , invited speaker, poster presenter, attendee	Berlin, Germany 4/2019, 4/2017, 9/2014
<b>Society for Neuroscience</b> , attendee	Chicago, U.S.A. 04/2015

PRESENTATIONS:

<b>The inhibitory input connectome of apical tuft dendrites in mouse cerebral cortex</b>	Frankfurt, Germany 5/2018
Max Planck-Hebrew University Meeting	
<b>Preparation of large volume electron microscopy samples for micro-connectivity analysis of navigational decision making in the parietal cortex</b>	Tübingen, Germany 4/2014
Laboratory rotation presentation for the Graduate Training Program	
<b>Analysis of predatory behavior in <i>Pristionchus pacificus</i></b>	Tübingen, Germany 11/2014
Laboratory rotation presentation for the Graduate Training Program	
<b>Studying the role of RANK in learning and memory</b>	Vienna, Austria 8/2012
Summer School Symposium	

LANGUAGES:

Native Persian, fluent English, basic German, and familiarity with Arabic.

## PROGRAMMING SKILLS:

MATLAB: Written a toolbox for analysis of skeleton reconstructions from volumetric electron microscopy (3D-EM) data. In addition, I wrote a package for automatic adjustment of focus during 3D-EM data acquisition. Finally, I have modified and used software packages for image processing.

Java: Modified a toolbox for controlling a custom-built 3D-EM system.

C++: Added image processing routines to a toolbox used for alignment of large 3D-EM volumes.

Git/Gitlab: Everyday use for version control.

Linux/Bash: Performing large scale image processing routines on a compute cluster.

## PUBLICATIONS:

---

**Karimi, A.\***, Odenthal, J.\*, Drawitsch, F., Boergens, K. M., & Helmstaedter, M. (2019). Cell-type specific innervation of cortical pyramidal cells at their apical tufts. BioRxiv (preprint, under Review), 571695. <http://doi.org/10.1101/571695>

\* equally contributing

Drawitsch, F., **Karimi, A.**, Boergens, K. M., & Helmstaedter, M. (2018). FluoEM, virtual labeling of axons in three-dimensional electron microscopy data for long-range connectomics. eLife, 7, e38976. <http://doi.org/10.7554/eLife.38976>